Chem Soc Rev

ROYAL SOCIETY OF CHEMISTRY

REVIEW ARTICLE

View Article Online
View Journal | View Issue

Check for updates

Cite this: *Chem. Soc. Rev.*, 2022, **51**, 188

Catalyst overcoating engineering towards high-performance electrocatalysis

Qiang Liu,[ab] Marco Ranocchiari[b] and Jeroen A. van Bokhoven*[ab]

Received 28th June 2021

DOI: 10.1039/d1cs00270h

rsc.li/chem-soc-rev

Clean and sustainable energy needs the development of advanced heterogeneous catalysts as they are of vital importance for electrochemical transformation reactions in renewable energy conversion and storage devices. Advances in nanoscience and material chemistry have afforded great opportunities for the design and optimization of nanostructured electrocatalysts with high efficiency and practical durability. In this review article, we specifically emphasize the synthetic methodologies for the versatile surface overcoating engineering reported to date for optimal electrocatalysts. We discuss the recent progress in the development of surface overcoating-derived electrocatalysts potentially applied in polymer electrolyte fuel cells and water electrolyzers by correlating catalyst intrinsic structures with electrocatalytic properties. Finally, we present the opportunities and perspectives of surface overcoating engineering for the design of advanced (electro)catalysts and their deep exploitation in a broad scope of applications.

1. Introduction

Heterogeneous catalysts, comprising metal nanoparticles (NPs) and solid supports, are widely applied in thermal- and electrocatalysis fields for clean and sustainable energy. Porous carbon, graphene and metal oxides with high specific surface area are the commonly exploited support materials for dispersing metal NPs.[1–3] Supported metal based catalysts with diverse particle size, composition, morphology and metal–support interactions can be generated to show distinct catalytic properties.[4–6] However, the encountered unstable performance and easy deactivation as a consequence of metal particle agglomeration, coalescence and Ostwald ripening are the remaining obstacles that impair their wide applications.[7,8] The issue concerning

---

[a] *Institute for Chemical and Bioengineering, ETH Zurich, Vladimir Prelog Weg 1, 8093 Zurich, Switzerland. E-mail: jeroen.vanbokhoven@chem.ethz.ch*
[b] *Laboratory for Catalysis and Sustainable Chemistry, Paul Scherrer Institut, 5232 Villigen PSI, Switzerland*

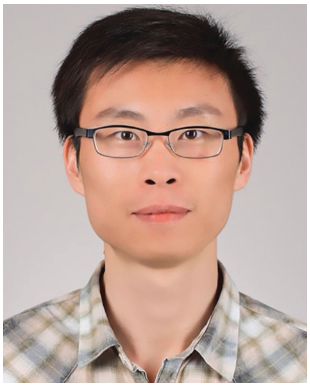

Qiang Liu

Qiang Liu received a BS (2013) in Chemical Engineering and Technology from Shandong University and a PhD degree (2018) in Chemical Engineering from Qingdao Institute of Bioenergy and Bioprocess Technology, Chinese Academy of Sciences, under the supervision of Prof. Xindong Mu. He then moved to Prof. Johannes A. Lercher's group at the Technical University of Munich (TUM) to learn zeolite catalysis from 2018 to 2020. He is currently a Postdoc at the ETH Zurich under the supervision of Prof. Jeroen A. van Bokhoven. His research interest focuses on the design and synthesis of advanced nanocatalysts for more efficient processes related to clean and sustainable energy.

Marco Ranocchiari

Marco Ranocchiari received his master's degree in chemistry in 2005 from the Università degli Studi di Milano in Italy. He completed his PhD at the ETH Zurich in 2009. In 2010, he joined the Paul Scherrer Institute in the Laboratory for Catalysis and Sustainable Chemistry and has been a group leader since 2016. His research focuses on energy-related catalysis and metal–organic frameworks for catalytic applications. He is co-founder of the spin-off novoMOF AG (https://novomof.com), a custom MOF manufacturing company.

catalyst deactivation can become more severe under high temperature and/or harsh reaction conditions, *i.e.* in an oxidizing and corrosive environment, which calls for innovative design and optimization strategies to fulfil the requirement of boosting the catalytic properties of supported metal catalysts.

Electrochemical transformation reactions in polymer electrolyte fuel cells (PEFCs) and water electrolyzers (WECs) with high efficiency and long-term durability have remained the hotspot for renewable energy production, conversion and storage.[9–11] In PEFCs, the oxygen (O_2) reduction reaction (ORR) proceeds *via* either the direct $4e^-$ pathway to produce H_2O or the $2e^-$ route by forming hydrogen peroxide (H_2O_2) on the cathode. Oxidation of a fuel molecule, *i.e.* the hydrogen (H_2) oxidation reaction (HOR), proceeds at the anode side of fuel cells. On the other hand, WECs that transform electricity into renewable energy involve the H_2 and O_2 evolution half-reactions (HER and OER), and are operated on the principle opposite to that of PEFCs. At present, platinum (Pt)-group metals (PGMs) are the most active state-of-the-art electrocatalysts, even though 3d transition metal-based nanomaterials are promising alternatives to PGM counterparts. In addition to the high price and scarcity of PGM catalysts, the intensely sluggish kinetics of ORR and OER, along with their intricate reaction pathways, impede the widespread and commercialization of electrochemical devices.[12,13] On the other hand, taking the hydrogen-driven PEFCs as an example, the HOR activity is orders of magnitude higher in an acid electrolyte than that in a basic solution (pH-dependent activity),[14] which allows an ultra-low loading ($\leq 0.05\ \mathrm{mg_{Pt}\ cm^{-2}}$) of Pt on the anodic catalyst when contacting with acid media. However, the instability and degradation of Pt, which show dependencies on catalyst characteristics (such as particle size, crystal structure, loading) and operating conditions (electrolyte, limiting potential, temperature and so on), still constitute important performance-limiting factors.[15,16] In the process of electrocatalyst design, the implicated trade-off relationship between activity enhancement and intrinsic instability is required to be overcome before the practical application of electrode catalysts.

Reducing the usage of PGMs and developing electrochemically highly active and durable materials are the main subjects of intense research on the wide implementation of energy conversion and storage devices.[17–19] Of the numerous efforts, alloying Pt with a second transition metal (*i.e.* Fe, Co, Ni, Cu, Zn) and the fabrication of core–shell nanostructures (where Pt is conformally deposited as an ultra-thin shell on a more abundant metal core) have been proven beneficial for improving the electrochemical performance.[20–25] The alterations of the electronic surface structure of the metal by foreign transition metal atoms and the lattice mismatch-derived strains at the interface of metal nanodomains yield the improvements.[26,27] Nevertheless, synthetically controllable design of catalysts with high specific surface area and maintaining the nanostructure of metal particles are not easy because of sintering and dealloying issues in the process of thermal treatment and catalytic reactions. The high dissolution tendency of alloyed transition metals or non-PGM cores often calls for elaborate selection of transition metals and precise modulation of Pt ''skin''/skeletal as well as morphological integrity and electronic structure.[12,28–30] In terms of developing nanomaterials with enhanced catalytic properties, deploying organic/inorganic barriers or overlayers recently appears to be one of the favourable countermeasures, which promises to reconcile high activity with improved stability of metal entities.[31,32] Polymeric and metal oxide overlayers are the typical coatings that can protect the carbon material (the commonly used catalyst support) from electrochemical oxidation and corrosion, ultimately making the as-synthesized electrocatalysts durable. Moreover, the multiple functions of surface coatings open a plethora of opportunities for enhancing the electrocatalytic efficiencies of nanocatalysts through the as-generated interfacial effects.[33] Thus far, some excellent reviews have discussed the recent development in the design of high-performance metal-based catalysts by using surface engineering strategies and their catalysis related applications.[34–37] For instance, Lenne *et al.*[34] reviewed the surface functionalization of metal catalysts with organic ligands and the consequent influence on their surface properties and catalytic activities for electro-oxidation and reduction reactions. Although another review from the research group of Yin mentioned the synthesis of encapsulated metal catalysts, it mainly reported the works related to the field of thermo-catalysis.[35] In addition, Pt-based materials designed by means of surface-confinement[36] and organic–inorganic hybrid concepts[37] for application covering only ORR catalysis were also reviewed. Benefiting from the ongoing innovative development of advanced synthetic nanotechnology and material chemistry, surface overcoating engineering has emerged as a powerful strategy for the development of optimal metal-based catalysts to unlock their application potential in various electrocatalytic processes. Therefore, it is

Jeroen A. van Bokhoven

Jeroen A. van Bokhoven completed a degree in chemistry at Utrecht University (Netherlands) in 1995 and went on to obtain a PhD in inorganic chemistry and catalysis from the same university in 2000 (with honours). From 1999 until 2002, he was the head of the XAS (X-ray absorption spectroscopy) users-support group at Utrecht University. In 2002, he moved to the ETH Zurich, where he worked as a postdoctoral researcher in the group of Professor Prins. In 2006 he obtained an SNF assistant professorship in the Department of Chemistry and Applied Biology. He is the 2008 recipient of the Swiss Chemical Society Werner Prize. Since 2010, Jeroen A. van Bokhoven has been a Chair in Heterogeneous Catalysis at the Institute for Chemical and Bioengineering at ETH Zurich and the Head of Laboratory for Catalysis and Sustainable Chemistry at Paul Scherrer Institute.

increasingly crucial to offer a critical overview of the potential synthesis methods for surface overcoating of advanced precious and non-precious metal based electrocatalysts for application in diverse important electrocatalytic reactions in PEFCs and WECs.

In the present review, we showcase a comprehensive summary of the versatile surface overcoating strategy for electrocatalyst design with a special focus on their applications in the research of PEFCs and WECs. Specifically, the fabrication of the surface of metal nanoparticles and the modification of support materials (such as carbon and metal oxides) based on a vast variety of overcoating methodologies are surveyed. High-temperature solid oxide fuel cells will not be covered in this review, although there are a number of works on capping Pt electrodes with a metal oxide overlayer for stabilizing the catalyst surface and improving their catalytic performance.[38–40] Next, we discuss the progress of surface overcoating-derived efficient electrocatalysts for PEFCs that involve electrochemical reactions such as ORR, HOR, and MOR/EOR (in direct alcohol (*i.e.* methanol, ethanol) fuel cells, DAFCs) and WECs comprising OER, HER and overall water splitting. The consequent benefits from surface overcoating engineering are considered and the electrocatalysts surveyed include both precious and non-precious metal based electrocatalysts. Finally, we describe the future research opportunities and perspectives associated with the design and deep exploitation of emerging heterogeneous catalysts fabricated by surface overcoating engineering.

2. Surface overcoating methodologies for the nanostructuring of metal based electrocatalysts

In this section, surface overcoating methodologies for the nanostructuring of high-performance electrocatalysts employed in the research of PEFCs and WECs are overviewed. As depicted in Fig. 1, the nanofabrication of metal NPs as well as the modification of catalyst supports (such as carbon materials and metal oxides) through surface overcoating engineering by the utility of different foreign coatings, including organic capping agents/polymers, inorganic carbon nanoshells and metal oxides, is summarized and discussed in the following.

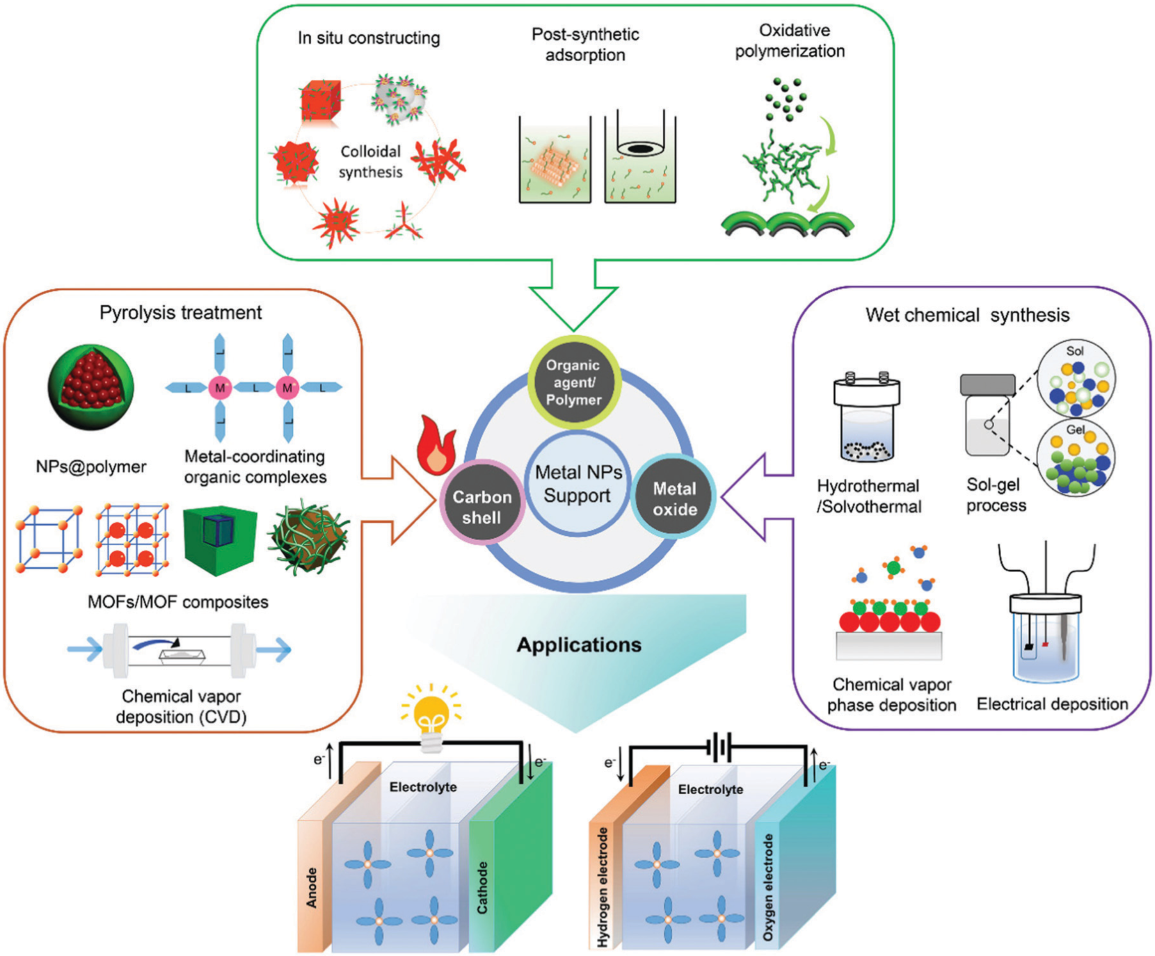

Fig. 1 Overview of a variety of overcoating methodologies utilizing organic agents/polymers, inorganic carbon nanoshells and metal oxides as overcoating materials for high-performance electrocatalysis.

2.1 Overcoating of metal nanoparticles with organic capping agents and polymers

Organic capping agents and polymers on metal surfaces are difficult to stabilize and are prone to decompose at high temperature (*i.e.* >300 °C) under thermal catalysis conditions.[41] By contrast, surface modification of metal particles with organic species without the need of chemical- or thermal-removal has proven effective at enhancing electrocatalytic performance.[34,36,37,42,43] Creating metal–organic structures is effective in modulating the electronic structure of the metal and alleviating the surface site-access blockage due to the adsorption of poisonous spectator species (*i.e.* Cl^-, Br^-, OH^-, PO_4^{3-}, SO_4^{2-}) and crossover-obtained reactants (*i.e.* methanol, ethanol).[34,37] This section will first start by presenting the synthetic approaches for overcoating metal NPs with organic capping agents and polymers.

2.1.1 *In situ* adsorption through metal nanoparticle colloidal reduction synthesis. Surfactants, also known as capping agents, have been exploited for the design of highly efficient electrocatalysts by deploying the molecular patterning concept.[37,44] It can be achieved through metal nanoparticle colloidal reduction synthesis. As illustrated in Fig. 2a, in the presence of surfactant molecules, metal precursors dispersed in a solution get reduced by a reductant to form highly dispersed metal NPs. Simultaneously, it causes the deposition of the metal onto the carbon material to afford carbon-supported metal NPs surface-patterned with organic molecules. The *in situ* deployed surfactant molecules are not only favourable for metal dispersion during the colloidal synthesis,[45,46] but also serve as performance promotors when metal catalysts are applied in catalysis. As the patterned organic molecules could make the metal surface sterically crowded (the so-called "third-body effect"), the adsorption of poisonous species (PO_4^{3-},[44] CO[47]) on active surface sites is hindered resulting in enhanced catalytic activity. The improvements in electrochemical performance are, in essence, reliant on the suitable choice of organic capping agents because they can have large impacts on the intrinsic structural property of metal entities, alter the electron transfer between the metal and the carbon support, and modify the adsorption behaviour of key intermediates on the surface of the catalyst.[48–50]

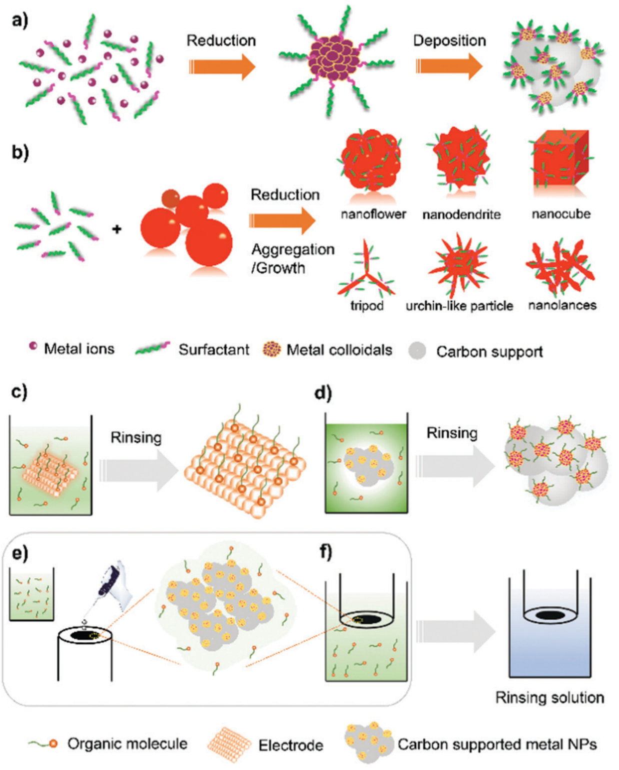

Fig. 2 (a) Synthetic procedures for the preparation of carbon-supported metal NPs patterned with organic surfactants *via* the colloidal reduction method. (b) The synthesis of Pt-based nanostructures with different compositions, shapes and morphologies through chemical reduction routes. (c–f) Schematic illustration of the procedures for the post-synthetic construction of organic architectures on the surface of electrocatalysts.

Surfactants are also useful for engineering metal nanostructures (NSs). It is possible to realize enhanced electrocatalytic properties by utilizing the synergistic effects between the unique metal NSs and the electronic modification by surfactants on the surface.[51–57] Recently, intensive works by the research group of Chen and Lee have pointed to the development of various Pt-based NSs through chemical reduction routes using polyallylamine hydrochloride (PAH) as the metal particle stabilizing and shape/morphology controlling agent (Fig. 2b). A number of polyallylamine (PAA)-functionalized Pt-based NSs, including Pt nanocubes,[52] Pt–Pd alloy nanoflowers,[53] highly branched Pt nanolance assemblies,[54] Pd–Pt bimetallic core–shell nanodendrites,[55] long-spined sea-urchin-like Pt nanostructures (Pt-LSSUs),[56] and Pt tripods,[57] have been reported for efficient electrocatalysis. Solution pH (∼0.5–9), temperature, and the amount and type of reduction agents (such as formaldehyde, hydrazine hydrate) are critical parameters for control over the shapes and morphologies of metal NSs. For instance, sea urchin-like Pt-LSSUs characterized by a three-dimensional (3D) interconnected structure and a high branching degree were formed by using hydrazine hydrate ($N_2H_4{\cdot}H_2O$).[56] In an alkaline aqueous solution, K_2PtCl_4 as a Pt precursor was mixed with PAA by heating at 80 °C. The formation of Pt-LSSUs was started after adding the $N_2H_4{\cdot}H_2O$ reductant. As the $-NH_2$ groups of PAA could selectively cap Pt{100} facets, the fast reduction kinetics favours the selective deposition of Pt atoms in the ⟨111⟩ direction with high growth rates, leading to the formation of Pt branches dominated by {111} facets and surface-functionalized with PAA molecules. The adsorption of PAH on metal NSs through metal–N chemical bonding can be verified by performing catalyst characterization techniques such as energy-dispersive X-ray mapping (EDX-mapping) and X-ray photoelectron spectroscopy (XPS). In most cases, PAH molecules are found loosely packed on the surface of Pt NSs, making it possible for the permeation of the electrolyte without disturbing electrocatalytic processes.

2.1.2 Post-synthetic construction of organic architectures on metal catalysts. For surface organic-modified metal catalysts, a facile immersion of the electrocatalyst, *i.e.* Pt/C or metal catalyst-based electrode, in organic solutions followed by a rinsing step is also a well-recognized protocol (Fig. 2c, d and f).[58–64] As such, chemically adsorbed or assembled organic molecules with tunable coverage on the surface of the metal are generated. Similar to the direct colloidal reduction synthesis, this strategy relies on the fact that organic molecules are prone to chemically coordinate with metal entities on the surface. Marković's group prepared a cyanide (CN^-)-patterned Pt electrode by immersing Pt in 0.1 M (mol L^{-1}) KCN solution.[59] The arrangement of adsorbed cyanide groups renders the surface of Pt sterically hindered towards adsorbates, leading to a strengthened ORR electrocatalysis. The same group constructed a self-assembled monolayer of calix[4]arene with different coverage (84%, 95%, 96%, 98%) on a platinum anode by immersing the platinum anode in a tetrahydrofuran solution of calix[4]arene with a varied concentration of 90, 130, 250, and 400 μM for a period of 24 h.[60] The unmodified Pt step-edges with a very small amount were speculated to be the only accessible sites to electrolyte components after covering with the calix overlayer. In a similar manner, Chen's group[58,62] demonstrated that interface engineering on Pt nanodendrites (NDs) and Ni_2P nanosheets using amine (1,10-phenanthroline monohydrate (PM)) or polyamine (polyethylenimine (PEI)) molecules benefited their electrocatalytic properties. Organic PEI and PM molecules were loosely packed by occupying 31–34% of the Pt surface area without blocking the accessibility of reactants to metal sites.[62] Due to the strong coordination ability of $-NH_2$ or –N– groups, PEI and PM appeared to link with the metal surface. Apart from the commonly used dipping method noted above, directly pipetting an organic solution onto an as-made metal electrode is also a practical choice to yield surface organic-modified metal electrode catalysts (Fig. 2e).[64]

2.1.3 Overcoating of metal nanoparticles with polymer layers. Polymeric coatings with high ionic conductivity such as polyaniline (PANI) and polypyrrole (Ppy) could be fabricated onto the surface of metal particles as homogeneous thin films (Fig. 3a). In an earlier instance, Chen *et al.*[65] coated the PANI overlayer onto commercial Pt/C to prepare the Pt/C@PANI catalyst featuring a core–shell nanostructure. In an acidic H_2SO_4 solution dispersed with Pt/C, the synthesis started with the direct oxidative polymerization of the aniline monomer by dropwise addition of ammonium peroxodisulfate ($(NH_4)_2S_2O_8$, APS) under an ice bath condition (<5 °C). Changing the mass ratio of aniline to Pt/C allows the thickness of the PANI layer to be controlled. PANI with 5 nm thickness is able to embed Pt NPs on the surface of the carbon support. PANI-overcoated Pt nanocube assemblies,[66] hybrid Pd/PANI/Pd sandwich-structured nanotube arrays[67] and ultra-thin PANI-coated Pt–Ni nano-octahedra[68] have been synthesized by following a similar oxidative polymerization process. Electrochemical performance follows the change in PANI thickness; a thinner PANI layer (0.6 nm) is more beneficial for the markedly improved electrocatalytic activity towards methanol oxidation than a thicker layer.[68]

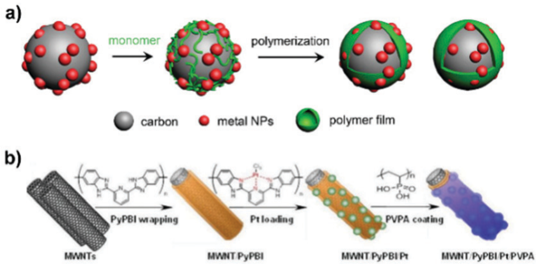

Fig. 3 Schematic illustration of the synthesis of polymer-overcoated electrocatalysts. (a) M/C@polymer (M: metal) synthesized by the oxidative polymerization of organic monomers. (b) Polymer double-shelled Pt-based material prepared through sequential overcoating with PyPBI and PVPA. Reproduced from ref. 75 with permission from Springer Nature. Copyright 2015.

Polydopamine (PDA) coating also manifests wide applications because of its robust structure and strong adhesive strength to the surface.[69–71] One commonly applied synthetic procedure for PDA overcoating is the oxidative polymerization of dopamine in Tris–HCl buffer solution (Trizma base + hydrochloric acid, pH 8.5) dispersed with the solid catalyst at room temperature, followed by sequential separation, rinsing and drying steps. Controlling the polymerization time allows for tuning the thickness of the PDA overlayer. PDA overcoating is more controllable due to the mild polymerization condition as compared to PANI and Ppy coating.[69]

From the research works of Yang *et al.* and Nakashima *et al.*, the wrapped pyridine-containing polybenzimidazole (poly[2,2′-(2,6-pyridine)-5,5′-bibenzimidazole], PyPBI) on a carbon support serves as the glue for highly dispersed Pt NPs.[72,73] When multiwalled carbon nanotube-supported Pt NPs are overcoated with a PyPBI layer, their electrocatalytic oxidation performance is favoured.[74] Based on these advances, they demonstrated a distinct type of polymer double-shelled electrocatalyst, of which the metal particles and carbon support are separately overcoated with polymer layers.[75] As illustrated in Fig. 3b, the steps in the fabrication of a polymer double-shelled electrocatalyst include (i) mixing the carbon material with *N*,*N*-dimethylacetamide solution containing PyPBI, (ii) loading Pt NPs onto the PyPBI-wrapped carbon support by a conventional polyol reduction method, and (iii) mixing the above Pt-loaded material with poly(vinylphosphonic acid) (PVPA) aqueous solution. Each step involves the additional separation/rinsing and drying procedure. This strategy is very flexible and can be used to design a large variety of electrocatalysts by elaborate selection of carbon support materials and polymer coatings.[76–79] The reinforcement of electrocatalytic performances *versus* the uncoated catalyst makes it effective in fabricating metal-based nanomaterials with extra modification of polymers.

2.2 Overcoating of metal nanoparticles with inorganic carbon nanoshells

The inorganic carbon nanoshell doped with heteroatoms (such as N, P, S, B, *etc.*) is another widely exploited overcoating material as in most cases it is capable of improving catalyst's electrical conductivity and providing additional active surface sites for electrocatalysis. In this section, we will discuss a wide assortment of synthetic protocols being developed for overcoating carbon nanoshells on the surface of metal NPs as the emerging efficient electrocatalysts.

2.2.1 Pyrolysis of the polymer overlayer or heteroatom-containing compounds on carbon-supported metal nanoparticles.

Polymers are carbon-rich substances composed of abundant heteroatoms, making them suitable precursors for heteroatom-doped carbon materials. High-temperature carbonization of the polymer layers preovercoated on carbon-supported metal NPs has thus far been the most approbatory method to prepare carbon nanoshell-coated electrocatalysts.[80–83] Guo *et al.*[83] overcoated a nitrogen-doped graphitic carbon (CN_x) shell on Pt/CNT (CNT: carbon nanotube) *via* the sequence of aniline oxidative polymerization, high-temperature pyrolysis, *in situ* reduction and H_2SO_4-assisted leaching process (Fig. 4a). In this work, the immobilization of Pt and polymer coating were integrated into a one-pot process. Adding $(NH_4)_2S_2O_8$ as an oxidant into the dispersion of aniline, CNT and H_2PtCl_6 helped in the formation of the polyaniline overlayer on the surface of the CNT to encapsulate Pt species. On pyrolysis at 900 °C in argon, Pt species got reduced into highly dispersed Pt NPs and were overcoated concurrently by the *in situ*-generated carbon layer, resulting in limited probability of metal species sintering into larger particles. Transmission electron microscopy (TEM) of Pt@CN_x/CNT indicated that more than 71% of Pt NPs were encased by carbon layers, while the others exhibited a partially exposed surface. The porous structure featured by carbon layers serves as the rewarding functionality, allowing for the free diffusion of oxygen and the accessibility of the electrolyte to metal active sites.

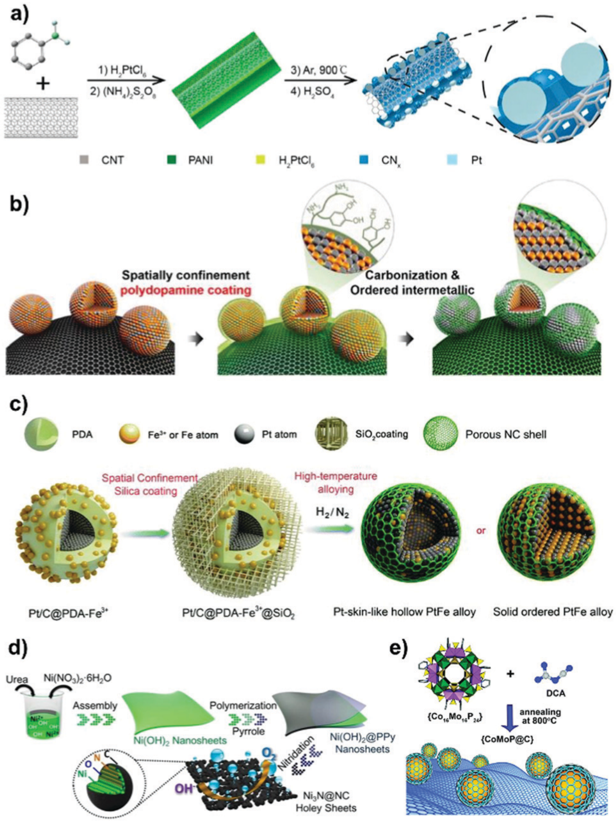

Fig. 4 Carbon nanoshell-overcoated electrocatalysts. (a) Pt@CN_x/CNT was partially covered with a PANI-derived N-doped carbon shell through the one-pot process. Reproduced from ref. 83 with permission from American Chemical Society, Copyright 2015. (b) Ordered face-centered tetragonal PtFe NPs were obtained by PDA overcoating and carbonization. Reproduced from ref. 89 with permission from American Chemical Society, Copyright 2015. (c) Synthesis of PtFe alloy NPs with an ordered or hollow nanostructure through PDA overcoating and the spatial confinement effect by SiO_2 outer coating. Reproduced from ref. 92 with permission from Royal Society of Chemistry, Copyright 2019. (d) Synthesis of N-doped carbon overcoated Ni_3N holey sheets through the polymerization of pyrrole on $Ni(OH)_2$ nanosheets and the followed high temperature carbonization–nitridation step. Reproduced from ref. 100 with permission from American Chemical Society, Copyright 2018. (e) Direct pyrolysis of the mixture of dicyandiamide and P-rich polyoxometalate to obtain CoMoP@C. Reproduced from ref. 110 with permission from Royal Society of Chemistry, Copyright 2017.

In terms of overcoating with carbon nanoshells, the optimization of the pyrolysis temperature and carbon nanoshell thickness with the aim of improving electrocatalytic properties is in high demand. A comparison with pyrolysis at lower temperatures, *i.e.* 600 and 700 °C, indicates that pyrolysis at higher temperature (900 °C) is a good practice to generate carbon nanoshells with a higher degree of graphitization; consequently, the corrosion-resistant carbon nanoshell confers high durability on the resultant catalyst.[84] However, care should be taken on the issues related to metal nanoparticle aggregation/sintering and the loss of active surface area at even higher pyrolysis temperatures.

A carbon nanoshell with thickness that is either too thin or too thick will either weaken the protection effect on metal NPs, or kinetically influence reactant transfer from the outer phase into the inner active sites.[85] Tong *et al.*[86] precisely tuned the carbon overlayer thickness by controlling the growth of the glucose-containing polymer on Pt/CNTs. It is worth noting that the electrochemical surface area (ECSA) is the accessible area of electrode catalysts to electrolyte components and reactants for catalyzing electrocatalytic reactions. In this work, a thick carbon nanoshell (2 nm) induces 5 times lower ECSA of Pt/CNTs@C compared to uncoated Pt/CNTs. In contrast, the diffusion of oxygen is facilitated on the catalyst overcoated with a 0.8 nm-thin carbon nanoshell for the process of ORR catalysis.

Fabricating ordered Pt-enriched nanoalloys or core–shell nanostructures could fulfill the on-demand requirements of reducing precious Pt loading and improving electrochemical efficiencies.[87,88] However, high-temperature annealing treatment on Pt-based nanoalloys usually induces the formation of larger metal NPs with broad size distributions. It results in extremely deteriorated ECSA and inefficient utilization of active surface sites. Impressively, the *in situ* overcoating of the carbon nanoshell onto metal nanoparticles is able to minimize the aggregation and sintering of metal NPs during annealing treatment. For example, the *in situ* carbonization of the PDA overlayer on carbon-supported PtFe NPs resulted in a metal particle size close to that before annealing treatment (Fig. 4b).[89] By contrast, the catalyst without dopamine coating underwent obvious particle coalescence, forming particles up to tens of nanometers in size. Based on the protective aid of PDA, Pt-rich

PtNi alloy particles without a carbon nanoshell were synthesized by pyrolyzing the Ni^{2+}-impregnated Pt/C–PDA composite under a H_2-containing atmosphere.[90] In addition to improvement in the resistance of metal NPs to sintering, it was shown in this work that PDA also behaved as a sponge to adsorb Ni ions for a precise control over the Pt–Ni ratio in the resulting Pt-alloyed electrocatalyst.

A space-confined pyrolysis strategy was recently developed by Wei's group[91,92] to prepare carbon nanoshell-coated PtFe NPs with ordered or Pt-skin-like hollow structures (Fig. 4c). In catalyst synthesis, commercial Pt/C (20 wt% loading of Pt with a diameter of 2–4 nm) was initially overcoated with an oxidatively polymerized PDA overlayer based on the procedure described in Section 2.1.3. After dispersing Pt/C@PDA in an aqueous solution containing Fe^{3+}, the outer-coating of the inorganic SiO_2 shell on the catalyst was proceeded by the hydrolysis and polycondensation of tetraethoxysilane (TEOS) catalyzed by HCl in a water/ethanol mixture, followed by the slow evaporation of solvents. Upon annealing treatment, PDA overlayers get transformed into a 2 nm-thin N-doped carbon shell, and the outer silica shell provides a spatially confined space to avoid metal NP aggregation/sintering, while the first formed PtFe alloy intermediates undergo subsequent phase transition, which can be controlled by modulating the content of Fe^{3+} and annealing temperature during the synthesis process.[92]

In addition to polymers, heteroatom-containing organic compounds such as thiourea and cyanamide have also become the precursor of choice to yield the heteroatom-doped carbon nanoshell on supported metal nanoparticles. For example, Chen *et al.*[93] prepared a Fe@S,N-DC catalyst *via* two major steps: (i) pyrolysis of activated carbon in the presence of thiourea (CH_4N_2S) to obtain the S,N-codoped carbon support (S,N-DC) and (ii) embedding Fe NPs into the carbon matrix by microwave radiation treatment of $Fe(OAc)_2OH$ and hexamethylenetetramine, which serve as Fe and N,C sources, respectively. Jin *et al.*[94] synthesized a graphene-supported g-C_3N_4@CoO core–shell catalyst, consisting of a CoO core and a Co-doped g-C_3N_4 (graphitic carbon nitride) outer nanoshell, through pyrolysis of the mixture of cyanamide-Co complex and graphene oxide support at 550 °C.

2.2.2 Direct pyrolysis of metal–polymer composites or metal-coordinating organic complexes. Polymers such as PDA,[90–92,95,96] polyvinyl pyrrolidone (PVP),[97,98] resin[99] and Ppy[100–103] have strong metal chelation ability to trap metal ions through their functional groups. The direct pyrolysis of metal–polymer composites in the absence of carbon support provides another route for engineering carbon nanoshell-overcoated electrocatalysts. For example, the Co(II)–PDA composite was first obtained by hydrothermal-assisted polymerization of dopamine in aqueous solution in the presence of the $Co(NO_3)_2$ precursor at 150 °C. The following pyrolysis of Co(II)–PDA at 900 °C in N_2, along with a mild heating treatment at 90 °C in air, resulted in the overcoating of Co@Co_3O_4 core–shell NPs with a N-doped graphitic carbon nanoshell.[96] Likewise, Yuan *et al.*[100] demonstrated that N-doped carbon-overcoated Ni_3N holey sheets (Ni_3N@NC) were generated by a combined synthetic strategy, including solvothermal assembly, polypyrrole wrapping, high-temperature carbonization and nitridation steps (Fig. 4d). With the added amount of pyrrole being controlled, the thickness of the NC shell overcoated on Ni_3N sheets varied within 2–8 nm. The overcoated NC nanoshell on Ni_3N@NC was found to protect the Ni–O oxide layer from over-oxidation, giving rise to enhanced stability towards the alkaline OER catalysis. Moreover, Wang *et al.*[103] developed N,O-codoped carbon-encapsulated Co NPs, named CoNOC, to be a binder-free electrode for HER application. The electrode was constructed *via* the first growth-deposition of polymeric PAQTA on carbon fiber cloth, then a facile impregnation of $Co(acac)_2$ (acac: acetylacetonate) followed by pyrolysis and acid leaching treatments. PAQTA, as a unique conjugated microporous polymer consisting of anthraquinonylamine and triphenylamine, features intrinsic porosity and a cross-linked network structure, which are beneficial for the high dispersion of Co on the catalyst obtained.

Similar to polymers, organic compounds especially those with heteroatom-containing groups such as $-NH_2$ and –NH– can coordinate with metal ions to form metal-coordinating organic complexes, making them promising precursors for the carbon nanoshell and the support of metal NPs.[104–108] For example, a one-step high pressure pyrolysis of ferrocene and cyanamide at 700 °C was reported by Hu *et al.*[104] to prepare Fe_3C/C hollow spheres overcoated with 4–9 layers of graphitic carbon. A negligible amount of nitrogen and Fe metal was observed on the surface of Fe_3C/C, indicating that it was another mechanism rather than that catalyzed by Fe–N_x moieties that accounted for the high ORR activity. The removal of the carbon nanoshell induced dissolution of Fe_3C into the electrolyte accompanied by an obvious ORR activity loss. The authors therefore claimed that Fe_3C sites did not have direct contact with the electrolyte but instead made the outer carbon nanoshell active for the ORR catalysis. Analogously, trimetallic FeCoNi alloys overcoated with N-doped carbon nanotubes were generated following the protocol of direct pyrolysis of dicyandiamide–metal nitrate complexes at 800 °C in an inert atmosphere.[106]

Such a versatile strategy has made it possible to elaborately select platform compounds such as the phosphorus (P) moiety-coordinated counterparts to produce metal phosphides with surface overcoating of carbon nanoshells.[108–111] For example, Pu *et al.*[108] prepared a N,P-codoped carbon-encapsulated ruthenium diphosphide catalyst (RuP_2@NPC) by pyrolysis of phytic acid (PA) cross-linked Ru complexes and melamine at 900 °C. In the work of Lv *et al.*,[109] cobalt phosphonate hybrid precursors were first fabricated by hydrothermally treating the mixture of cobalt chloride and sodium salt of ethylene diamine tetra-(methylene phosphonic acid) (EDTMPS) at 140 °C. Subsequently, the phase-controlled Co_xP@NC was obtained by H_2 reduction of as-made precursors with different Co/P molar ratios at 700 °C. In addition, Ma *et al.*[110] demonstrated that a carbon nanoshell-coated CoMoP@C catalyst was generated through pyrolysis of the mixture of P-rich polyoxometalate ($Co_{16}Mo_{16}P_{24}$) and dicyandiamide (DCA) at 800 °C in a N_2 atmosphere (Fig. 4e). DCA not only serves as a reducing agent to catalyze the deoxygenation of $Co_{16}Mo_{16}P_{24}$, but also protects the CoMoP particles from aggregation during the process of carbonization and *in situ* phosphidation. In the engineered CoMoP@C, the single crystalline CoMoP core with the overcoated 2–4 graphitic carbon layer is favourable for electrocatalytic reactions. We note that, it is also applicable to generate metal phosphide catalysts by carrying out post-phosphorization treatment on as-made metal@C materials using *e.g.* NaH_2PO_2 as the P source at moderate-to-high temperature.[112]

2.2.3 Pyrolysis of metal organic frameworks (MOFs) and MOF nanocomposites. Increasingly, MOFs and MOF nanocomposites are gaining in popularity for the rational fabrication of nanocatalysts for efficient application in energy conversion and storage technologies.[113–115] The high diversity of tunable metal nodes and organic linkers endows MOFs with unique compositional and structural properties. Pyrolysis of MOFs and MOF nanocomposites is one of the most popular strategies for the synthesis of MOF-derived carbon nanomaterials with highly exposed active sites, a facilitated charge/electron transfer process and a robustness feature, which constitute the inherent aspects determining their electrocatalytic properties.

Direct pyrolysis of the MOF nanostructure can feasibly aid in isolating metal sites within the MOF-derived carbon matrix with a large surface area.[116–120] Metal nodes in MOFs could serve as the source of metal NPs, while the organic linkers transform into a porous carbon matrix and affect the composition of encapsulated metal entities after high-temperature pyrolysis. Shi *et al.*[118] developed a MOF-directed strategy to synthesize a graphitic carbon nanoshell-coated MoC electrocatalyst (named nanoMoC@GS) with high porosity. As illustrated in Fig. 5a, $Mo(CO)_6$ is first mixed with trimesic acid (H_3BTC) in an oxygen-free dimethylformamide (DMF) solvent and then solvothermally treated under argon to form $Mo_3(BTC)_2$. Subsequently, carbonization of $Mo_3(BTC)_2$ at 700–900 °C under an inert atmosphere yields nanoMoC@GS. Metal carbides are formed by the diffusion of carbon atoms into the interstices of metal atoms, which atomically contact with the organic linkers in MOFs.[118,120] This atomic interaction can effectively make metal NPs highly resistive towards aggregation during the carbonization process.

In addition, the transition metal moieties such as Co and Fe in MOFs could catalyze the formation of carbon nanotubes (CNTs) under pyrolysis conditions, helping in obtaining CNT-encapsulated metal based catalysts.[119,120] For example, Co-containing ZIF-67 polyhedra (ZIF: zeolitic imidazolate framework) were pyrolyzed at 900 °C in a H_2 atmosphere, along with low-temperature phosphatization treatment to produce N-doped carbon nanotube (NCNT)-embedded CoP NPs dispersed on carbon polyhedra (500 nm of average diameter) (Fig. 5b).[119] In the process of carbonization, Co ions get reduced into metallic Co, which could promote the formation and growth of NCNTs. Subsequently, on phosphatization treatment, metallic Co species react with the PH_3 species generated from the decomposition of NaH_2PO_2, leading to the formation of CoP NPs encased in NCNTs, which is underpinned by high resolution TEM (HRTEM) analysis.

Prussian blue analogues (PBAs) with the chemical formula $K_3[M(CN)_6]$ or $M_3^{II}[M^{III}(CN)_6]_2$ (where M represents the transition metals), as a subclass of MOFs, have been investigated to fabricate carbon nanoshell-overcoated electrocatalysts with promising catalytic properties.[121–124] One can additionally supplement active sites by introducing metal precursors during the synthesis of PBAs to design well-alloyed or core–shell nanostructures. In an exemplary work reported by Jiang *et al.*,[124] an Ir-doped Prussian-blue analogue ($Co_3[Co(CN)_6]_2$) was first prepared by mixing the H_2IrCl_6 precursor with $Co(CH_3COO)_2$, $K_3[Co(CN)_6]_2$ and PVP in an aqueous solution, followed by hydrothermal treatment at 100 °C for 5 h. On direct pyrolysis, IrCo@NC was generated composed of N-doped graphene shell-overcoated IrCo alloy NPs. The CN^- groups from the PBA served as the source of carbon and nitrogen during the annealing treatment. As a consequence of the phase transformation of Co moieties at elevated temperatures, regulation of the structure phase of IrCo NPs can be achieved. In this work, the lower temperature-pyrolyzed catalyst, *i.e.* IrCo@NC-500, was characterized to possess a hexagonal IrCo phase with surface covering of the N-enriched graphene overlayer. The graphene overlayer was able to transfer the adjacent carbon atoms into catalytic active sites and form strong interactions with the encapsulated metal NPs. Similarly, binary transition metal-based FeCo@C[125] and NiFe@C[126] have been generated following the protocol of annealing a wide assortment of PBA-based nanomaterials.

The unique pore structures and interconnected channels of MOFs render them as promising hosts for introducing catalytic metal moieties. An example of this is the direct pyrolysis of fabricated polyoxometalate (POM)-incorporated MOF materials, which could make the introduction of transition metals into metal carbide electrocatalysts feasible. In this sense, POMs serve as the metal sources, while MOFs get transformed into a carbon matrix with additional metal sites after carbonization. Li *et al.*[127] reported for the first time the synthesis of a Fe_3C/Mo_2C-containing N,P co-doped carbon catalyst by pyrolyzing POM@MOF-100(Fe) with melamine (Fig. 5c). The POM@MOF-100(Fe) precursor was intentionally synthesized by hydrothermally treating the mixture of $FeCl_3$, $H_3PMo_{12}O_{40}$ and trimethyl 1,3,5-benzenetricarboxylate at 130 °C for 72 h, followed by sequential centrifugation, washing and drying steps. POM@MOF-100(Fe) was then mixed with melamine by ball milling before the pyrolysis treatment. Melamine provides the source of carbon and nitrogen, while the Fe species derived from MOF-100(Fe) catalyzes the formation of graphitized carbon during the process of carbonization. Subsequent HRTEM and EDX-mapping images verified that the confinement effect of MOF-100 benefited the high dispersion of Mo_2C NPs, which were overcoated with uniform graphitic carbon layers. The resulted catalyst possessed a characteristic mesoporous structure, facilitating the mass transfer process during catalytic reactions. This work highlights the new opportunities for the design of advanced non-precious metal-based electrocatalysts by the utility of POM-incorporated MOF nanomaterials.

Metal precursors could also be incorporated into the as-synthesized MOFs featured with open channels and large

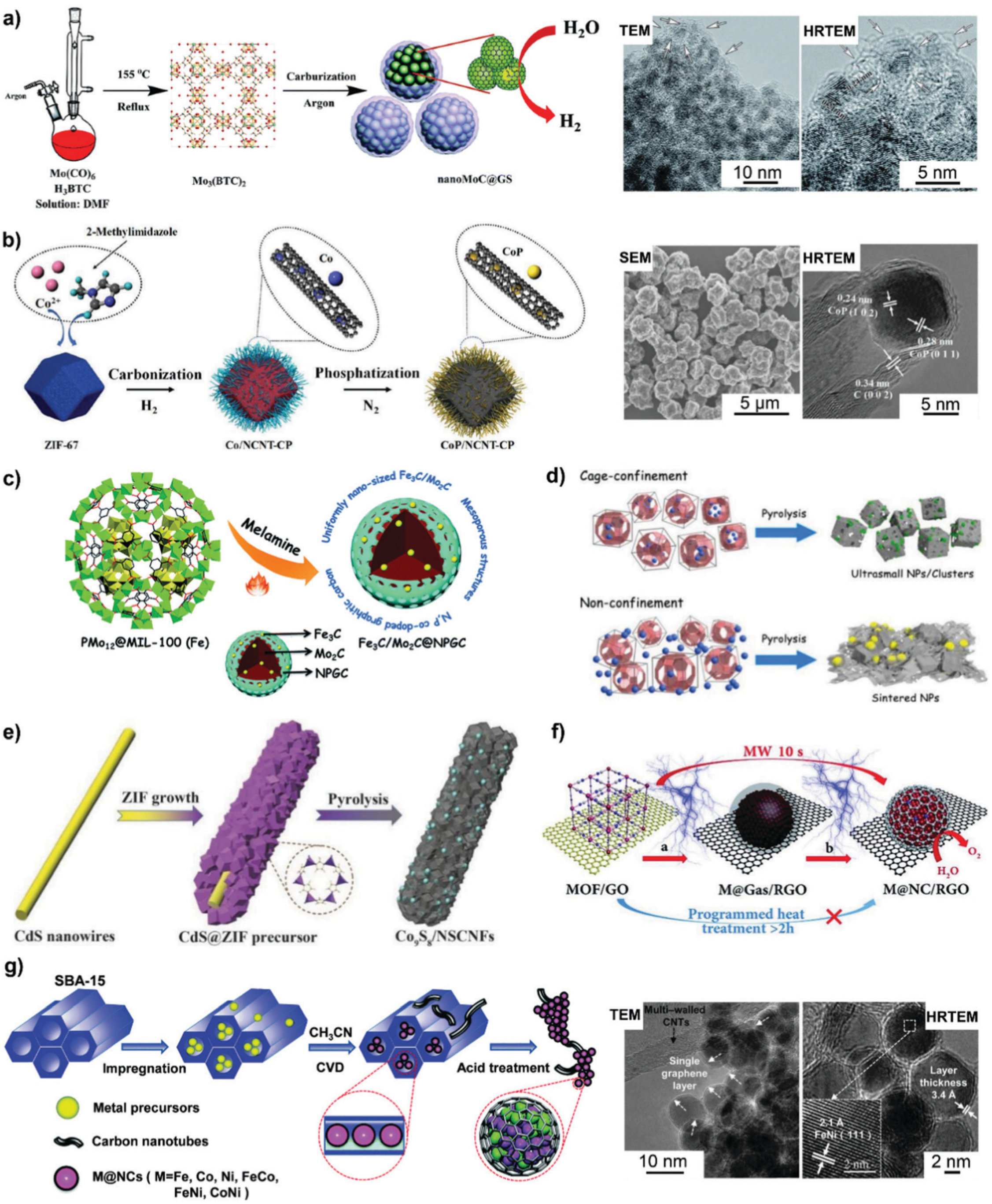

Fig. 5 Carbon nanoshell-overcoated electrocatalysts obtained from MOFs or MOF nanocomposites. (a) $Mo_3(BTC)_3$ MOF synthesis and its carbonization to nanoMoC@GS under 700 °C. Reproduced from ref. 118 with permission from Royal Society of Chemistry, Copyright 2016. (b) CoP/NCNT-CP was prepared by the carbonization of ZIF-67 under H_2 and subsequent phosphatization treatment in N_2. Reproduced from ref. 119 with permission from American Chemical Society, Copyright 2019. (c) N,P-Codoped graphitic carbon-embedded Fe_3C/Mo_2C was obtained through pyrolysis of PMo_{12}@MIL-100(Fe). Reproduced from ref. 127 with permission from Royal Society of Chemistry, Copyright 2016. (d) Ultra-small WC NPs were produced on the basis of cage-confinement of MOFs. Reproduced from ref. 129 with permission from American Chemical Society, Copyright 2017. (e) A synthetic procedure for N,S-codoped carbon fiber embedded Co_9S_8. Reproduced from ref. 132 with permission from Wiley-VCH, Copyright 2018. (f) Ultrafast microwave-assisted CVD-like synthesis of M@NC/RGO. Reproduced from ref. 135 with permission from Royal Society of Chemistry, Copyright 2018. Chemical vapor phase deposition (CVD) also favours the generation of carbon nanoshell-overcoated electrocatalysts. (g) Graphene layer-overcoated transition metal or metal alloy NPs obtained by CVD technology. Reproduced from ref. 136 with permission from Royal Society of Chemistry, Copyright 2016.

pores by using suitable post-synthesis approaches.[128,129] The confinement effect of MOF nanomaterials is beneficial to form more uniform dispersion relative to that of metal NPs supported on open-structured solid materials. As a typical example, in order to rationally avoid WC sintering into larger particles during high-temperature synthesis, Xu *et al.*[129] developed a cage-confinement pyrolysis route where MAF-6 (rho-[Zn(eim)$_2$]) was selected as a host to isolate the guest metal sites-W(CO)$_6$ (Fig. 5d). Compared to the *in situ* mixing method, a low-temperature vapor adsorption procedure, that is, heating the mixture of MAF-6 and W(CO)$_6$ in a sealed setup at 85 °C for 24 h, was more effective for the confinement and isolation of W(CO)$_6$ within the MAF-6 framework to form W(CO)$_6$@MAF-6. Subsequently, WC@NPC was yielded through the carbonization of the W(CO)$_6$@MAF-6 precursor at 980 °C in N$_2$ for 5 h. Owing to the pivotal role of the cage-confinement effect, WC with much smaller particle size (*ca.* 2 nm) relative to most reported metal carbides was coated with 1–2 graphitic carbon layers.

Combining MOFs with other structure-oriented materials provides the route for fabricating complex composites with multiple compositions and specific nanostructures.[125,130–135] For example, coating MOFs with a polymer overlayer could prevent the aggregation of MOF-derived NPs during pyrolysis.[131] PVP-coated NiFe-PBA[131] and NiFeMn-PBA[134] could be transformed into a unique 3D network composed of N-doped carbon-overcoated heterojunctions after carbonization, compared to that generated without the hybrid PVP polymer. In addition, Wu *et al.*[132] reported a facile method to realize the formation of Co$_9$S$_8$ NPs encapsulated by N,S-doped carbon nanofibers (Fig. 5e). CdS@ZIF hybrids (ZIF polyhedra-wrapped CdS nanowires) were first prepared by quickly pouring the methanolic solution of 2-methylimidazole (2-MIM) and PVP into the mixed solution of zinc nitrate/cobalt nitrate and CdS nanowires. On pyrolyzing the CdS@ZIF precursor in an inert atmosphere, the ZIF shell was transformed into a Co,N-codoped carbon matrix. Concomitantly, CdS got reduced into evaporable Cd and S; the latter can be doped into the carbon matrix and react with Co species for the generation of N,S-doped carbon nanofiber-encapsulated Co$_9$S$_8$ NPs with uniform dispersion. HRTEM measurements validated the overcoating of Co$_9$S$_8$ NPs with a few carbon layers, which have an interplanar spacing of 0.34 nm. The obtained nanocatalyst shows the features of a large surface area and a mesoporous structure, resulting in abundant accessible active sites and a fast mass transfer process for electrocatalytic OER catalysis.

Furthermore, Bu *et al.*[135] demonstrated that graphene oxide (GO) was employed in an ultrafast microwave-assisted route for converting PBA nanomaterials into N-doped graphene shell-coated transition metal NPs (*i.e.* FeCoNi, CoNi, FeNi, Co) supported on reduced GO (RGO) (Fig. 5f). This strategy induces the decomposition of PBAs into metals and carbon- and nitrogen-containing gases. The *in situ* formed gases could deposit onto the surface of the metal *via* a so-called chemical vapor deposition-like process, which is dramatically different from the conventional programmed heating procedure. During this well-controlled process, GO gets reduced into RGO and works as a microwave susceptor by rapidly creating heat to promote the uniform conversion of PBA nanomaterials within a seconds time. RGO could also facilitate the high dispersion of metal NPs derived from PBA nanomaterials. This strategy developed in this work is simple and controllable, which will expand the application in the synthesis of other kinds of metal@NC materials.

2.2.4 Chemical vapor deposition of the carbon nanoshell onto metal nanoparticles.

Chemical vapor deposition (CVD) is also effective for the design of carbon nanoshell-overcoated metal electrocatalysts. For instance, Cui *et al.*[136] applied a CVD strategy to prepare single layer graphene-encapsulated earth-abundant 3*d* transition metal NPs (Fe, Co, Ni, or metal alloys) (Fig. 5g). Ordered mesoporous silica SBA-15 serves as the template as it is crucial for the uniform distribution of metal NPs because of the confinement effect. In the catalyst synthesis process, transition metal precursors are first filled into the SBA-15 channel by using an impregnation method in methanol solution. The sample is then subjected to reduction and annealing treatment in a H$_2$/Ar atmosphere by increasing the temperature to 700 °C, which is followed by CVD of CH$_3$CN – the source for the carbon nanoshell – on the surface of as-formed metal NPs for a period of 20 minutes. Acid etching of SBA-15 results in the generation of graphene overlayer-encapsulated non-precious metal NPs with high dispersion. Following the developed CVD strategy, a further oxidation treatment at moderate temperatures could partially decompose the surface graphene layer to create a unique interfacial structure between RuO$_2$ and graphene for efficient OER electrocatalysis.[137] The control over the uniformity and/or the thickness of the carbon overlayer on metal nanoparticles is regarded as important in surface overcoating engineering, since the accessibility of inner active sites determines the benefits for electrocatalytic reactions.

2.3 Overcoating of the metal catalyst with inorganic metal oxides

Metal oxides (*i.e.* SiO$_2$ and TiO$_2$) feature the advantages of good thermal stability, high acid resistance and tunable structural porosity, thus, showing potential as overcoating materials for rationally fabricating high-performance electrocatalysts. Metal oxide overlayer-encapsulated materials are an emerging class of electrocatalysts, and the corresponding viewpoint has already been provided by Esposito.[138] The silica overlayer has been reported to improve catalyst durability in the way of stabilizing metal NPs towards out-diffusion and suppressing their migration, agglomeration and sintering under high temperature and/or severe reaction conditions.[139–141] Conventional sol–gel chemistry of silica could help in achieving the overcoating of silica onto the surface of metal catalysts. Takenaka *et al.*[140] coated a silica overlayer onto carbon black (CB)-supported Pt–Co *via* the hydrolysis and polycondensation of TEOS and 3-aminopropyl-triethoxysilane (APTES) in the presence of a base – trimethylamine – followed by a high-temperature calcination step (Fig. 6a). In the overcoating process, APTES with amino groups can strongly interact with the carbon support and the silica precursor derived from APTES provides nucleation sites for the successive hydrolysis of TEOS on the surface of the catalyst.[141] A benefit from silica overlayer coating is that a narrower particle size distribution is obtained on SiO$_2$/Pt–Co/CB than that found with Pt–Co/CB, the sample without

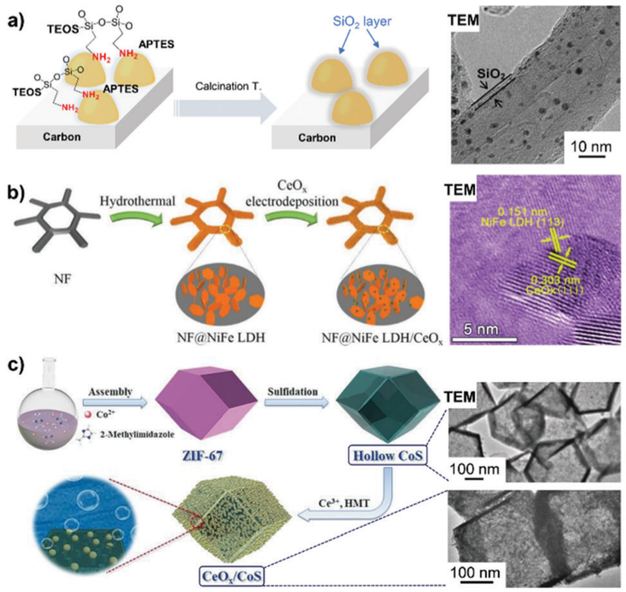

Fig. 6 Inorganic metal oxide-overcoated electrocatalysts prepared by different synthetic methods. (a) Overcoating carbon-supported metal particles with a silica oxide layer by the successive hydrolysis of APTES and TEOS, along with calcination treatment. Reproduced from ref. 141 with permission from American Chemical Society, Copyright 2014. (b) The hydrothermal and subsequent electrodeposition process for obtaining NF@NiFe LDH/CeO$_x$. Reproduced from ref. 144 with permission from American Chemical Society, Copyright 2018. (c) Schematic of the synthesis of hollow CoS particles with surface-covered CeO$_x$ by thermal treatment in the presence of Ce^{3+} precursor and HMT. Reproduced from ref. 145 with permission from Wiley-VCH, Copyright 2018.

the SiO_2 overlayer.[140] Likewise, Pt–Co NPs on SiO_2/Pt–Co/CB are inclined to have a higher alloying degree, whereas those on Pt–Co/CB are prone to agglomerate in the absence of silica.

It is worth noting that the coating of silica would not be simple when unsupported metal NPs are implicated especially those belonging to the smaller particle size regime (<10 nm), owing to the weak interaction and high interfacial energy between metal and silica coating. In this sense, elaborate synthesis approaches are required to fabricate well-controlled core–shell nanostructures in the context of potential application in catalysis, which have been comprehensively reviewed by Gao *et al.*[35]

Kang *et al.*[142] prepared porous TiO_2 thin overlayer-coated Pt NPs by first wrapping as-formed Pt NPs with a $TiO(OH)_2$ layer by the hydrolysis of titanium(IV) butoxide in ammonia-containing ethanol solution. Subsequently, TiO_2-skin on the surface of Pt was attained through annealing treatment at a moderate temperature of 350 °C in an Ar atmosphere, where $TiO(OH)_2$ was allowed to be converted into a TiO_2 overlayer. In addition to the aforementioned wet chemical synthesis approaches, atomic layer deposition (ALD) is becoming an efficient technology for overcoating metal oxides on the surface of metal catalysts. In an exemplified report, Kim *et al.*[143] carried out TiO_2 ALD overcoating on the surface of carbon-supported Co NPs, producing an active OER electrocatalyst after optimizing the thickness of the TiO_2 overlayer by controlling the number of ALD cycles. We will present the brief discussions of the metal oxide ALD process in Section 2.4.3.

Metal oxides also find application in surface overcoating of metal oxide nanosheets,[144] porous and hollow metal-based nanostructures[145] and metal thin film electrodes.[146–149] For example, Wang *et al.*[144] first constructed NiFe layered double hydroxide-coated nickel foam (NF@NiFe LDH) by hydrothermally treating NF in a solution of metal nitrates. CeO_2 NPs were then electrodeposited onto NF@NiFe LDH at a current density of 0.25 mA cm^{-2} in a three-electrode cell to yield the 3D self-supporting NF@NiFe LDH/CeO$_x$ electrode catalyst (Fig. 6b). From the HRTEM images of NF@NiFe LDH/CeO$_x$, a visible interface structure was identified between the NiFe LDH(113) plane and the overcoated CeO$_x$(111) plane. Their local electron potential difference introduced abundant oxygen vacancies, which could promote the electron/charge transfer and create more active surface sites for the alkaline HER. In addition, coating an ultra-thin overlayer of a metal oxide (*i.e.* SiO_2, VO_x and CeO_x) on the metal electrode surface could form a semi-permeable membrane by controlling the transfer of reactants or products to achieve a higher electrical selectivity. As such, electrodeposition of MnO_x thin film onto a glassy carbon-supported IrO_x electrode endowed the OER catalysis with improved efficiency over the chorine evolution reaction in acid solution for potential water splitting application.[146] An example of metal oxide overcoating on porous metal-based nanostructures comes from the report of Xu *et al.*[145] First, an amorphous CoS hollow nanocage was formed by refluxing ZIF-67 particles in an ethanol solution of thioacetamide. Subsequently, a hybrid nanostructure (CeO_x/CoS) was constructed by *in situ* overcoating CeO_x NPs (with an average diameter of 5 nm) onto ZIF-67-derived hollow CoS polyhedra *via* a thermal treatment using $Ce(NO_3)_3$ and hexamethylenetetramine at 180 °C for more than 6 h (Fig. 6c). The resultant CeO_x/CoS nanostructure, containing CoS polyhedra decorated with CeO_x particles, possesses the features of a highly porous structure and a large surface area, which are favourable for electrocatalytic OER activity. It was found that an optimized loading of CeO_x was profitable for tailoring the metal electronic structure, forming a large number of defective sites and limiting the oxidation/dissolution of catalytically active Co species.

2.4 Modification of the carbon support by surface overcoating

Carbon black is the most used low-aspect-ratio support material for PGM electrocatalysts, including Vulcan XC72, Ketjen EC 300J, Ketjen EC 600JD and Black pearls 2000. However, carbon corrosion in terms of electrochemical oxidation ($C + 2H_2O \rightarrow CO + 4H^+ + 4e^-$) and chemical oxidation ($C + H_2O \rightarrow CO + H_2$ or $C + 2H_2O \rightarrow CO_2 + 2H_2$) is a severe issue under shut-down/start-up operating conditions and/or in an oxidizing environment, in addition to the issue of the easy deactivation of supported metal NPs. Moreover, the presence of PGM-based NPs on carbon support materials could accelerate the corrosion of carbon through the oxidation pathways. The literature review highlights that surface overcoating engineering on carbon black and high-aspect-ratio carbon nanotubes can bring in benefits such as mitigation of carbon corrosion, improvement in the dispersion of metal NPs, and formation of strong metal–support interactions. These benefits of surface-overcoating modifications on the carbon support will be discussed in Section 3.5.1. In this section, we showcase the synthetic methodologies being developed for overcoating of carbon support materials with polymers, carbon species, and metal oxides by some representative body of works.

2.4.1 Modification of the carbon support by overcoating with organic polymers. Oxidative polymerization of organic monomers under aqueous/liquid conditions is an efficient approach to wrap the surface of carbon materials with polymer overlayers.[65–68] PANI, for example, is more suitable for performing surface overcoating in comparison with the aniline monomer, owing to its much higher conductivity and stability in acidic solution. PANI can conjugate with carbon nanotubes *via* π-stacking interactions without disrupting the graphitized structure of carbon. As such, PANI serves as a cross-linker between metal NPs and carbon support by forming strong metal–N bonds.[150–152] Ionic-liquid polymers,[153] PDA,[154–156] Ppy,[157] polybenzimidazole (PBI),[78,158–161] PVP,[162] and polyethyleneimine (PEI)[163] have broadened the application of polymers for the surface modification of carbon support materials as well. Intriguingly, it is reported that PDA serves not only as a crosslinking agent, but also as a reductant for the *in situ* reduction and nucleation of metal species without the need of adding any other reducing agents during the synthesis of polymer-modified carbon-supported metal NPs.[155,164,165] In addition to oxidative polymerization, an easy-handling process involving a simple mixing of the carbon support with an organic entity containing solution followed by a thorough rinsing step has been applied for overcoating with PyPBI, PBI and PVP.[78,159–162,166–168] Moreover, by utilizing the amide reaction between the –COOH groups of carbon black and the $-NH_2$ groups of amine-terminated poly(*N*-isopropylacrylamide) (PNIPAM), Jung *et al.*[169] demonstrated the covalent functionalization of the carbon support with polymers for efficient anchoring of metal species. Of note, since the polymer overlayer can strongly interact with the surface of carbon materials, the subsequent metal deposition and coordinating interactions with functional groups (such as N-containing groups) will be feasible.

2.4.2 Modification of the carbon support by overcoating with carbon species. Introducing carbon species onto the surface of carbon materials is also efficient for the stabilization of metal NPs loaded.[83] As illustrated in Fig. 7a, pyrolysis of the preovercoated organic compounds or polymer layers could help in introducing carbon species on carbon-supported catalysts. The surface of metal nanoparticles is again exposed after carbonization without being buried in the carbon shell, leaving the *in situ*-generated carbon at the catalyst "root" to serve as a rivet. The stabilization effect (also called the anchoring effect) of the rivet is beneficial for suppressing metal NP coalescence and sintering/detaching from the carbon support. In order to utilize such a rivet for improvement of catalytic stability, Wang's group demonstrated the successful preparation of carbon-riveted Pt/C,[32] microcapsule Pt/MWCNTs–TiO_2,[170] Pt/TiO_2–C,[171] and Pt/MWCNTs–Al_2O_3[172] on the basis of *in situ* carbonization of glucose – the carbon precursor – at 400 °C under an inert atmosphere. Unlike the overcoating engineering on metal NPs discussed in the above sections, the carbon rivet could not evidently affect (or decrease) the electrochemical surface area of the resulting metal catalysts.

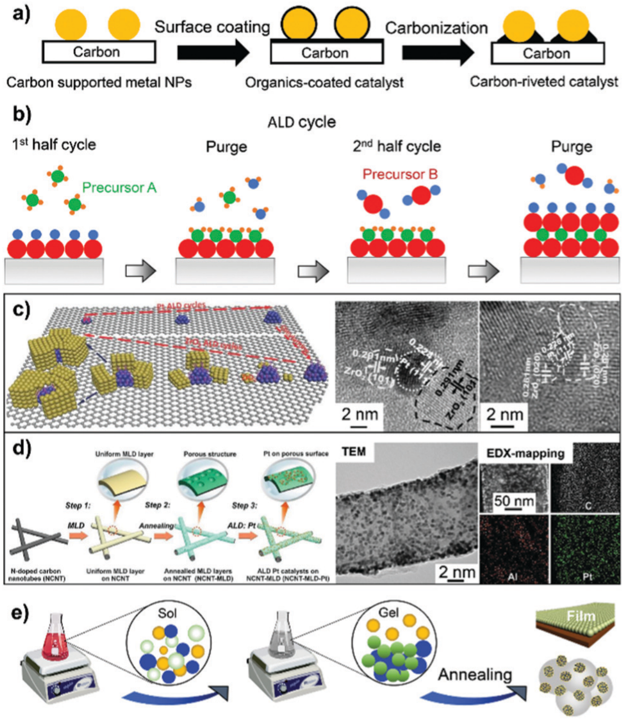

Fig. 7 (a) Schematic illustration of carbon rivet formation on a carbon-supported metal catalyst using organic coatings as the carbon precursor. (b) Schematic of the process of ALD cycles. (c) Overcoating ZrO_2 onto the N-doped carbon nanotube by ALD cycle number control. Reproduced from ref. 191 with permission from Wiley-VCH, Copyright 2015. (d) MLD of AlO_x species onto the carbon nanotube to support the well-dispersed Pt NPs. Reproduced from ref. 193 with permission from Elsevier, Copyright 2019. (e) Schematic of the sol–gel process for the preparation of carbon–metal oxide composites.

In addition, graphitic carbon nitride (g-C_3N_4) materials feature the advantages of high mechanical stability in an acidic/oxidative environment, and possess abundant Lewis acid and base sites (*i.e.* –NH groups and N atoms on the triazine/heptazine ring) for high dispersion of metals by forming strong electronic interactions. Introducing g-C_3N_4 materials onto the surface of carbon has been demonstrated to stabilize carbon-supported PtRu NPs for enhanced MOR electrocatalysis.[173–175] Direct one-pot pyrolysis of the mixture of carbon-supported metal material and melamine is an effective method for g-C_3N_4 overcoating.[173] On the other hand, the carbon nitride nanosheet-coated carbon, named C@g-C_3N_4, was reported to be fabricated through thermal polymerization of the mixture of urea and carbon support, followed by an exfoliation process at decomposition temperature (600 °C) under an inert atmosphere.[174,175]

2.4.3 Modification of the carbon support by overcoating with inorganic metal oxides. In thermal catalysis, metal oxides, when used as support materials, could promote catalytic reactivity and structural stability towards sintering by regulating the metal nanoparticle surface and forming strong metal–support interactions (SMSIs). Equally, metal oxides such as TiO_2,[176] WO_3,[177] $Ti_{0.7}Mo_{0.3}O_2$,[178,179] $Ta_{0.3}Ti_{0.7}O_2$[180] and Sn-doped indium oxide[181] have been constantly exploited as support materials to improve the catalytic efficiencies of PGM-based electrocatalysts. However, the lack of sufficient surface area for the high dispersion of metal NPs restricts their wide applications. To circumvent it, carbon–metal oxide composites (that is, metal oxide-decorated carbon materials) have been vigorously investigated by combining the merits of carbon support and metal oxides. The synthetic methods for the preparation of carbon–metal oxide composites mainly include, but are not limited to, chemical vapor phase deposition technology and wet chemical synthesis method.

Chemical vapor phase deposition. Among the boomingly deployed chemical vapor phase deposition technologies, atomic layer deposition (ALD) and molecular layer deposition (MLD) are, in particular, gaining in popularity for the rational design and fabrication of advanced nanomaterials from an atomic level. The readers are referred to the excellent reviews that highlight the status and prospects of ALD and MLD technologies for sustainable energy-related applications.[182–187]

The ALD process generally proceeds as sequential, self-limiting surface reactions by exposing the substrate to separate precursors (such as trimethylaluminum (TMA) and water vapor used in the best known Al_2O_3 ALD process) in near-vacuum conditions. Each deposition cycle tends to form an atomically thick layer on the surface of the substrate (Fig. 7b). ALD can be used to deposit many kinds of coatings such as metal oxides, nitrides, and sulfides, and allows control over the uniformity of surface coatings with high accuracy. ALD overcoating of metal oxide layers with the thickness controlled by deposition cycle numbers could endow the as-fabricated catalysts with distinct catalytic reactivities.[188–190] Researchers have specifically developed the area-selective ALD technology in an attempt to precisely control overcoating sites and expose more preferred surface.[187] An organic mask molecule, *i.e.* oleylamine, is used to prevent the deposition of metal oxide coatings on the surface of metal nanoparticles. Oleylamine molecules can be removed by a high-temperature annealing treatment afterwards. As such, typical examples of area-selective ALD coating of ZrO_2 nanocages onto Pt-supported N-doped carbon nanotubes (NCNTs)[191] and TaO_x ALD overcoating onto Pt-supported carbon black[192] have been reported by Sun's group. As illustrated in Fig. 7c, upon increasing ZrO_2 ALD cycles from 20, 30 to 50, an open or holy nanocage is formed around the Pt nanoparticle without deposition on its surface. Thermal stability evaluation by heating the as-synthesized catalysts to 600 °C indicated that the particle size of Pt on ALD30ZrO_2–Pt/NCNT (with 30 ALD cycles) increased from 2.3 to 2.7 nm, while that of ALD50ZrO_2–Pt/NCNT600 °C (with 50 ALD cycles) showed a nearly constant particle size distribution. ALD50ZrO_2–Pt/NCNT600 °C also displayed 9 and 10 times higher electrochemical stability relative to the ALDPt/NCNT without ZrO_2 overcoating and the reference Pt/C catalyst, respectively, after 4000 potential cycles between 0.6 and 1.2 V_{RHE}.[191] Therefore, the encapsulation of Pt NPs within ALD overcoating-derived ZrO_2 nanocages could allow the catalytic efficacy of supported metal-based electrocatalysts to be maximized.

MLD is an extended technology after ALD for the preparation of polymer-based organic materials and inorganic–organic hybrid materials.[183] Metal-based metalcones and organic ethylene glycol (EG) are the most commonly used precursors for inorganic–organic thin-film coatings. The removal of organic linkers such as EG by thermal or chemical treatment is necessary for the generation of porous metal oxide overlayers. For developing a stable Pt ORR electrocatalyst, Zhang *et al.*[193] for the first time applied MLD technology to stabilize Pt NPs. MLD alumina oxide (AlO_x) overlayers on N-doped carbon nanotubes were fabricated by alternatively introducing trimethylaluminium and glycerol precursors into a Gemstar-8 ALD system. MLD AlO_x overlayers feature a porous structure with enriched pores after thermal treatment at 400 °C in air (Fig. 7d). As verified by TEM and EDX-mapping images, the enriched pores on AlO_x-overcoated carbon nanotubes serve as the anchor sites for interacting with Pt NPs, which accounts for the observed high dispersion of the metal. Consequently, the MLD strategy imparts the Pt-based catalyst with markedly improved ORR performance, overpassing the catalyst in which the Pt NPs are not coated with the MLD-derived metal oxide overlayer.

Wet chemical synthesis. For wet chemical synthesis, the introduction of metal oxides onto the carbon support could be divided into two approaches, including the hydrothermal-induced deposition–precipitation process and the chemical sol–gel process *via* electrostatic interactions. Limitedly, a CeO_2-decorated carbon support was reported to be obtained through the direct carbonization of Ce-MOFs.[194] The deposition of metal particles on carbon–metal oxide composites, as a step involved in metal based catalyst preparation, can be performed by (i) one-pot co-precipitation with a metal hydroxide onto the carbon support followed by annealing treatment; or (ii) post-immobilization *via* the conventional polyol reduction method; or (iii) direct ''solid'' method involving impregnation, heating and gas reduction steps. Selecting a reliable method requires care to meet the requirements of metal particle size and size-distribution as well as metal chemical states for specific applications in catalysis.

In the deposition–precipitation process, a base such as NaOH and urea facilitates the first conversion of metal salt precursors into metal hydroxides and then their simultaneous deposition on the surface of the carbon support.[195,196] Thermal decomposition of as-precipitated metal hydroxides on the surface of carbon helps in the formation of homogeneous and crystalline metal oxide-overcoated carbon composites. On the other hand, in the sol–gel chemical process, metal alkoxide compounds ($M(OR)_n$), including ethyloxide, isopropoxide, and butoxide compounds, are initially hydrolyzed into $M(OH)_m(OR)_{n-m}$ species in the presence of water or in an acid solution under moderate hydrothermal conditions.[197–199] Concomitantly, the as-formed $M(OH)_m(OR)_{n-m}$ species undergo a complex polycondensation to form a well-dispersed metal oxide network on the surface of carbon after annealing treatment (Fig. 7e). Based on this strategy, Akalework *et al.*[200] overcoated multiwall carbon nanotubes (MWCNTs) with an ultra-thin TiO_2 film. The ultra-thin TiO_2 was a valuable coating for improvement in the dispersion of Pt with smaller particle size (1.6 nm) and a higher ECSA value (285.5 $m^2\ g^{-1}$), giving rise to a much higher electrocatalytic efficiency than that found with the uncoated Pt-MWCNT and commercial Pt/C catalyst. Similarly, TiO_2-coated carbon nanotubes (TiO_2/CNTs) were one-pot synthesized through the non-boiling isothermal hydrolysis process.[201] SnO_2–C composites with different SnO_2 loading were prepared *via* the sol–gel process.[202] Besides metal alkoxide compounds, metal chlorides such as $NbCl_5$,[203] $SnCl_2$,[204] and $TaCl_5$,[205] metal acetylacetonate (*i.e.* $Zr(acac)_4$),[206] and metal acetate (*i.e.* manganese acetate)[207] are also employed to prepare carbon–metal oxide nanocomposites, mostly by the process of thermal hydrolysis-deposition in anhydrous alcohol or an alcohol/water system.

Other synthesis methods. There are other attempts such as the direct air-annealing,[208] self-assembly-decomposition,[209] and a physical pulse-laser ablation in liquids (PLAL) method[210] for preparing carbon–metal oxide composites. In particular, highly dispersed MoO_x species were introduced onto carbon nanotubes (CNTs) through the decomposition of phosphomolybdic acid (HPMo, Keggin-type), which were self-assembled on the surface of functionalized CNTs.[209] Besides, TiO_x or SnO_x derived from the PLAL method were found to have abundant oxygen defects, which could reduce GO into rGo and the Pt precursor ($PtCl_4^{2-}$) to Pt(0) NPs. This *in situ* reduction process was crucial for the uniform distribution of small Pt NPs and the formation of strong interactions between Pt and the metal oxide, leading to enhanced mass activity, stability and excellent CO-antipoisoning ability towards the MOR catalysis.[210]

2.5 Modification of the metal oxide support by surface overcoating

Overcoating with carbon nanoshells has been widely exploited to modify the surface of the metal oxide support with examples pertaining to CeO_2,[211,212] Mn_3O_4,[213] and TiO_2.[214–217] Similar to the approach described for metal nanoparticles and the carbon support, direct pyrolysis of the composites containing organic compounds or polymers (such as ionic liquid,[212] Ppy,[214] xylose,[215] furfuryl alcohol[216]) is adapted for overcoating of the metal oxide support with carbon nanoshells. For example, through direct carbonization of β-cyclodextrin on the mesoporous CeO_2 support (MP-CeO_2) at 400 °C, Chu *et al.*[211] prepared carbon-CeO_2 composites comprising CeO_2 that were partly coated with carbon layers. Pt NPs were then deposited on the peripheral interface between MP–CeO_2 and carbon layer by means of the microwave-assisted polyol reduction method. Carbon overcoating on the MP–CeO_2 support could produce a large number of oxygen-containing species, *i.e.* –COOR group, which serve as anchoring sites for Pt deposition. An optimized 10.4 wt% loading of carbon species was effective for an acceptable catalytic performance of Pt/C_{40}–CeO_2. Upon further increasing the carbon content to 15.9 wt%, the contact between Pt NPs and CeO_2 support was obstructed, resulting in poor electrocatalytic property. As another example, the synthetic process for overcoating the carbon layer onto the Mn_3O_4 support to fabricate the Pt/Mn_3O_4–carbon triple-junction structure is illustrated in Fig. 8a.[213] Starting from Mn_3O_4 as the catalyst support, dopamine undergoes sequential oxidative polymerization and high-temperature carbonization to result in the formation of MnO@C. With the increase in the concentration of dopamine in the synthetic solution, the carbon nanoshell thickness also shows an increasing trend after carbonization (Fig. 8b–e). Subsequently, the deposition of Pt NPs was proceeded *via* a galvanic replacement process, whereby Pt precursors were allowed to diffuse through the carbon nanoshell to chelate and grow onto the surface of inner MnO, while MnO could be concurrently oxidized into Mn_3O_4. The final structure of the catalyst relied on the thickness of the carbon shell, since a thicker (*i.e.* 7.1 nm) carbon layer was observed to delay the inward diffusion of $PtCl_4^{2-}$ which induced the deposition of Pt on the outer surface of carbon. These works clearly imply that it is important to control the amount or the shell thickness of carbon on the metal oxide support to benefit the electrocatalytic performance of metal based catalysts.

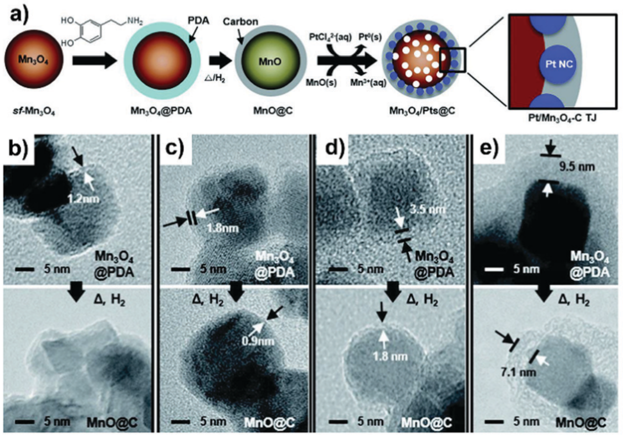

Fig. 8 (a) Schematic illustration of the preparation process of the Pt/Mn_3O_4–carbon triple-junction structure using Mn_3O_4, dopamine, and $PtCl_4^{2-}$ as the support, the precursor for the carbon overlayer and the precursor of Pt NPs, respectively. (b–e) TEM images of the overcoated metal oxide support having different outer layer thickness before and after high temperature pyrolysis. Reproduced from ref. 213 with permission from Royal Society of Chemistry, Copyright 2017.

2.6 Comparison of different surface overcoating strategies for the design of high-performance electrocatalysts

A comparison of a diversity of surface overcoating methodologies utilizing organic capping agents/polymers, inorganic carbon nanoshells and metal oxides is presented in Table 1, and the pros and cons of each process are also overviewed. High-performance electrocatalysts can be rationally designed *via* surface overcoating engineering by a suitable selection of overcoating materials and synthetic methodologies. The advantages of using organic capping agents and polymers as the surface coatings include (i) a large number of organic matters featuring specific electron-withdrawing/donating properties can be selected to manipulate the electron density of the metal surface by constructing unique metal–organic interfacial nanostructures and (ii) the corresponding catalytic benefits vary with the organic matters functionalized on the surface of metals when they are applied for a range of electrochemical reactions. However, it is precisely these advantages that might cause a lot of work for screening optimal organic species in the design and optimization of high-performance electrocatalysts in the laboratory. The stability of organic molecules coordinated with the metal needs to be paid attention when the surface-functionalized catalyst is applied under harsh operating conditions. Carbon nanoshells, as the stable coating material, are generally fabricated on the catalyst surface through pyrolysis and/or deposition of organic precursors at high temperatures. Synthetic conditions in terms of temperature, gas environment and coating amount need to be elaborately optimized since the engineered catalyst structural properties would significantly impact the electron/mass transfer process and further the catalytic efficiencies during catalysis. The introduction of the carbon nanoshell may influence metal particle properties such as the size, morphology and surface composition, in addition to the high-energy input in this strategy. On the basis of the existing literature, wet chemical synthesis and atomic layer deposition are the most used processes for the surface overcoating of metal catalysts with metal oxides. In particular, the ALD technology is able to allow control over the deposition location (that is the selective area atomic layer deposition) and the overlayer thickness from an atomic scale, although this technology along with MLD is not economically viable. In comparison with ALD/MLD, wet chemical synthesis tends to be more affordable for large scale modification of metal catalysts. It is important to perform wet chemical synthesis under the conditions that are suitable for the transformation of metal precursors (*i.e.* by hydrolysis, polycondensation), the further formation of an inorganic network and the final deposition onto the catalyst substrate in the solid–liquid phase. Metal oxide layers as-fabricated on the surface of catalysts are usually not uniform when using such a complex process, thus leading to limitations in terms of reliability. Nevertheless, note that the integration of surface coatings with metal NPs and/or support materials into a unique nanostructure could effectively endow the designed nanocatalysts with synergistic contributions for clean energy-based electrocatalysis especially in PEFCs and WECs.

3. Overcoated electrocatalysts for polymer electrolyte fuel cells

Proton-exchange membrane fuel cells (PEMFCs) and anion-exchange membrane fuel cells (AEMFCs) are among the most explored fuel cell technologies. PGM-based nanomaterials are the active electrocatalysts so far for energy-related small molecule activation reactions such as the ORR, HOR and MOR in PEFCs. Metal NPs supported on fuel cell electrocatalysts easily suffer from the issues of coalescence, Ostwald ripening and dissolution, attributed to their weak interactions with the support and the highly acidic operating conditions.[15,16] Due to the high potential (1.5–2.0 V) of the cathode under shut-down/start-up conditions a severe carbon corrosion could be induced, which, in turn, leads to the decrease of metal–support interactions accompanied by metal NP agglomeration and detachment from the support.[15] Moreover, the serious site-blockage and poisoning effects by spectator species, *i.e.* PO_4^{3-}, SO_4^{2-}, CO, and methanol (the crossover species in direct methanol fuel cells (DMFCs)), still remain as problems that hinder the improvement of catalytic efficiencies for low-temperature fuel cells.[37] Owing to the above performance degradation mechanisms, in most cases the electrocatalysts cannot meet the fuel cell

Table 1 Comparison of different overcoating strategies for the design of optimal electrocatalysts

Coatings	Processes	Pros	Cons
Organic capping agent/polymer	*In situ* capping through colloidal synthesis	One-pot method for organic-capped metal nanostructures; abundantly available organic capping agents	Wastage of most of the as-added organic molecules; several synthetic parameters affect particle properties
	Post-synthetic construction through *e.g.* the dipping method	Simple and easy method	Specific solvent for dissolving the organic modifier
	Oxidative polymerization in liquid phase	Uniform thin film; relatively high loading	Control of film thickness; special oxidant added; impurities generated
Inorganic carbon nanoshell	High-temperature pyrolysis of polymers or metal–organic composites including MOFs	Simple; abundantly available carbon precursors; potential scale-up	Induction of metal particle structural evolution under heating conditions; high energy required; control of carbon shell homogeneity and graphitization degree
	Chemical vapor phase deposition	Thin-layer carbon shell; high uniformity	High energy required; toxic and explosive gases as carbon precursors
Inorganic metal oxide layer	Wet chemical synthesis	Simple and efficient; commercially viable	Limitation of controlling the layer thickness, morphology and uniformity
	Atomic layer deposition/molecular layer deposition	Atomic control over layer thickness; ultra-thin coating film; high uniformity	Low coating rate; economic viability
	Electrodeposition	Easy control by applying a slight voltage; cost-effective	Pre-coating the catalyst onto the electrode; specific devices equipped with electrode and electrolyte

performance targets. Several limitations, in essence, pose considerable challenges to optimal electrocatalyst design: (i) the trade-off between electrocatalytic activity and long-term durability; (ii) the sacrificing of power performance and durability when decreasing the loading of PGMs (in order to reduce cost).[12,16] As summarized in the above section, vast research has been focused on the surface overcoating strategy for the fabrication of metal NPs and the modification of support materials. Herein, recent advances of both precious and non-precious metal-based electrocatalysts fabricated by surface overcoating engineering for efficient application in H_2–O_2 fuel cells (PEMFCs and AEMFCs involving the ORR and HOR) and direct alcohol fuel cells (anodic reactions such as MOR and EOR) are presented in Sections 3.1–3.3. A comparison of the surface coatings suitable for above-mentioned catalytic processes is summarized in Section 3.4. The benefits of utilizing overcoating-derived support materials, *i.e.* porous carbon and metal oxides, for metal-supported electrocatalyst design and optimization will be discussed in Section 3.5.

3.1 Overcoated electrocatalysts for the ORR

The ORR catalysis on the cathode is at the heart of fuel cells since its sluggish kinetics require a higher loading of Pt, thereby becoming the active area of research. The cathodic ORR is a multielectron process involving the reacting active intermediates such as *OOH, *O and *OH. The ORR in acid and alkaline solution can proceed by the following pathway: $O_2 + 4H^+ + 4e^- \rightarrow 2H_2O$ (acidic condition) and $O_2 + 2H_2O + 4e^- \rightarrow 4OH^-$ (alkaline condition). Depending on the nature of the electrocatalyst, a partial reduction, the two-electron pathway: $O_2 + 2H^+ + 2e^- \rightarrow H_2O_2$ (acidic condition) and $O_2 + H_2O + 2e^- \rightarrow HO_2^- + OH^-$ (alkaline condition), can take place on the cathode to form H_2O_2. ORR is oftentimes regarded as a prototype for developing advanced concepts that can be applied to other catalytic systems.[218] In this section, the categories related to both precious and non-precious metal based ORR electrocatalysts are described.

3.1.1 Overcoated precious metal based ORR electrocatalysts

Organic material-overcoated precious metal based ORR electrocatalysts. Engineering metal based electrocatalysts with high resistance towards the site-blocking by spectator species from the electrolyte is desirable for catalytic improvements in performance for the cathodic ORR in PEFCs.[31,42,47] Surface-patterned organic molecules such as cyanide (CN^-) groups and amine could hinder the adsorption of non-covalent bulky adsorbates (SO_4^{2-} and PO_4^{3-} ions) on the metal, leading to favoured ORR activity in acid solution.[44,59] The limitation on the CN^--patterned Pt surface is that the noncovalent interactions formed between the anionic CN^- adlayer and the positively hydrated $K^+(H_2O)_x$ cluster would block O_2 adsorption and result in activity deactivation in a basic KOH electrolyte.[59] Electrostatic interactions were recently utilized by Jung *et al.*,[219] who fabricated self-assembled monolayers of L-cysteine on Pt for efficient ORR catalysis. On the one hand, the –COOH groups of L-cysteine become negatively charged (–COO^-) in KOH solution, and can repulse excess OH^- and attract the hydrated $K^+(H_2O)_x$ cluster to avoid the blocking of Pt active sites (Fig. 9a). On the other hand, when immersing in acidic H_3PO_4, the –NH_2 groups of L-cysteine are protonated to form positively charged –NH_3^+ species, which could capture the PO_4^{3-} ions by forming strong hydrogen bond and electrostatic interactions, and thus inhibiting their interactions with Pt. In these ways, the hindering by various spectator ions is remitted, as indicated by the decreased adsorption charge densities on Pt (Fig. 9b). As a result, the ORR specific activity on L-cysteine-patterned Pt is much higher than that found with the unmodified Pt catalyst in both KOH and H_3PO_4 solutions (Fig. 9c).

In DMFCs, the issue associated with methanol crossover from the anode to cathode of the cell remains as a barrier to the development of ORR electrocatalysts. Improving the methanol-tolerance of the cathodic Pt-based electrocatalyst is thus of vital importance for achieving electrical selectivity and high efficiency of ORR. Polymer layers and organic matters such as PAH,[51,54,56] PVPA/PyPBI[75] and ionic liquid ([MTBD][bmsi])[220] have been fabricated onto Pt-based catalysts by using *in situ* or post-synthesis approaches to improve their anti-poisoning ability towards methanol. The improved methanol-tolerance can be attributed to the steric hindrance effect from the surface coatings. Lu *et al.*[221] reported that a higher pyridine coverage ($\theta_{S,H} > 50\%$) on the surface of the Pt/C ORR electrocatalyst was necessary for hindering the adsorption of methanol. As a result, ORR specific activity linearly increased with $\theta_{S,H}$ and a 6 times enhancement was achieved when the Pt surface was saturated with pyridine ($\theta_{S,H} = 80\%$). In addition to the steric hindrance effect, surface-overcoated organic molecules have profound effects on the electronic surface structure of metal entities.[51,52,56] As indicated from CO stripping measurement, the coordination of pyridine molecules made the Pt surface electron-rich, which could facilitate the adsorption of O_2 and weaken the adsorption of the *O intermediate.[221] ORR mass activity was found to be determined by the competition between the steric and electronic effects from pyridine. Accordingly, the electronic effect dominated the ORR process when $\theta_{S,H} < 50\%$. The authors also demonstrated the existence of both steric and electronic effects from 4-dimethylaminopyridine and triphenylphosphine ligands functionalized on the Pt surface. Other ligands such as oleylamine (OA) and butylamine exhibited a negligible electronic effect on the ORR in acidic solution. Chung *et al.*[222] observed from synchrotron-based spectroscopy that the d-band center of Pt downshifted after surface-construction with OA (Fig. 9d), a fact ascribed to the increase of electron density in the frontier d states of Pt. The smaller d-band vacancy contributed to the decreased adsorption strength of bulky PO_4^{3-} ions on the Pt surface, resulting in enhanced ORR kinetics. In this study, the frontier d-band structure of metals represents the suitable descriptor of the ORR activity.

The strong adsorption of OH_{ad} on the metal surface causes the sluggish ORR kinetics.[64,223] Metal intrinsic structural properties with respect to their electronic structures strongly determine the adsorption of OH_{ad}. Electron delocalization on Pt is thus reasonable for changing metal affinity with O_{ad} and OH_{ad} species and

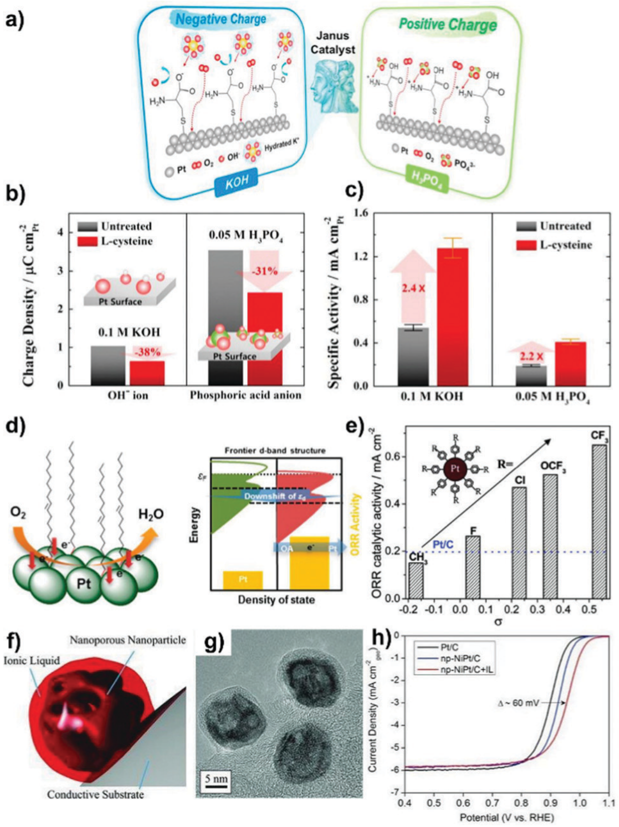

Fig. 9 (a) Schematics of the electrostatic interaction between charged L-cysteine molecules on the Pt surface and spectator ions in KOH and H_3PO_4 solutions. (b) Anion adsorption charge densities obtained from CVs and (c) ORR specific activities (at 0.9 V_{RHE}) on untreated and L-cysteine-decorated Pt polycrystalline structure. Reproduced from ref. 219 with permission from Elsevier, Copyright 2015. (d) Schematic of the Pt d-band structure change after surface-capping of OA molecules. Reproduced from ref. 222 with permission from American Chemical Society, Copyright 2013. (e) Variation of the ORR specific activity (at 0.9 V_{RHE}) with Hammet substituent constant (σ). Reproduced from ref. 224 with permission from American Chemical Society, Copyright 2012. (f) Cartoon illustrating the encapsulation of nanoporous NiPt NPs by an IL. (g) HRTEM image of NiPt NPs encapsulated within the [MTBD] [beti] IL, supported on carbon. (h) ORR curves for Pt/C, np-NiPt/C, and np-NiPt/C + IL in O_2-saturated 0.1 M $HClO_4$ at 60 °C with 20 mV s^{-1} and 1600 rpm. Reproduced from ref. 226 with permission from Wiley-VCH, Copyright 2013.

enabling the regulations on ORR catalytic activity. Zhou *et al.*[224] manipulated the electronic surface structure of Pt using a variety of phenyl-based organic molecules with different electron-withdrawing *para*-groups (such as CH_3, F, Cl, OCF_3, CF_3). As shown in Fig. 9e, the ORR activity increases in line with the increased electronegativity of *para*-groups, according to their Hammet substituent constants (σ). The transfer of electrons from Pt to the surface organic molecules could decrease the electron density of Pt and weaken the adsorption of oxygen-containing species (OH_{ad}, O_{ad}), which eventually lead to a positive effect on ORR catalysis. In addition, the organic agent-functionalized Pt catalysts show a higher stability than "naked" Pt/C under similar conditions.

The OH_{ad}–water network is a stable form of OH_{ad} after its incorporation into water hexagonal networks. In addition, the interface water, known as the source of oxygenated species, is regarded as the site-blocker for ORR electrocatalysts. Typically, surface engineering of Pt with a hydrophobic ionic liquid layer has been considered as the effective strategy to efficiently destabilize OH_{ad} species and repel water from the surface intermediates and products while maintaining the accessibility of active sites to the reactants, resulting in high resistance of the catalyst to surface oxidation and thus accelerated ORR activities.[63,225–227] In the work reported by Snyder *et al.*,[226] markedly improved ORR kinetics in performance was observed on nanoporous NiPt nanoparticles encapsulated by a hydrophobic, protic ionic liquid (IL, [MTBD][beti]) (Fig. 9f and g). This IL coating is not only able to provide a nonaqueous environment to prevent the oxidation of Pt, but also brings in the benefit of high solubility of O_2 near the metal particle surface. As shown in Fig. 9h, a nearly 60 mV reduction of overpotential for ORR is a clear reflection of the decrease of the surface coverage of OH_{ad}. Such an IL-coated catalyst exhibits an order of magnitude larger half-cell specific activity than the commercial Pt/C catalyst.

Based on the existing literature, it should be stressed that there is an inevitable loss of the active surface area following the organic surface modification.[47,49] It is therefore necessary to optimize the amount or the coverage of the organic material on the surface of the metal to maintain the adsorption and desorption of reactants and products with the aim of realizing an acceptable electrocatalytic performance. Meanwhile, the findings from a small number of studies especially on ionic liquid layer coatings of Pt-based catalysts suggest comparable ECSA values to the unmodified counterparts.[227,228] In most cases, the coordination stability of organic–metal nanostructures has been ensured at least in the potential range where the electrochemical reactions take place.[221] On the other hand, the ionic liquid layer for example was found to accelerate the dissolution of Mo from PtNiMo NPs because of its strong complexing capability, leading to worse durability performance.[228] Therefore, comprehensive interface theory and understanding the dynamic properties of the interfacial metal–organic structure during the electrochemical processes are highly desired in further research works.[62]

Inorganic carbon nanoshell-encapsulated precious metal based ORR electrocatalysts. Fabricating metal-based catalysts with inorganic carbon nanoshells can spatially confine metal active sites by providing barriers toward their aggregation and sintering during the process of catalyst preparation and electrocatalytic reactions.[80–86,89–92,229,230] Nie *et al.*[230] reported the synthesis of Pt/C@NGC by overcoating nitrogen-doped graphitic carbon (NGC) shells onto the Pt/C catalyst. Polymeric PANI overlayers efficiently stabilize 4.7 nm Pt NPs in the 900 °C carbonization process, where NGC shells with 3 nm of thickness are consequently formed (Fig. 10a and b). Although there is a 40% decrease of ECSA after overcoating with NGC, the ORR specific activity at 0.9 V_{RHE} on Pt/C@NGC is 2.5 times larger than that found with Pt/C (Fig. 10c). Accelerated stress tests by performing cyclic potential sweeps between 0 and 1.2 V_{RHE} show only 16 mV degradation in half-wave potential on

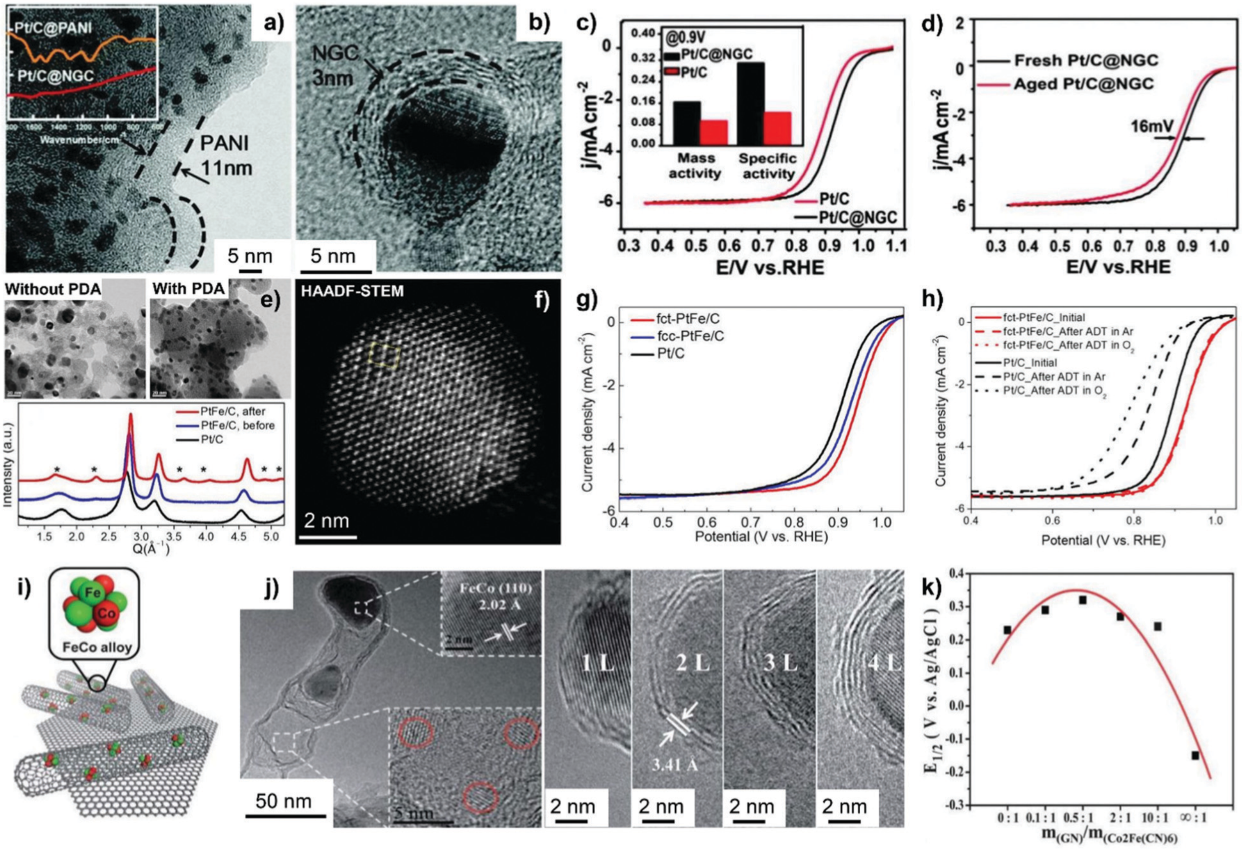

Fig. 10 HRTEM images of (a) Pt/C@PANI and (b) Pt/C@NGC. (c) Polarization curves of Pt/C and Pt/C@NGC in an O_2-saturated 0.1 M $HClO_4$ solution at 60 °C at 10 mV s^{-1} and 1600 rpm. The inset in (c) represents the mass activities and specific activities at 0.9 V_{RHE} for Pt/C and Pt/C@NGC. (d) Polarization curves of Pt/C@NGC before and after 1500 cycles under a condition similar to that in (c). Reproduced from ref. 230 with permission from Royal Society of Chemistry, Copyright 2014. (e) TEM images (upper) of PtFe NPs after annealing at 700 °C with and without surface coating of PDA; high-resolution powder diffraction patterns (bottom) of PtFe/C before and after annealing in comparison with Pt/C. (f) HAADF-STEM image of annealed fct-PtFe NPs. (g) ORR polarization curves of Pt/C, fcc-PtFe/C, and fct-PtFe/C at the rotating disc electrode (RDE). (h) Polarization curves of fct-PtFe/C and Pt/C before and after 10 000 ADT cycles. Reproduced from ref. 89 with permission from American Chemical Society, Copyright 2015. (i) Illustration of Pod(N)-FeCo/GNs with the FeCo (110) crystal plane and smaller NPs confined within pod-like CNTs. (j) HRTEM images show the cross-sections of FeCo NPs covered by 1–4 layers of graphitic carbon wall. (k) Half-wave potential ($E_{1/2}$) of RDE polarization curves as a function of m(GN)/m($Co_2Fe(CN)_6$). Reproduced from ref. 242 with permission from Royal Society of Chemistry, Copyright 2013.

Pt/C@NGC (Fig. 10d), even lower than that (62 mV) of Pt/C. In addition to stabilizing Pt NPs, the carbon nanoshells doped with heteroatoms, *i.e.* S,[82] are catalytically active for lowering the surface coverage of OOH* (the species generated through $O_2 + H^+ + e^- + * \rightarrow OOH^*$, where * indicates an active site on the electrocatalyst surface) *via* fast O–O dissociation and, thereby boosting the ORR activity. On the other hand, as reported by Yamada *et al.*,[85] the PDA-derived carbon overlayer was capable of mitigating the adsorption of the Nafion ionomer (a widely used polyelectrolyte in PEFCs) on Pt sites and facilitate O_2 transport near the Pt/ionomer interface to improve ORR mass activity.

In order to form ordered face-centered tetragonal (fct)-structured PtFe NPs with small particle size, Chung *et al.*[89] overcoated a N-doped carbon nanoshell onto as-synthesized carbon-supported disordered PtFe NPs by *in situ* carbonization of the PDA overlayer. High-resolution powder diffraction and high-angle annular dark-field scanning transmission electron microscopy (HAADF-STEM) characterization verified the formation of 6.5 nm fct-PtFe NPs that are supported on the carbon (Fig. 10e and f). The PDA-derived carbon shell with less than 1 nm thickness could efficiently avoid PtFe NP coalescence. The fct-PtFe NPs showed a weak affinity to oxygen-containing species and thereby a higher ORR activity than fcc-PtFe and monometallic Pt/C (Fig. 10g). Extremely high durability was observed on the ordered fct-PtFe catalyst (Fig. 10h), which is because of the higher resistance of Fe atoms towards oxidation and dissolution after electronic coupling with Pt. The strong binding of N dopants with Pt atoms was also speculated to be responsible for stability improvement. In addition, structurally ordered intermetallic PtFe alloy NPs were formed *via* a thermally driven interfacial diffusion alloying route in the presence of the as-fabricated inner PDA layer and outer silica shell.[92] In this case, ordered PtFe NPs exhibited a 600% increase in mass activity and specific activity to the ORR in comparison with Pt/C. A higher stability was additionally observed on the

PtFe alloy due to the ordered atomic arrangement and robustness of the N-doped carbon nanoshell. Moreover, a PDA-derived N-doped graphitic carbon layer (NGC, 0.76 nm thickness) was overcoated on the carbon-supported $PtNi_3$ alloy catalyst to overcome the stability issue under acidic conditions, as reported by Sun *et al.*[231] In the preparation process, overcoating as-synthesized $PtNi_3/C$ with the PDA layer was first performed, followed by high-temperature pyrolysis to obtain the final catalyst, which was named $PtNi_3/C@NGC$. Structural characterization indicated that the $PtNi_3$ particle holds the merit of a Pt-rich surface and a Ni-rich core, likely attributed to the higher adsorption energy of Pt with N atoms (from PDA coating) than that of Ni. As a result, the utilization efficiency of Pt on the $PtNi_3/C@NGC$ sample was improved, showing 1.16 A mg_{Pt}^{-1} of mass activity and 2.9 mA cm^{-2} of specific activity towards the ORR. During the accelerated durability test between 0.6 and 1.0 V_{RHE} for 10 000 cycles under an O_2 atmosphere, $PtNi_3/C@NGC$ displayed negligible loss of ECSA and half-wave potential, which were much superior than $PtNi_3/C$ and commercial JM-Pt/C catalysts.

MOF-derived nanostructures are also corroborated to bring in the benefits of enhancing the electrocatalytic performance of PGM-based catalysts.[232–234] Wu *et al.*[233] reported that a ZIF-67-derived ultra-thin 2D carbon layer could stabilize Pt NPs distributed on reduced graphene oxide. It is the synergy of Pt with $Co–N_x–C$ active sites (pyrolyzed from ZIF-67) that improved the ORR activity. Theoretical studies revealed that O*, OOH* and H_2O_2 were formed only on $Co–N_4–C$ sites. The generated H_2O_2 could spillover to Pt(111) sites to produce H_2O when Pt(111) was in the vicinity of $Co–N_4–C$ sites. In addition, a carbon layer-coated PtNi ORR electrocatalyst, named PtNi@C, was obtained from the pyrolysis of ZIF-like nanomaterials, which were synthesized by a one-pot solvothermal process from Ni^{2+}, Pt^{2+} and 2-MIM.[234] Several factors contributed to the high ORR efficiencies, including the optimized adsorption energy of oxygen-containing species after alloying Pt with Ni atoms, the modulated electronic structure of PtNi by the N-doped carbon nanoshell, and the physical barrier functionality of carbon coatings towards metal agglomeration and dissolution. Regardless of the type of organic materials used as the carbon precursor, the pyrolysis conditions should be precisely controlled as the thickness and graphitization degree of the carbon nanoshell determine the catalytic efficacy of metal@C materials.[84–86]

Inorganic metal oxide overlayer-fabricated precious metal based ORR electrocatalysts. Silica oxide is the most investigated coating material among the metal oxides employed for the design of high-performance fuel cell electrocatalysts. Takenaka *et al.*[140,141] have demonstrated that silica overlayer-coated Pt-based electrocatalysts exhibit enhanced ORR efficiencies. The selection of silica precursors usually has an effect on the features of the obtained silica overlayer with regard to porosity and hydrophilic/hydrophobic properties. Catalyzed by a base such as the ammonia water solution, the $C_2H_5O–Si$ bonds in TEOS could hydrolyze into Si–OH groups, which could further undergo Si–O–Si bond formation with a high polycondensation degree. Unlike $C_2H_5O–Si$ bonds, the $CH_3–Si$ bonds in the methyltriethoxysilane (MTEOS) precursor cannot hydrolyze into Si–OH groups. As a result, the silica overlayer ($CH_3–SiO_2$) derived from MTEOS shows larger pore size and hydrophobic surface property. The higher ORR activity of SiO_2/Pt/CNT(MTEOS) was mainly attributed to the promoted diffusion of oxygen and water in the larger pores the catalyst featured.[141] The micropore size of the TEOS-derived silica overlayer can be enlarged by using organic $NH_2(CH_2)_nNH_2$ as a template to benefit the diffusion of reactants and products on SiO_2/Pt/CNT during the ORR process.[235] The benefits from coating with silica layers are not limited to the well-known aspects in terms of preventing metal NPs from degradation and acting as the selective membrane for oxygen diffusion onto the active sites. As reported from the work of Park *et al.*,[236] the silica overlayer with hydrophilic Si–OH surface species could help in increasing the proton conductivity especially in low-humidity conditions. According to them, the overcoating of Pt/C with silica layers enabled the preparation of the anodic catalyst layer for PEFCs with a low ratio of ionomer to carbon. As such, SiO_2-coated Pt/C showcased a better electrocatalytic performance than the commercially uncoated Pt/C catalyst.

3.1.2 Overcoated non-precious metal-based ORR electrocatalysts. The cathodic ORR accounts for nearly 80% of the Pt loading in fuel cells because of its sluggish kinetics. The requirement to reduce the total cost of cell stacking has stimulated the development of a broad variety of cost-effective ORR non-precious metal-based catalysts (NPMCs), namely, metal–polymer components, non-PGM chalcogenides, metal oxide/carbide/nitride catalysts, and transition-metal-derived N-doped carbon materials ($M–N_x/C$, where M = Fe, Co, Ni, Mn, *etc.*).[31,237] Even though some NPMCs exhibit comparable ORR activity to that found with the commercial reference Pt/C catalyst in alkaline solution, the easier dissolution and performance degradation of 3d transition metals in an acid electrolyte call for innovative design and optimization of NPMCs. To our delight, the surface overcoating strategy has been employed as an effective means of developing high performance NPMCs by incorporating transition metal species into the polymer matrix or by confining them within the heteroatom-doped carbon nanoshell, which will be discussed in this section.

Metal–polymer composites and overcoated metallic catalysts. Polymers can incorporate transition metal sites into their matrix to work as non-precious electrocatalysts in fuel cells.[71] To mimic the atomic configuration in cobalt porphyrins, for instance, conductive polypyrrole (PPY) loaded on Vulcan XC 72 carbon was selected as the entrapping matrix to prepare the Co–PPY–C composite.[238] After entrapping into the PPY polymer, Co species were observed to strongly interact with the N atoms in pyrrole units by forming Co–N bonds. In this case, the as-formed CoN_x species were active for the achievement of a power density of *ca.* 0.14 W cm^{-2} in H_2–air fuel cells at 0.4 V. Likewise, the Co–PPY–C composite was extremely stable, without showing obvious activity drop after 100 h cell operations.

Transition-metal-derived N-doped carbon materials are normally produced from the pyrolysis of metal–heteroatom-containing composites or metal-coordinating complexes.[94,239–241] Dong *et al.*[240] obtained N,S-codoped carbon matrix-coated Co NPs through the *in situ* reduction of Co_9S_8 with melamine in the process of carbonization. S species could facilitate N element doping into the carbon matrix with a high richness of defects, which served as the additional active sites for the alkaline ORR catalysis. The realized high durability was assigned to the protective aid from carbon overlayers. Similarly, in order to inhibit the leaching of Fe into acid solution during the process of ORR, heteroatom-doped carbon-coated Fe catalysts with core–shell nanostructures have been developed. In the study of Park *et al.*,[241] Fe@NSC20-700_1-900_1 (NSC: N,S-codoped carbon shell) served as the best performing catalyst, by showing an enhanced half-wave potential (0.794 V) and comparable ORR activity (0.864 mA cm^{-2}) to Pt/C (0.811 V and 1.18 mA cm^{-2}@0.85 V). The half-wave potential negatively shifted by only 41 mV after the stability test with 10 000 potential cycles between 0.7 and 1.2 V_{RHE} in O_2-saturated 0.5 M H_2SO_4. Recently, Chen *et al.*[93] studied the impact of S-doping of carbon layers on the ORR catalysis catalyzed by Fe@S,N-DC, which was composed of Fe encapsulated within S,N-codoped defective carbon layers (S,N-DC). In comparison with the S-free counterpart, the S,N-DC surface was characterized by enriched electron density, which could reduce the barrier towards the electron transfer from Fe to the S,N-DC shell, thus boosting the ORR activity.

Overcoated metal alloy and metal oxide catalysts. As demonstrated by Wu *et al.*,[239] a PANI–FeCo–C catalyst was successfully fabricated through the pyrolysis of aniline, carbon black, cobalt(II) nitrate, iron(III) chloride and $(NH_4)_2S_2O_8$ oxidant under an inert atmosphere followed by acid leaching and second heating treatment. Upon pyrolysis at elevated temperatures, PANI got gradually converted into spherical carbon particles and resulted in a more graphitic structure when the temperature reached 900 °C. The resultant PANI–FeCo–C was the best-performing catalyst by exhibiting high activity and remarkable operative stability after 700 h at 0.4 V in H_2–air fuel cells. Higher temperature (950 °C, 1000 °C) led to a non-uniform morphology for the carbon particles with a high loss of surface area and, thus an inferior catalytic performance.

In order to study the influence of carbon wall thickness on the ORR, Deng *et al.*[242] pyrolyzed the mixture of graphene nanosheets (GNs) and $Co_2Fe(CN)_6$ to form highly dispersed FeCo alloy NPs, which were encapsulated by pod-like carbon nanotubes (Pod(N)) with fewer walls. GNs were effective in controlling the growth of carbon nanotubes. From the catalyst, named Pod(N)–FeCo/GNs, it was found that the thickness of the carbon wall distributes within 3–4 layers over the metal cores (Fig. 10i and j). ORR activity based on the half-wave potential ($E_{1/2}$) of RDE polarization curves displays a volcano-shaped relationship with the GNs/$Co_2Fe(CN)_6$ mass ratio. 0.5/1 is an optimized ratio to obtain a maximum power density (328 mW cm^{-2}) on Pod(N)–FeCo/GNs (Fig. 10k). More than 60% increase of power density was attained with respect to Pod(N)–FeCo (derived from direct-pyrolysis of $Co_2Fe(CN)_6$) in H_2–O_2 fuel cell tests. Theoretical studies indicated that the N dopants on the surface of Pod(N) could promote the adsorption of O_2. Such a promotion effect appeared to decrease with an increase in the thickness of the carbon wall. It reasonably explained the observation that the catalyst with a thinner carbon wall displayed much higher activity towards the ORR catalysis. In addition, ORR catalytic efficiencies can be enhanced in most cases by the synergy of the metal alloy with the heteroatom-doped carbon nanoshell.[95,125]

Metal oxide core–shell nanostructures such as CoO@Co-g-C_3N_4 were reported to exhibit high ORR activity, long-term durability and good methanol-tolerance ability.[94] The outer Co-doped g-C_3N_4 shell on the CoO@Co-g-C_3N_4 catalyst was assigned as the active site for ORR. In addition, Gao *et al.*[243] demonstrated the preparation of N-doped carbon-overcoated Fe_3O_4 through the pyrolysis of *in situ*-polymerized PANI-coated MIL-101-Fe MOF nanocomposites. The PANI overlayer served as a highly conductive skeleton and the source of nitrogen dopants in the catalyst obtained. The authors found that the PANI-derived N-doped carbon nanoshell was crucial for facilitating O_2 adsorption to enhance the ORR activity. They also investigated the effects of pyrolysis temperature and PANI coating amount on the ORR. From the optimal catalyst that was pyrolyzed at 900 °C with the initial mass ratio of aniline to MOFs at 1.5, a positive ORR onset potential was observed, close to that of the benchmark Pt/C catalyst in alkaline solution.

Overcoated other kinds of metal-based compounds. Carbon nanoshell-overcoated Fe_3C-based electrocatalysts have been developed by pyrolyzing organic compounds for the ORR.[120,244] In the catalyst overcoated with N-doped carbon shells, the coordination nests consisting of Fe_3C and N atoms are active for the alkaline ORR catalysis.[245] Additionally introducing heteroatoms such as boron (B) into the N-doped carbon matrix could enhance the ORR activity over the Fe–B, N–C active sites.[246] In addition, Karuppannan *et al.*[102] recently reported a nitrogen- and fluorine-enriched carbon-overcoated Fe/Fe_3C ORR electrocatalyst (NFC@Fe/Fe_3C). They examined the effect of pyrolysis temperature on the structural and electrocatalytic properties of NFC@Fe/Fe_3C. On increasing the temperature above 900 °C, there was a decreasing trend of the contents of nitrogen and fluorine in the carbon matrix, and the Fe_3C phase was converted into the FeC phase through carbon diffusion into face-centered cubic iron crystals. NFC@Fe/Fe_3C-9, a sample that was pyrolyzed at 900 °C, exhibited the best ORR performance with a half-wave potential of 0.87 V, which was 16 mV higher than that of commercial Pt/C in 0.1 M KOH. It also showed exemplary durability, where 26 mV degradation after 50 000 cycles (0.6–1.0 V_{RHE}) in alkaline solution and 27 mV decay after 30 000 cycles (0.6–1.0 V_{RHE}) in acid media were attained. The electrical interactions between the outer carbon shell and the inner metal core have been similarly observed on carbon-coated C@Co-P/C,[247] N-rich carbon shell-coated CoNP@NC/NG[248] and B,N-codoped graphitic carbon shell-encased Co_2P,[249] representing the efficient ORR electrocatalysts.

To sum up, surface overcoating-derived ORR electrocatalysts can be fabricated in a rational way, which requires a suitable choice of coatings including organic matters, inorganic carbon nanoshells and metal oxide layers. By integrating the benefits such as the modulated electronic structure of metal species, the sterically hindered process of metal coalescence/sintering and dissolution as well as the regulated adsorption behaviour of spectator species, the as-made precious metal based electrocatalysts could expectantly exhibit strengthened catalytic properties for the cathodic ORR in PEFCs. With the aid of the protection of transition metal NPs from contacting with the harsh electrolyte environment, along with the synergistic effects between heteroatom-doped carbon coatings and metal cores, remarkably reinforced electrocatalytic activity and durability can also be achieved on non-precious metal based electrocatalysts for the ORR catalysis.

3.2 Overcoated electrocatalysts for the HOR

As the anode reaction of a H_2–O_2 fuel cell, the HOR in acid and alkaline solution proceeds *via* the following: $H_2 \rightarrow 2H^+ + 2e^-$ (acidic condition) and $H_2 + 2OH^- \rightarrow 2H_2O + 2e^-$ (alkaline condition). In an acidic solution, the only intermediate on the metal surface is the adsorbed hydrogen (H_{ad}); thus, the hydrogen binding energy (HBE) is widely accepted as the activity descriptor parameter for the acidic HOR.[250] When switching the acidic operating environment to a basic one, the HOR shows markedly slow kinetics even when catalyzed by Pt-based catalysts. We note, in passing, that recently Ru-alloyed electrocatalysts such as PtRu,[251,252] RuIr,[253] and IrPdRu[254] have been innovatively developed as the most active materials for the alkaline HOR. Massive efforts have also been devoted for an in-depth understanding of the mechanism of the alkaline HOR with the aim of designing active and stable electrocatalysts.[255,256] HBE[257] and hydroxyl binding energy (OHBE, also known as oxophilicity)[251] are among the proposed theories for the alkaline HOR. In the elementary HOR process in an alkaline solution, the adsorbed molecular H_2 dissociates into surface adsorbed H_{ad} *via* a Tafel step ($H_2 + 2M^* \rightarrow 2M^*–H_{ad}$) or the Heyrovsky step ($H_2 + OH^- + M^* \rightarrow M^*–H_{ad} + H_2O + e^-$), followed by a Volmer step ($M^*–H_{ad} + OH^- \rightarrow M^* + H_2O + e^-$) from where H_2O and one electron are produced. The anodic HOR process mostly follows the Tafel–Volmer pathway and the Heyrovsky–Volmer pathway on catalytic active sites. Notably, as the attractive alternative to PEMFCs, AEMFCs open up the possibilities of applying earth-abundant and low-cost catalysts for the alkaline HOR, since non-PGM based electrocatalysts have been developed with Pt-like performance for alkaline ORR.

3.2.1 Overcoated precious metal based HOR electrocatalysts.

For H_2–O_2 fuel cells, tremendous progress in the development of cathodic ORR electrocatalysts has been made. On the other hand, much less attention is paid on the anodic HOR, since the PGM-based electrocatalysts show much faster kinetics toward the HOR in acidic electrolytes. In spite of this fact, the impurities, *i.e.* H_2S and CO, from H_2 supply for H_2–O_2 fuel cells are usually detrimental to PGM-based electrode catalysts, thus hampering their implementation. Wang *et al.*[258] demonstrated that the pyridine ring of organic 2,6-diacetylpyridine (DAcPy) with tilted orientation could create a height-limited space on Pt with a high steric hindrance (Fig. 11a), which was permeable for "small" H_2 while blocking the adsorption of larger-sized H_2S (4.47 Å) and CO (2.65 Å). As such, DAcPy-modified Pt worked as the anodic HOR catalyst with higher H_2S and CO tolerance in 0.5 M H_2SO_4 (Fig. 11b), although only 19% of the initial surface sites of Pt were retained free after organic modification. In addition, by applying the concept of "catalysis under shell", Sun *et al.*[259] prepared a PtRu/C catalyst encapsulated by few-layer graphitic boron nitride (h-BN) shells for PEMFCs. When used as the anodic catalyst in a single cell test, the obtained PtCu@h-BN/C showed comparable HOR activity with commercial PtRu/C but much strong CO-tolerance ability in the presence of 30 ppm of CO in H_2 feed gas. It was ascribed to the confinement effect of h-BN shells on PtRu NPs by weakening the adsorption of CO.

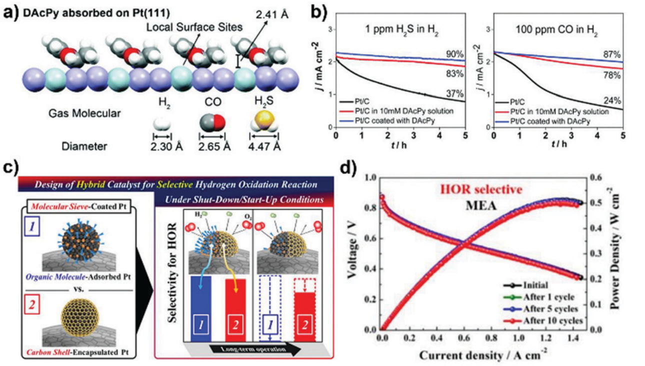

Fig. 11 (a) The side view of the proposed model for reduced-form DAcPy adsorbed on Pt(111). (b) H_2S and CO tolerance tests in a 0.5 M H_2SO_4 solution saturated with 1 ppm H_2S and 100 ppm CO balanced H_2 gas at 0.1 V_{RHE} and 1600 rpm. Reproduced from ref. 258 with permission from Royal Society of Chemistry, Copyright 2018. (c) Schematic illustration (left) of molecular sieve-coated Pt catalysts using organic materials and carbon shells; the changes in HOR selectivity (right) of the catalysts during the long-term operations in PEMFCs. (d) Changes in the single-cell performance of the HOR-selective MEA after shut-down/start-up cycles. Reproduced from ref. 261 with permission from American Chemical Society, Copyright 2019.

Under shut-down/start-up conditions, unexpected ORR on the anode side because of the crossover of O_2 through the membrane could cause a high cathode potential, which could lead to oxidative corrosion of carbon supports and performance degradation of electrocatalysts. Surface engineering of Pt NPs with coatings acts as a kind of promising strategy to overcome this issue. As earlier reported by Marković's group, patterning Pt with a self-assembled monolayer of calix[4]arene molecules featuring a wide rim structure endowed the catalyst with a high selectivity for the HOR.[63,64] High occupation of Pt by the calix layer could not change HOR activity since it has fast kinetics in an acidic electrolyte. In contrast, the ORR was inhibited because of the insufficient sites for O_2 adsorption and O–O bond cleavage on the Pt surface following the organic patterning. Similarly, an enhanced HOR selectivity was attained by using fine-tuned dodecanethiol/Pt ensemble sites after optimizing the concentration of surface organic molecules.[260] In this study, high durability was achieved from the cell test, although part of thiol groups would be detached from the surface. The instability of organic molecules coated on the Pt/C catalyst was also revealed from the work of Jang *et al.*[261] Oleylamine-coated Pt NPs supported on carbon material were first prepared, denoted as Pt@C/C ASP. Following annealing at 600 °C and 900 °C in an Ar atmosphere, Pt@C/C ASP got converted into a nanoporous carbon molecular sieve-encapsulated Pt catalyst, named Pt@C/C 600 and Pt@C/C 900, respectively. The HOR selectivity and electrochemical stability of the attained catalysts were evaluated by collecting ORR and HOR polarization curves after every 1000 cycles between 0.05 and 1.05 V_{RHE} in Ar-saturated 0.1 M $HClO_4$. The results indicated that the ORR activity of Pt@C/C ASP was totally recovered after 3000 cycles due to the detachment of organic molecules, whereas that of Pt@C/C 900 was slightly changed and showed an excellent long-term durability combined with a high selectivity to the anodic HOR (Fig. 11c). According to the authors, a higher pyrolysis temperature promised the formation of nanoporous carbon shells featuring a higher carbon density and smaller pore size, which were responsible for the selective permeation of H_2. The potential application of Pt@C/C 900 as the anode catalyst in PEMFCs was evidenced by transforming it into a membrane electrode assembly (MEA). In comparison with the conventional MEA with severe degradation after the first cycle, the HOR-selective MEA showed well maintained single-cell performance after running for 10 shut-down/start-up cycles (Fig. 11d).

Coating with a metal oxide overlayer can also boost the HOR efficiencies of PGM-based electrocatalysts. Owing to the oxygen-deficient and high oxophilic character, CeO_x has been applied in the development of Pd–CeO_x nanocomposites with intimate contact between Pd and CeO_x for the alkaline HOR.[262] Speck *et al.*[263] fabricated a quasi-2D Pd/CeO_x buried interface by ALD technology to investigate the HOR activity and stability in an alkaline electrolyte. In this work, the accelerated alkaline HOR activity was ascribed to the bifunctional mechanism where the adsorption/dissociation of H_2 takes place on Pd sites and the CeO_x film provides OH^- to facilitate the desorption of strongly adsorbed H on Pd *via* the Volmer step. Benefiting from the semipermeable property of the CeO_x film, much high stability of Pd was achieved since it could not only prevent the metal from oxidation but also impair the outward diffusion of metal ions to the bulk electrolyte. In addition to CeO_x, TiO_x encapsulation of Pt NPs by forming strong metal support interactions (SMSIs) is effective at tuning the HOR selectivity. Stühmeier *et al.*[264] reported that partial-encapsulation of Pt NPs with TiO_x overlayers through reductive heating treatment could hinder the process of Pt oxidation and oxygen reduction, while allowing superior HOR selectivity and activity at high potentials. The influence of SMSIs on the electrochemical behavior of Pt was investigated by Geppert *et al.*[265] Coating with a TiO_x thin-film could reduce the ability of Pt to catalyze the ORR and OER, while no influence was observed on the HOR even above 1.2 V_{RHE}. These findings were attributed to the selective permeability of the TiO_x film, allowing proton and hydrogen diffusion but impairing the transport of oxygenated species.

3.2.2 Overcoated non-precious metal based HOR electrocatalysts. The development of cost-effective non-precious metal based electrocatalysts for the alkaline HOR has fallen far behind that for the ORR and HER.[266] Currently, Ni-based materials are the most studied non-PGM catalysts for the alkaline HOR.[267] Pristine Ni is not active for the alkaline HOR process, which has been widely discussed to be because of its strong affinity to surface intermediates. Great efforts have been accordingly made to enhance the electrochemical efficiencies of Ni toward the alkaline HOR. Typically, alloying with another metal (*i.e.* NiMo,[268,269] NiCu,[270] CoNiMo,[271] NiWCu[272]), doping with a non-metal element (*i.e.* N, B),[273,274] strain engineering[275] and interfacial construction[276] have been validated to be available attempts for modulating the electronic structure of Ni and optimizing the binding interactions with surface intermediates. The HBE of Ni can also be tuned through the synergistic ligand effects by supporting Ni NPs on heteroatom-doped carbon materials.[277,278] A delicate balance for the adsorption behavior of H* and OH* on metal active sites is generally required for the alkaline HOR. Similar to what has been deployed for PGM-based HOR electrocatalysts,[251,279] fabricating Ni/metal (hydr)oxide heterostructures is effective for enhancing the alkaline HOR activity.[280] The introduction of metal oxides at the interface of Ni could increase the hydroxide binding energy[281,282] and decrease the hydrogen adsorption energy.[282–285] The Ni (hydr)oxide amount or the $Ni^0 : Ni^{2+}$ ratio on the Ni interfacial surface oftentimes determines the HOR performance. For instance, a volcano-type dependence of HOR specific activity was revealed on Ni/NiO_x electrodes, in which the catalyst with 30% coverage of NiO_x on its surface showed a 14-fold increase.[285] In addition, when the molar ratio of $Ni(OH)_2$/Ni was around 1.1/1, maximum HOR activity was obtained on the $Ni(OH)_2$-decorared Ni/C catalyst that was generated by an electrochemical oxidation method.[286]

Stability is one of the important criteria for pursuing cost-effective HOR electrocatalysts. Under a higher anodic potential (*i.e.* 0.7 V), metallic Ni-based catalysts can be fully oxidized in the long-term HOR process, causing performance deterioration.[287] Apart from alloying with another metal, overcoating of Ni NPs with inorganic nanoshells was proven to be efficient for improving the antioxidation capability of Ni-based catalysts. For example, Gao *et al.*[288] revealed that coating with a few-layer hexagonal boron nitride (h-BN) shell resulted in weakened interaction of O, H and OH species on the Ni surface and thus a better alkaline HOR performance catalyzed by the retained metallic Ni. Later, the group of Zhuang reported carbon shell-overcoated Ni catalysts for the alkaline HOR.[289] The Ni catalysts were generated by vacuum pyrolysis of nickel acetylacetonate under different temperatures. In this study, Ni@C-500 °C delivered the highest utilization of Ni active sites and the best HOR activity among the catalysts obtained. Although a higher pyrolysis temperature, *i.e.* 600 °C and 700 °C, benefited the formation of carbon shells with a higher graphitization degree and a higher percentage of Ni^0, the ECSA of Ni@C catalysts showed a markedly decreased trend since the carbon shells would hinder the interaction of the electrolyte with the inner Ni cores. This study demonstrates that carbon shells are able to prevent the passivation of metallic Ni during the electrochemical HOR process. On the other hand, the thickness of the carbon nanoshell needs an elaborate control for achieving high HOR activity, as the intrinsic HOR activity can be more than 100% increased when decreasing the thickness of carbon from three to one layer.[290] It is worth noting that, not limited to Ni, the heteroatom-doped carbon layer has also been applied to fabricate transition metal carbides, *i.e.* W_2C@N,PC (N,P-doped carbon encased W_2C NPs), as the promising alternatives to Pt/C for the HOR catalysis across a whole pH range.[291]

In spite of the progress related to the transition metal based materials, the alkaline HOR activities of these catalysts are still inferior to those catalyzed by PGM-based electrocatalysts. According to the cell performance tests in AEMFCs, a power density of around 1000–1200 mW cm^{-2} can be achieved on PtRu[292] and CeO_x–Pd/C[262] anodic catalysts. On the other hand, the power density obtained from Cr@Ni[293] and Ni_3Mo/C[268] was only 70 and 120 mW cm^{-2}, respectively. In addition, non-precious metal catalysts usually have a thick layer on the anode because of the need of high loading, which would have a pronounced impact on the mass transfer of reactants and water management.[289] Accordingly, facile synthetic strategies along with the combination of advanced characterization technologies with theoretical calculations are desired to engineer highly active and stable HOR electrocatalysts for practical application in AEMFCs.

3.3 Overcoated electrocatalysts for direct alcohol fuel cells

The direct alcohol fuel cells, in particular, the direct methanol fuel cells (DMFCs), are promising portable power sources due to the high power density and high efficiency. In DMFCs, the poisoning of PGM-based electrode catalysts caused by the carbonaceous intermediate, *i.e.* CO, usually impairs the cell performance. Intriguingly, the strategy of catalyst overcoating engineering provides the opportunities of improving the anti-poisoning capability of electrocatalysts towards CO in the process of MOR. The underlying origin of the CO anti-poisoning ability of polymer double-shelled electrocatalysts for highly efficient MOR catalysis was proposed by Yang *et al.*[76,77,79] The PyPBI overlayer could stabilize Pt–OH_{ad} by forming Pt–OH–N= species through hydrogen bonding. The stabilized Pt–OH_{ad} then facilitates the oxidation of CO to CO_2 (Pt–$(CO)_{ad}$ + Pt–OH_{ad} → CO_2 + H^+ + e^-). On the other hand, the PVPA coatings with multi OH groups could undergo hydration reactions to accelerate the formation of Pt–OH_{ad} (Pt + H_2O → $Pt(OH)_{ad}$ + H^+ + e^-), which consume further Pt–$(CO)_{ad}$ species to generate active Pt surface. They demonstrated that the kinetics of MOR can be accelerated because of the fast oxidation of CO to CO_2 in the presence of multi OH groups from the polymer overlayers. As mentioned in Section 3.1, the employment of pyridine molecules on the cathodic Pt/C catalyst helped to significantly avoid the adsorption of methanol and ensured a high ORR efficiency.[221] However, as a consequence of the cooperation of steric and electronic effects from pyridine, when pyridine-capped Pt/C was used as the anodic catalyst for the MOR, the MOR mass activity linearly decreased with the increased coverage of pyridine on the catalyst surface. This work indicates that the impact of organic ligands on metal-based catalysts needs specific study and understanding for implementation in various catalytic reactions.

A typical example of a carbon nanoshell-encapsulated catalyst developed with high activity for the MOR is Pt_3CoRu/C@NC, as reported by Wang *et al.*[294] On the surface of commercial Pt/C, they built two space-confined interfaces by overcoating of the PDA layer followed by the addition of Ru^{3+} and Co^{3+} atoms and the sequential overcoating with the inorganic SiO_2 shell. The inner PDA layer not only serves as the precursor of N-doped carbon but also provides chelating sites for Ru^{3+} and Co^{3+} atoms. In the process of H_2-assisted pyrolysis, the outer SiO_2 shell could avoid PDA decomposition loss and prevent as-formed Pt_3CoRu NPs from coalescence and sintering. The obtained Pt_3CoRu/C@NC in this example, when used as the MOR catalyst, showed 4.2 times higher mass activity (0.97 mA μg_{Pt}^{-1}) and 5.3 times higher specific activity (1.6 mA cm^{-2}) compared to that of the commercial Pt/C catalyst. CO stripping voltammograms showed that the onset potential (0.35 V) of CO_{ad} oxidation on Pt_3CoRu/C@NC was more negative compared to that on Pt/C with 0.82 V, pointing to a higher CO-antipoisoning ability during the MOR catalysis. Electrical modification of Pt with Ru and Co is responsible for facilitating the methanol dehydrogenation process and the removal of surface-generated CO_{ad} species. Pt_3CoRu/C@NC also possesses an improved structural and chemical stability because of its ordered structure and the protective aid of the carbon nanoshell.

In addition, membrane-coated electrocatalysts for the MOR were also studied on the basis of the strategy of controlling transport phenomena on the catalyst surface.[138] A silicon oxide (SiO_x)-buried Pt thin film electrode was fabricated by Robinson *et al.*[295] as a highly active MOR electrocatalyst. The overcoating-derived permeable SiO_x overlayer with less than 10 nm thickness could prevent metal Pt from corrosion and maximize the density of active sites at the metal|metal oxide interface. In this work, a distinct increase of CO-tolerance ability was indicated by collecting CO stripping voltammetry curves, from which the CO oxidation peaks were found to shift to negative potentials when increasing the thickness of the SiO_x overlayer. In addition, silanol groups on SiO_x played a promoting role in the removal of CO_{ad} species from the surface of Pt (which is known as the bifunctional mechanism) and thereby a 2-fold activity enhancement towards the MOR compared to the bare Pt thin film electrode was achieved.

3.4 Comparison of the surface coatings suitable for the electrochemical reactions in PEFCs

In view of the fact that the organic and inorganic coatings as discussed above are all beneficial for the electrochemical reactions in PEFCs, the surface overcoating strategy could usher in emerging opportunities for demand-guided design of electrocatalysts to deal with the practical application use. Generally, the benefits from coatings on metal NPs are most frequently reported in terms of stability improvement and reaction kinetics control. The overcoating layer especially the carbon nanoshell and metal oxide could act as a physical barrier toward the metal NP coalescence/sintering and detachment from the surface of the catalyst. The direct contact of the electrode catalyst with the highly oxidative or corrosive electrolyte could also be avoided by the coating overlayers, thereby suppressing the metal dissolution, surface passivation and catalytic deactivation. It is therefore expected that carbon nanoshells and metal oxide overlayers are more suitable when considering the improvement of both structural and chemical stability of metal catalysts for the ORR, HOR and alcohol electrooxidation reactions under different operating conditions in PEFCs.

The mechanisms of overcoating in controlling the reaction kinetics of metal catalysts can be mainly classified into the following three categories: (i) size-selective eletrocatalysis, (ii) electronic interactions and modulations, and (iii) overlayer-assisted electrocatalysis (can also be called the bifunctional mechanism). Depending on the molecular size of reactants and/or spectator species, the coating overlayer can be rationally constructed to control their transport on/to the metal surface. As such, extremely high catalytic selectivity toward the HOR *vs.* ORR (under shut-down/start-up conditions in H_2–O_2 fuel cells)[63,64,260,261,265] and the ORR *vs.* MOR (the case associated with methanol crossover in DMFCs)[51,54,56,75,219–221] has been achieved. ORR and HOR catalytic activity can be additionally enhanced because of the abundant active sites free from blocking by poisoning species.[224–227,258,259] Moreover, the organic surfactant/polymer and heteroatom-doped carbon nanoshell can bring in the electronic effects on metals by modulating their affinity to reactants and active surface intermediates (*i.e.* H*, OH*, OOH*) with appropriate binding states and, thus boosting the ORR and HOR activities. However, the reports on the electronic effects of metal oxides especially the silica overlayer for catalyzing the electrochemical reactions such as ORR and MOR are limited. Furthermore, polymer and metal oxide overlayers are the suitable coating of choice for overlayer-assisted electrocatalysis. In particular, this concept has been validated to be efficient for accelerating alcohol electrooxidation reaction and circumventing the CO-poisoning issue in DMFCs.[76,77,79,295] By providing hydroxyl groups on the surface, metal oxides can also facilitate the sorption behaviour of H during the alkaline HOR process.[263] Based on these advances, it is important to select a suitable coating overlayer for enhancing the efficiencies of metal based catalysts in diverse electrochemical reactions. It is also necessary to exploit the knowledge of the stability of coatings on the metal surface under a variety of conditions. Any single effect or the co-existence of these catalytic effects as discussed above may influence catalyst's catalytic performance, which also depends on the operating conditions, *i.e.*, testing configurations. Reasonable differentiation and quantitative understanding of these beneficial effects are still in their developing stage, which calls for great experimental efforts to deal with the practical distribution of overcoating-derived electrocatalysts in PEFCs.

3.5 Overcoated supports for the electrocatalysts in PEFCs

3.5.1 Carbon support. In this section, the merits of the overcoating-modified carbon support are detailed: (i) inhibiting the corrosion of the carbon support; (ii) improving the dispersion of metal particles; and (iii) forming strong metal–support interactions.

Inhibiting the corrosion of the carbon support. Polymers[65,79,151] and metal oxides such as SnO_2,[204] Ta_2O_5,[205] SiO_2,[296] and ZrO_2[297] can efficiently protect the carbon support from oxidative corrosion under operating conditions. From XPS quantitative analysis, unobvious carbon loss presumably by the way of carbon oxidation to CO_2 or CO was observed on Pt/C@PANI.[65] PANI coatings endowed the carbon support with extremely robust functionality, which could reduce the probability of Pt NP degradation. It was verified by the findings from the accelerated stress tests (0–1.2 V_{RHE}) that, only 30% ECSA loss was observed on Pt/C@PANI, lower than that (83%) of Pt/C. In addition, based on the cyclic voltammetry (CV) curves of the polymer double-shelled NanoPC/PyPBI/Pt/PVPA catalyst,[79] a comparison with that of commercial CB/Pt showed a smaller hydroquinone–quinone (HQ/Q) redox peak even after 50 000 potential cycles (1.0–1.5 V_{RHE}) in 0.1 M $HClO_4$ at 60 °C, indicating a higher resistance towards corrosion after overcoating the carbon support with polymers. In this work, the origin of the high stability of the carbon material was speculated to be the multi-point acid–base interactions between outer surface-coated PVPA and PyPBI, the latter was overcoated on nanoporous carbon (NanoPC).

The mechanism of inherent stability improvement by overcoating PBI polymer layers on carbon black was studied by Fujigaya *et al.*[158] Based on N_2 physical-adsorption analysis, they discerned the conclusion that PBI overlayers would preferentially coat the gate of micropores and interior mesopore sites, rather than the surface of micropores inside the carbon support. Since the inner micropore surface has a high degree of defects, PBI overlayers could efficiently suppress the penetration of the electrolyte into micropores, and thus preventing the carbon matrix from being oxidatively corroded. This protection mechanism is believed to be applicable to other kinds of polymer-overcoated carbon-supported metal catalysts.

Improving the dispersion of metal nanoparticles. Carbon materials with a highly crystalline graphitic structure and good electrical conductivity are ideal supports for electrocatalysts. Insufficient functional groups on the surface of the carbon support usually weaken the stabilization effect on metal NPs. Such limitation on the carbon support could be overcome by overcoating with organic materials such as PyPBI,[72,73] PANI,[150–152] PDA,[156] Ppy,[157] and PBI[159,160] or by surface-grafting NH_2- and SO_3H-containing functional groups.[298] Aniline molecules adsorbed on CNTs have been reported to serve as the separate coordination sites for Pt^{4+} and strongly interact with the reduced Pt(0) particles to have a high dispersion.[299]

Polymer overcoatings on the carbon support could help in the fine control of the size and size-distribution of supported metal NPs through strong coordinations,[72,73,152,159] although the electrical conductivity of the catalyst may be affected. We note that, owing to the fact that polymer overlayers preferentially block the gate of micropores in carbon,[158] the deposition of metal entities in the micropores could be suppressed;[151,160] therefore, the utilization efficiency of metal active sites is expectantly raised. In this respect, PyPBI-coated carbon black allowed less Pt loading with the smallest particle size (2.4 ± 0.2 nm) and the highest ECSA ($120.8 \pm 12.0\ \mathrm{m^2\ g_{Pt}^{-1}}$) on CB/PyPBI/$Pt_{0.1}$/PVPA (0.1 is the weight ratio between Pt feed and polymer-coated carbon support).[78] A record MOR mass activity ($1860\ \mathrm{mA\ mg_{Pt}^{-1}}$) was thus achieved, together with 10 times higher durability than commercial CB/Pt. Also, as higher as 92% utilization efficiency of Pt was realized on CNT/E-HBM/Pt (E-HBM: end-capped hyperbranched sulfonated macromolecules), outperforming that (64%) of CNT/Pt without polymer overcoating on the CNT support.[300] Electrochemical tests on CNT/E-HBM/Pt showed 20 and 1.4 times higher durability and ORR mass activity than the reference CB/Pt catalyst, respectively.

As a consequence of the formation of metal–N bonding, when metal NPs are loaded on polymer-overcoated carbon support materials, stabilized metal species with high dispersibility could be achieved. A high electrocatalytic activity is related to the improved utilization efficiency of active sites. It can also be attributed to the favourable electronic structure of metal nanostructures modulated by the coordination sites (or the defects) from the carbon support. An example of this is the immobilization of PtCo alloy NPs on PNIPAM-functionalized carbon (C-PNIPAM).[169] In this work, the electronic structure of PtCo was remarkably changed by surface Co–N species, which were formed between Co atoms and PNIPAM. The formation of Co–N bonds not only indirectly enhanced the electron transfer from Co to Pt, but also hindered the oxidation of surface active sites. As a result, PtCo/C-PNIPAM displayed higher ORR activity and degradation resistance, in comparison with PtCo/C without PNIPAM functionalization. However, it was recently demonstrated by Kato *et al.*[167] that the PBI overlayer on the carbon support could not impose an effect on the electronic structure of PtNi nanoframes immobilized but, instead, tended to stabilize Pt–$(OH)_{ad}$ species under the ORR conditions for activity improvement. Indeed, they found the electronic effect from the corresponding N-doped carbon-supported PtNi catalyst. These results indicate the importance of manipulating the microscopic environment of N atoms at the metal/support interface for efficient electrochemical reactions, which is expected to be a general scenario applicable for other heteroatoms.

The Nafion ionomer is widely used as the proton conductor and catalyst binder during the fabrication of the MEA. In most cases, the distribution of Nafion on the MEA is rather inhomogeneous and its content often has a large impact on the accessibility of reactants to metal sites. As from the recent works by Yang *et al.*[301] and Jayawickrama *et al.*,[160] when PyPBI and PBI adhesive overlayer-coated carbon materials were applied as the supports for the loading of Pt NPs, a homogeneous coating of the Nafion ionomer on the MEA was achieved. It was attributed to the existing acid–base interactions between the acid sulfonic group of the Nafion ionomer and the basic imidazole group of polymer coatings.[301] The consequence is that, the formation of a long-range proton conduction path is facilitated, and metal utilization efficiency and structural stability are improved as well. The above results indicate the high possibilities of the polymer overcoating strategy for efficient electrocatalyst design, although the intrinsic aspects that are responsible for enhanced catalytic performance need careful studies in each case.

Forming strong metal–support interfacial structures. A wide assortment of metal oxides such as TiO_2,[190,199] AlO_x,[193] ZrO_2,[191] CeO_2,[194] Ta_2O_5,[205,302] MnO_x[207] and MoO_x[209] have been investigated for the surface modification of carbon supports. Semiconducting TiO_2 doped with Ta/Nb[197] and N[303] atoms with improved electrical conductivity is also employed. Apart from mitigating the corrosion of the carbon support and promoting the dispersion and utilization efficiency of the metal,[193,200,210,296,297] metal oxide species in the form of particles or thin films could strongly interact with the metal NPs immobilized on carbon support materials.[189,192,194,204,205,207] Recently, the studies of surface and interfacial interactions are becoming extremely vital for engineering advanced heterogeneous catalysts.[304] Thus far, remarkable progress has been made in the understanding of metal–support interactions on metal-supported electrocatalysts, in particular, in which metal oxide coatings are present on the surface.

A metal–metal oxide–graphene triple junction was formed after the deposition of 2 nm Pt NPs onto indium oxide (ITO) nanocrystal-decorated graphene hybrids.[305] This triple junction is distinguishable from TEM images (Fig. 12a and b) and its formation is thermodynamically favourable, as revealed by DFT calculations. Electrochemical tests on Pt–ITO–graphene hybrids show remarkable ORR activity and stability in comparison to Pt–graphene (Fig. 12c and d) and most of the other Pt metal based catalysts. Since then, creating a metal–metal oxide–support triple-phase boundary has paved the way for developing highly efficient ORR electrocatalysts such as Pt–TiO_2/C,[171] Pt/MnO_2/GS (GS: graphene sheet),[306] Pt–SnO_2–prGO (prGo: protected and reduced graphene oxide)[307] and ALD–TaO_x–Pt/C.[192] Particularly, we note in passing that area-selective ALD was readily applied for the selective nucleation and growth of TaO_x particles (with 2.7 ± 0.5 nm diameter) around the carbon-supported Pt NPs.[192] The triple junction structure of Pt–TaO_x–C was imperative for the formation of strong metal–support interactions and, thereby stabilizing the as-immobilized Pt NPs and minimizing the ECSA loss during the electrocatalytic processes in PEFCs.

Both geometric and electrical modifications occur on the metal, metal oxide and carbon support, which, in turn, induce the formation of unique interfacial active sites. Akalework *et al.*[200] performed XPS and X-ray absorption spectroscopy (XAS) characterization to gain an in-depth understanding of metal–support interactions on ORR electrocatalysts. One of the findings of the negative shift of the Pt 4f XPS peak compared to uncoated Pt–MWCNTs is indicative of the interaction of Pt with

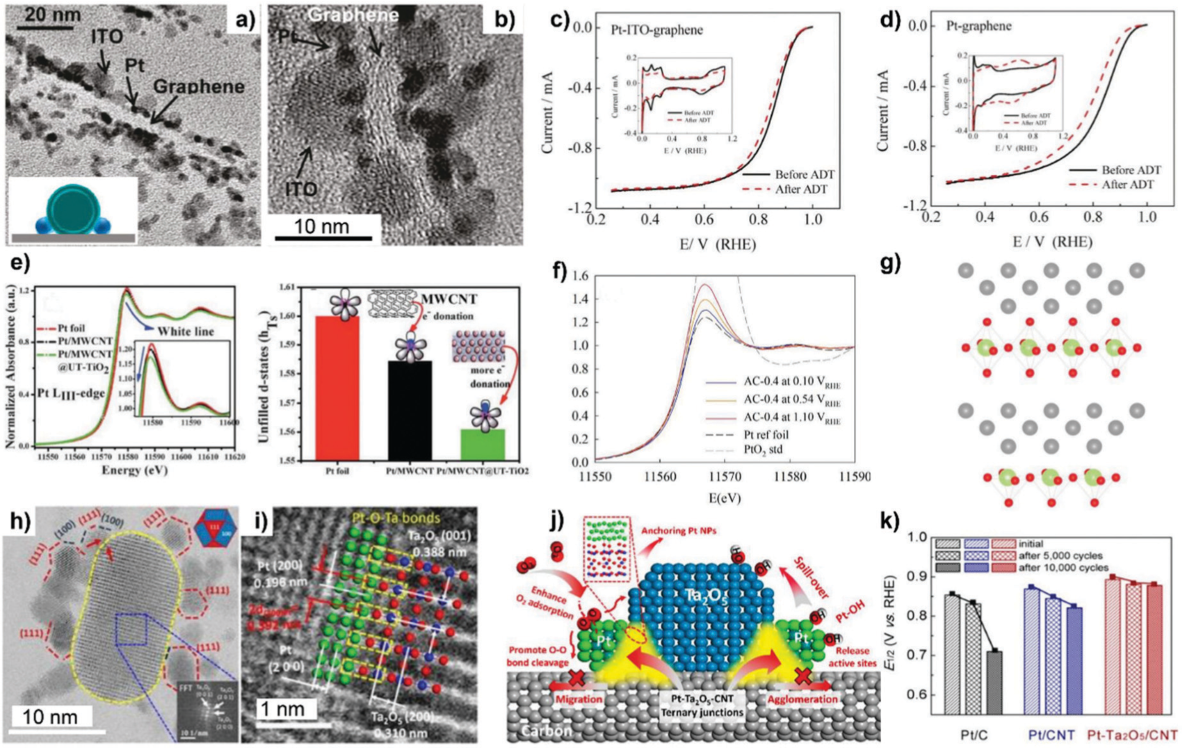

Fig. 12 (a and b) Cross-section TEM images of Pt–ITO–graphene hybrids. The inset in (a) is the schematic structure of the Pt–ITO–graphene nanocomposite. LSV ORR polarization curves of Pt–ITO–graphene (c) and Pt–graphene (d) in O_2-saturated 0.1 M $HClO_4$ (5 mV s^{-1}, 1600 rpm). Inset: CVs in N_2-saturated 0.1 M $HClO_4$ (50 mV s^{-1}). Reproduced from ref. 305 with permission from American Chemical Society, Copyright 2011. (e) Pt L_3-edge XANES spectra (the inset shows an enlarged region of peaks), while the right bar graph is the calculated unfilled d-states for Pt foil and other catalysts. Reproduced from ref. 200 with permission from Royal Society of Chemistry, Copyright 2012. (f) XANES spectra of AC-0.4 collected at the Pt L_3-edge at 0.1 V_{RHE}, 0.54 V_{RHE}, and 1.1 V_{RHE} in O_2-saturated 0.1 M $HClO_4$. (g) Interfaces between Pt and the saturated Nb_2O_5 (up) and unsaturated NbO_x (down); silver, green, and red balls represent Pt, Nb, and O, respectively. Reproduced from ref. 308 with permission from American Chemical Society, Copyright 2017. (h) HAADF-STEM image (the inset shows the FFT pattern in the blue region) and (i) enlarged image of Pt–Ta_2O_5/CNT. (j) Schematic of the mechanisms responsible for the improved ORR activity and durability on Pt–Ta_2O_5/CNT. (k) Half-wave potential ($E_{1/2}$) values after 5000 and 10 000 cycles. Reproduced from ref. 309 with permission from American Chemical Society, Copyright 2019.

ultra-thin TiO_2-overcoated MWCNTs through forming SMSIs. As illustrated in Fig. 12e, the white line intensity (the d-band vacancy indicator) of the Pt L_3-edge X-ray absorption near edge structure (XANES) follows the trend Pt foil > Pt–MWCNT > Pt–MWCNT@UT-TiO_2. The formation of SMSIs and the decrease of Pt d-band vacancy provide evidence for the efficient ORR electrocatalytic property of Pt-MWCNT@UT-TiO_2.

The nature of metal and metal oxide interactions (MMOIs) was intensively studied by Jia *et al.*[308] in a representative Pt/NbO_x/C system, where NbO_x was saturated on amorphous carbon (AC) while it was unsaturated on the graphene nanoflake (GF) support. Electron transfer from Pt to NbO_x was firmly verified by the collected Pt L_3-edge and Nb K-edge XANES spectra. The *in situ* XANES spectra of the Pt L_3-edge for AC-0.4 (Pt/Nb ratio is 0.4), especially that collected at 0.1 V_{RHE}, show higher white line intensity than that of Pt foil, indicating the formation of Pt–O interactions between Pt and O species of NbO_x (Fig. 12f). Until the potential reached 1.1 V_{RHE}, the Pt–O peak shows a drastic increase and Pt–Nb interactions still exist on AC-0.4. Nevertheless, Pt on Pt-NbO_x/GF was found to mainly interact with Nb during the entire voltage cycling. These findings point out that the composition of the metal–metal oxide (MMO) interface determines the interaction of Pt with either oxygen atoms or metal cations in metal oxides. As illustrated in Fig. 12g, Pt atoms interact with Nb in oxygen-deficient NbO_x, whereas Pt–O interactions are first dominant on saturated NbO_x followed by the formation of Pt–Nb bonds when O atoms immigrate onto Pt particles. It is worth noting that the as-formed Pt–Nb species are not the active sites for the ORR. In fact, the shorter Pt–Pt bonds resulting from Pt–O interactions impart the ORR process with high activity. Small-sized and low-coordinated Pt NPs are stabilized by NbO_x with the formation of MMIO, leading to enhanced ORR activity and durability of the studied MMO system.

Gao *et al.*[309] developed a carbon nanotube (CNT) on which 8.8 nm Ta_2O_5 NPs were uniformly dispersed to anchor Pt by forming metal–metal oxide–carbon junctions. HAADF-STEM images indicate that the Pt species, adjacent to the interface between highly crystalline Ta_2O_5 and carbon, tend to expose the {111} and {100} planes and form Pt–O–Ta bonds by lattice fringes overlapping at the Pt–Ta_2O_5 interface (Fig. 12h and i). Similar to the Pt–NbO_x/C described above,[308] the electron transfer was directed from Pt to Ta_2O_5, as revealed by the lower binding energy shift of Ta 4f XPS and the higher Pt L_3-edge

XANES white line intensity of Pt–Ta_2O_5/CNT. Pt–Ta_2O_5/CNT displays higher ORR activity and superior long-term durability than commercial Pt/C and Pt/CNT (Fig. 12k). The improvement in electrocatalytic properties is attributed to the combined features, including the particularly exposed Pt{111} and {100} planes, the electron-deficient Pt (active for O–O bond cleavage), and the spillover effect of Ta_2O_5 by reducing the formation of OH_{ad} on Pt sites (Fig. 12j). In addition, the strong metal–metal oxide interactions formed at the Pt–Ta_2O_5–carbon interface and the highly hindered Pt–O oxidation are advantageous towards inhibiting Pt NPs from migration/sintering and dissolution.

In short, the benefits from surface overcoating engineering on carbon materials in terms of preventing the carbon support from corrosion, improving the metal dispersion degree and forming strong metal–support interactions have been discussed. Further studies of surface overcoating-derived carbon-supported electrocatalysts should be focused on correlating the structural–performance relationships to provide novel guidelines for progress in the design of high-performance electrocatalyst.

3.5.2 Metal oxide support. Metal oxides like TiO_2, CeO_2, SnO_2, and α-Al_2O_3 have also been applied as the support materials for designing electrocatalysts because of their abundant sources and corrosion resistance properties.[310] In addition to the important characteristic of the formation of SMSIs between metal NPs and the metal oxide,[176,178–180] the hydroxyl groups on the surface of the metal oxide can function as the co-catalyst.[310] However, compared to carbon materials, metal oxides show a higher tendency to be agglomerated with a low surface area during high-temperature synthesis and possess lower electrical conductivity, which usually restrict metal dispersion and the corresponding catalytic performance. Attempts to overcoat metal oxide supports with a carbon nanoshell could enable the benefits such as improving electrical conductivity, constraining metal particles from migration/coalescence, and creating abundant active sites for electrocatalysis.[211–217]

Lee's group reported a Pt NP-deposited Mn_3O_4 catalyst with lower ORR mass activity than commercial Pt/C, owing to the smaller ECSA and poor conductivity.[311] They further developed carbon thin layer-coated Mn_3O_4 nanocrystals as a suitable support for Pt NP deposition.[213] Pt was exclusively deposited at the interfacial area between the Mn_3O_4 core and the outer carbon nanoshell, resulting in the formation of a Pt/Mn_3O_4–carbon triple-junction (TJ) structure. The afforded Mn_3O_4/Pts@$C_{1.8nm}$ (the catalyst overcoated with a 1.8 nm-thin N-doped carbon overlayer) exhibited significantly higher mass activity than Mn_3O_4/Pts and Pt/C, which was attributed to the synergistic effect of the TJ structure. Control-synthesized catalysts including Mn_3O_4/Pts@$C_{700°C}$ having larger Pt NPs, Mn_3O_4@$C_{7.1nm}$/Pts without the TJ structure and Mn_3O_4/Pts–CB with physically mixed phase all showed inferior electrocatalytic performance in comparison with Mn_3O_4/Pts@$C_{1.8nm}$. Fabricating a triple-junction nanostructure comprising metal particles, metal oxide and carbon support is readily applicable for the design of various electrocatalysts with promising properties.[171,192,305–309]

Increasing the thickness of the carbon shell on the metal oxide support is beneficial for the improvement of electrical conductivity and the uniform distribution of Pt NPs with high ECSA.[217] A thicker carbon shell (*i.e.* 5.0 nm) on TiO_2, however, could hinder the spillover of –OH species from TiO_2 to Pt, and thus, resulting in inferior CO-antipoisoning ability during the MOR process. It indicates that providing –OH species from the metal oxide by rationally controlling carbon shell thickness is profitable for kinetic enhancement. Such a OH promotor mechanism also holds true for the case of SnO_2-supported Pd NPs for the alcohol electro-oxidation reactions, *i.e.* MOR and EOR, in alkaline solution.[312] The formation of reactive oxygenated species (OH_{ads}) and their delivery to Pd NPs in principle would be limited when overcoating the SnO_2 support with carbon shells. Interestingly, the overcoating-derived catalyst, named Pd–(SnO_2@C)/C, showed remarkable electrocatalytic properties. The proposed rationale for this finding was that the enhancement of electrical interactions between Pd and carbon shell-overcoated SnO_2 acted as the dominant contribution to the high activities of alcohol electro-oxidation reactions. The carbon overlayer could electrically modify the SnO_2 support and subsequently alter the surface adsorption of reaction intermediates, *i.e.* aldehyde and CO_{ad}, to remove them from the catalyst surface and release metal active sites. The electronic interaction mechanism reported in this work could probably provide a guideline for the design of high-performance electrocatalysts in direct alcohol fuel cell applications.

4. Overcoated electrocatalysts for water electrolyzers

Water electrolyzers produce H_2 and O_2 *via* the water splitting process by the application of electrical energy, representing attractive energy storage devices. Electrochemical water splitting comprises the two-electron cathodic hydrogen evolution reaction (HER) and the four-electron anodic oxygen evolution reaction (OER). Pt-Based materials are the most efficient HER electrocatalysts, while IrO_x and RuO_x are active for catalyzing the OER.[313] Owing to the high price and scarcity of precious metals, numerous research efforts have been devoted to the design of low-cost transition metal-based nanomaterials for overall water splitting in acid and alkaline environments.[314] Of particular note, there is often a high demand on long-term durability when electrocatalysts are applied for water splitting in acid solution. To date, rational synthetic strategies are still desirable to improve the utilization efficiency of active sites and enhance the electrocatalytic properties of both precious and non-precious metal catalysts to deal with the efficient application demands in WECs.

4.1 Overcoated electrocatalysts for the OER

The OER, a half-reaction including HO*, O* and HOO* intermediate reactive species, takes place in acid and alkaline solution as follows: $2H_2O \rightarrow O_2 + 4H^+ + 4e^-$ (acidic condition) and $4OH^- \rightarrow O_2 + 2H_2O + 4e^-$ (alkaline condition). OER catalysis shows sluggish kinetics due to the multistep proton coupled electron transfer involved in O–H bond breaking and O–O bond formation. The performance of OER electrocatalysts is usually compared on the basis of some critical parameters such as the overpotential needed to achieve a current density of 10 mA cm^{-2}, Tafel slope (the relationship between current density and overpotential), faradaic efficiency (the charge utilization efficiency for producing desired products) and long-term durability, *i.e.* by recording chronoamperometry curves over operation time.

Earth-abundant transition metal-based OER electrocatalysts especially those applied in an alkaline environment have recently attracted growing research interest. Carbon materials are still the widely employed supports for OER electrocatalyst design, taking advantage of the features such as high structural and chemical stability, and excellent conductivity. In this section, a large number of surface overcoating-derived precious and non-precious metal based OER electrocatalysts will be discussed by correlating their intrinsic structural properties with the electrochemical performance.

4.1.1 Precious metal based OER electrocatalysts. Note that only a few works have reported precious metal based OER electrocatalysts, which are fabricated based on the surface overcoating strategy.[137,146,161] RuO_2 as one of the active OER catalysts would easily convert into unstable RuO_4 at a high potential in acid solution. To circumvent this limitation on acidic OER, Cui *et al.*[137] constructed graphene shells on the surface of RuNi alloys through the CH_3CN CVD process (Fig. 13a). The addition of Ni facilitated the *in situ*-growth of graphene layers. As a key synthetic step in this work, controllable oxidation treatment was carried out on the above catalyst to partially decompose the as-fabricated graphene layers by generating an efficient reaction interface with RuO_2 NPs (Fig. 13b and c). Typically, $RuNi_2$@G-250 after oxidation at 250 °C displays a discontinuous graphene overlayer but the best OER activity with lower overpotential (227 mV) at 10 mA cm^{-2} than that (290 mV) of commercial RuO_2 (Fig. 13d). Higher oxidation temperature, *i.e.* 500 °C, could remove the graphene layers and make RuNi alloys completely oxidized into RuO_2 NPs, leading to a decreased oxygen-evolving catalytic activity. Theoretical calculations suggested that the interface between RuO_2 and graphene layers can significantly stabilize the free energy of HOO* species than that of the O* intermediate, thus reducing the limiting potential to enhance the intrinsic OER activity (Fig. 13e). Moreover, the overcoated graphene layer and its electron transfer with RuO_2 could synergistically prevent RuO_2 NPs from over-oxidation and dissolution, resulting in an extraordinary durability towards the OER.

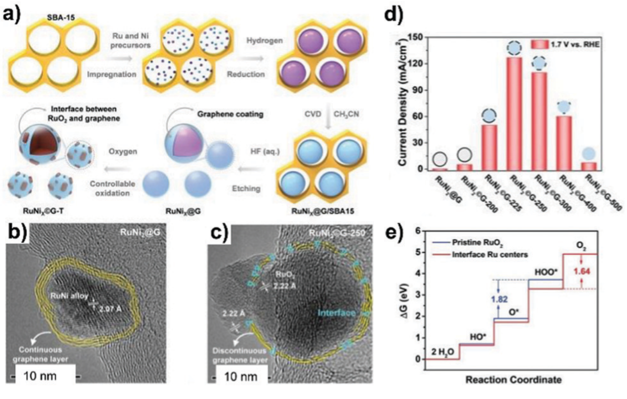

Fig. 13 (a) Schematic of the synthesis of $RuNi_2$@G-T with an interface between RuO_2 and graphene. HRTEM image of (b) $RuNi_2$@G and (c) $RuNi_2$@G-250; the latter has a unique interfacial structure between RuO_2 and graphene. (d) The current densities at 1.7 V_{RHE} of $RuNi_2$@G samples treated under different oxidation temperatures. (e) Free energy profiles for the OER over RuO_2 and the interface Ru centers between RuO_2 and graphene with an armchair edge at zero potential (U = 0). Reproduced from ref. 137 with permission from Wiley-VCH, Copyright 2020.

Compared with RuO_2, IrO_x is the most suitable OER electrocatalyst benefiting from its high durability in acidic solution. Fujigaya *et al.*[161] have demonstrated that PBI overcoating of multi-walled CNTs (MWCNTs) was effective in anchoring small IrO_x NPs and improving their utilization efficiency for a highly active OER catalysis in 0.05 M H_2SO_4. Owing to the superior electrochemical stability of MWCNTs, the as-made MWCNT/PBI/Ir catalyst also exhibited an excellent durability. As chloride species often suppress the OER activity and make metal catalysts dissolved, an efficient control of chlorine evolution reaction (CER) is of vital importance for saline water electrolysis. It has been validated that the OER selectivity in the presence of impurities can be well regulated by overcoating a metal oxide on the surface of active sites. An example of this is the electrodeposited MnO_x thin film serving as a physical transfer barrier towards the diffusion of chloride ions onto the inner IrO_x catalytically active sites, which by itself made no contribution to the OER activity.[146] The diffusion of water, protons and O_2 species from the electrolyte to the active sites remained unaffected in the presence of the metal oxide overlayer on metal sites, as described in this case.

4.1.2 Non-precious metal based OER electrocatalysts

Metal, metal (hydro)oxide and metal alloy. Co-Based materials containing Co^{2+} and Co^{3+} species are active for the OER catalysis. TiO_2 ALD overcoating onto a carbon-supported cobalt catalyst, *i.e.* Co/C, could enhance its OER property.[143] In this work, OER activity was found to increase with ALD cycle number. 60 cycles of TiO_2 ALD (0.79 mg cm^{-2} loading on Co/C) showed 2.5 times higher activity than commercial Pt/C in alkaline solution. An in-depth study revealed that the enhanced activity was attributed to the oxidation of Co by the TiO_2 overlayer through the formation of Ti–O–Co bonds. Co with a high oxidation state was believed to be the active sites for the OER and, the rate determining step, *viz.*, the reaction of adsorbed OH^- with O* to form OOH* species, was accelerated. It is well known that Co-based oxide materials tend to undergo structural self-reconstruction, which leads to a boosted OER activity. In this case, the real active site on graphitic, nanocarbon-coated Co catalyst (named Co@NC-600) for the alkaline OER was identified to be CoOOH/CoO_2 with high oxidation states, which was *in situ* electrochemically formed from metallic Co species.[315] Yu *et al.*[316] synthesized a polyfluoroaniline (PFANI)-coated $Co(OH)_2$ catalyst featured with a core–shell structure for efficient OER application. The small overpotential (265 mV) to achieve a current density of 10 mA cm^{-2} was assigned to several positive aspects such as the optimized electronic structure of Co^{2+} in Co(OH)$_2$ by the fluorine anion from the PFANI layer, the hydrophilic property of Co(OH)$_2$@PFANI and the accelerated charge transfer process after overcoating with 1.7 nm-thin PFANI. In addition, g-C$_3$N$_4$ nanosheet coatings with 10 nm layer thickness can strongly couple with Co(OH)$_2$ nanowires to form abundant active sites and promote the process of electron transfer.[317] As a result, the g-C$_3$N$_4$-overcoated Co(OH)$_2$ nanowires, named Co(OH)$_2$@g-C$_3$N$_4$, manifested a surpassed OER activity in 1.0 M KOH with 320 mV overpotential at a current density of 10 mA cm^{-2}, as well as long-term durability, in contrast to the performance of PGM catalysts (such as IrO$_2$, RuO$_2$, Pt/C) and individual Co- and g-C$_3$N$_4$-based materials.

As already discussed, overcoating metal active sites (*i.e.* Pt, IrO$_x$) with an ultra-thin metal oxide overlayer is valuable for improving electrical reactivity and chemical stability.[146,295] This strategy is applicable for the design of non-precious metal-based OER electrocatalysts as well. For example, Obata *et al.*[318] reported the strategy of overcoating an anodic-deposited CeO$_x$ layer on the surface of NiFeO$_x$ to enhance its stability for the OER in alkaline solution. The permselective CeO$_x$ layer can not only ensure the permeation of OH$^-$ and O$_2$ while preventing redox ions from diffusing through, but also inhibit the dissolution of Fe species during catalysis. In addition, it was validated that the interfacial effects resulting from CeO$_x$ overcoating on metal (hydro)oxide materials such as Ni(OH)$_2$, bimetallic NiFe-hydroxide and spinel Co$_3$O$_4$ could induce strong electronic interactions on the as-coupled interface and enable tuning the electroadsorption of oxygenated intermediates and thus being responsible for the enhanced OER catalysis in an alkaline electrolyte.[319–321]

After studying CNT-confined Fe NPs,[322] Cui *et al.*[136] introduced single layer graphene onto 3d transition metals (Fe, Co, Ni, and FeNi, FeCo, CoNi alloys) by a CH$_3$CN CVD process for the alkaline OER. FeNi@C showed the best OER activity among the catalysts, as shown by 280 mV overpotential to deliver a current density of 10 mA cm^{-2} and excellent durability after 10 000 cycles, outperforming that of the commercial IrO$_2$ catalyst (Fig. 14a). As determined by DFT calculations, the $\Delta G(\mathrm{O}^*) - \Delta G(\mathrm{HO}^*)$ (the activity descriptor) of FeNi@C was 1.48 eV, which is close to the volcano peak. Electron transfer between metals and N dopants was found to enhance the adsorption of reactive intermediates, as reflected by the optimal $\Delta G(\mathrm{O}^*) - \Delta G(\mathrm{HO}^*)$ in Fig. 14b. In addition, effective control of the carbon coating process and careful identification of structural properties of the catalyst are important to be considered.[126,135] During the preparation of N-doped graphitic carbon-coated NiFe NPs by pyrolyzing NiFe-PBA materials, Ni appeared to be more prone to promote the carbon graphitization degree than Fe.[126] The carbon shell with spherical (high Ni/Fe ratio) and tubular (low Ni/Fe ratio) morphology can be respectively obtained by tuning the Ni/Fe ratios in PBA precursors. XPS and XAS results revealed the electron donation from metallic Fe to the carbon shell, while there was no electron transfer for the case of Ni. Instead, Ni was found to strain the NiFe lattice, ascribed to the observation that both Fe–Fe and Ni–Ni bonds shifted in comparison with Fe and Ni foil. In addition to the modifications on the local and electrical structure of NiFe NPs, the N dopants in the carbon shell could make the carbon surface positively charged to facilitate the formation of oxygenated OH* and O* species, and ultimately enhancing the OER activity.[134] Such a synergistic effect was also observed in single-walled CNT-embedded FeCo NPs[323] and FeNi@N-doped graphene.[98] Furthermore, the changes in alloy composition (*i.e.* FeCoNi alloy) by incorporating a third metal into a binary alloy could tune the electron transfer numbers between metal alloy and overcoated graphene layer;[324] thus, the adsorption of surface intermediates was manipulated to achieve enhanced OER properties.[107] Moreover, it was reported that pyrolytic treatment of PBA nanomaterials[325] and ZIF polyhedra coatings[133] could induce the metal-doping of the outer N-doped carbon shell. In these cases, both the synergistic effects and electron penetration from metal-doped NC shells to metal cores benefited the surface-dependent OER process.

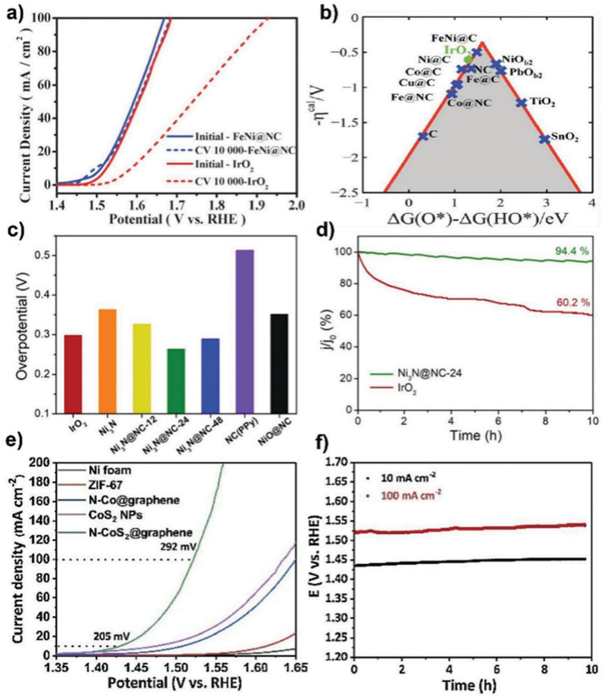

Fig. 14 (a) Durability test of FeNi@NC in an alkaline electrolyte in comparison to IrO$_2$. (b) The calculated negative overpotential (η^{cal}) against $\Delta G(\mathrm{O}^*) - \Delta G(\mathrm{HO}^*)$ on different catalysts. Reproduced from ref. 136 with permission from Royal Society of Chemistry, Copyright 2016. (c) Overpotentials of the catalysts required to reach j = 10 mA cm^{-2}. (d) Chronoamperometric responses at 1.50 V$_{\mathrm{RHE}}$ ($E_{j=10}$ of Ni$_3$N@NC-24). Reproduced from ref. 100 with permission from American Chemical Society, Copyright 2018. (e) Polarization curves of N-CoS$_2$@graphene and other compared samples in 1.0 M KOH at 2 mV s^{-1}. (f) Long-term stability measurements on N-CoS$_2$@graphene in 1.0 M KOH. Reproduced from ref. 333 with permission from Elsevier, Copyright 2020.

Metal phosphides, nitrides and chalcogenides. Metal phosphides and metal nitrides have been vigorously studied as active

OER electrocatalysts. Introduction of a porous nanostructure onto active metal sites enables enhanced OER electrocatalytic properties. For example, Ni–Ni PBA direct pyrolysis-derived porous carbon coating on NiP nanoplates could improve catalyst conductivity, facilitate the charge transfer and reactant diffusion process, and promote the exposure of abundant active sites.[326] In this work, the *in situ*-formed Ni oxide species served as the primary active sites for the alkaline OER catalysis. Likewise, Yu *et al.*[327] reported that, in addition to the function of improving electrical conductivity, the carbon nanoshell could cooperate with the 3D Ni_8P_3 nanosheet for reducing the adsorption energy of intermediate catalytic species and help in protecting the Ni_8P_3 nanosheet from dissolution. As a result, the carbon-coated Ni_8P_3 nanosheet, named C@Ni_8P_3, exhibited better OER activity by offering lower overpotential (267 mV) to deliver a current density of 10 mA cm^{-2} than that (283 mV@10 mA cm^{-2}) of uncoated Ni_8P_3. The decreased Tafel slope (51 mV dec^{-1} *vs.* 78 mV dec^{-1}) indicated facilitated electrokinetics of water oxidation after engineering carbon nanoshell coatings on the Ni_8P_3 nanosheet. In addition to the monometallic phosphides mentioned above, overcoating-derived bimetallic phosphides such as carbon-incorporated hollow-structured NiCoP nanoboxes,[128] nanoporous carbon-coated $Co_{0.7}Fe_{0.3}P$@C[328] and Co_3FeP_x/C[329] have been demonstrated as efficient OER electrocatalysts, in which the synergistic effects between the carbon coating and the metal core are suggested.

Overcoating-derived metal nitrides fabricated for catalyzing the process of OER are limited. Here we present the N-doped carbon-coated Ni_3N holey sheets (Ni_3N@NC) developed by Yuan *et al.*[100] As displayed in Fig. 14c, overcoating a 4 nm-thin carbon shell enables a lower overpotential of 260 mV to obtain a current density of 10 mA cm^{-2} on Ni_3N@NC-24 in 0.1 M KOH, whereas that of IrO_2, NiO@NC, NC and Ni_3N is determined to be 300, 350, 510, and 360 mV, respectively. Ni_3N@NC-24 is also stable in alkaline solution by maintaining 94.4% of the initial activity after 10 h operation, more excellent than that (60.2%) of IrO_2 under the same experimental condition (Fig. 14d). Further increasing carbon shell thickness to 8 nm for the case of Ni_3N@NC-48 is inferior for the OER activity as explained by the access-blocking of the active Ni_3N core.

Metal chalcogenides such as Co-based chalcogenides have drawn increasing research interest because of the features of earth-abundance and high activity for the OER catalysis. There are several reports on the synthesis of Co-based chalcogenides by utilizing the surface overcoating strategy.[145,330–333] In particular, on the N,S-codoped carbon nanofiber-encapsulated Co_9S_8 catalyst for the OER tests in 1.0 M KOH solution, the observed overpotential of 302 mV at a current density of 10 mA cm^{-2} and the low Tafel slope of 54 mV dec^{-1} surpassed the performance of commercial RuO_2.[132] Apart from Co_9S_8, CoS_2 ultrafine NPs overcoated with 1–5 layers of N-doped graphene were prepared by sequential pyrolysis of ZIF-67 and sulfurization with S.[333] The resulted N-CoS_2@graphene catalyst offers 205 mV overpotential to reach a geometrical current density of 10 mA cm^{-2} and a low Tafel slope of 65 mV dec^{-1} in 1.0 M KOH solution (Fig. 14e). In durability tests by keeping at 10 and 100 mA cm^{-2} current density, the potentials of N-CoS_2@graphene are negligibly reduced (Fig. 14f), whereas the CoS_2 NPs without overcoating with a graphene layer are found to be degraded rapidly. Fig. 15 is the comparison and summary of some representative surface overcoating-derived non-precious metal based electrocatalysts for efficient OER catalysis in alkaline solution (1.0 M KOH).[126,132,136,316,317,323,325,327,329,333]

In brief, surface overcoating can bring various benefits for both precious and non-precious metal based electrocatalysts applied in the OER catalysis. The few reports of polymer- or metal oxide-coupled non-precious metal catalysts are limited to the applications in the OER in alkaline solution. In view of their high electrical conductivity, chemical stability and electronic interaction effects on the metal core, heteroatom-doped carbon nanoshells are more suitable compared with the polymer and metal oxide overlayer for the design of high-performance OER electrocatalysts. Typically, the improved inherent structural and chemical stability is attributed to the presence of the carbon shell with a few layers. Based on this functionality of the carbon shell, we expect that, electrocatalysts especially those composed of cost-effective 3d transition metals will be developed to be promising substitutes to precious metals for acidic OER applications. Moreover, by rationally controlling the thickness of the carbon shell, the electron transfer process can be facilitated by means of changing the adsorption behaviour of surface reactive intermediates on metal NPs, thus enhancing the OER in both acid and alkaline solutions.

4.2 Overcoated electrocatalysts for the HER

Hydrogen has shown great potential as a promising energy carrier employed in H_2–O_2 fuel cells for clean and sustainable energy. In addition to production from conventional industrial water–gas shift reaction, hydrogen can be produced by a cleaner and carbon-neutral way, *i.e.* water splitting process in water electrolyzer devices. One of the half-reactions of the HER, a two-electron-transfer reaction, takes place in acid and alkaline solution as follows: $2H^+ + 2e^- \rightarrow H_2$ (acidic condition) and $2H_2O + 2e^- \rightarrow H_2 + 2OH^-$ (alkaline condition). In general, there are two reaction steps involved in the HER process regardless of the type of electrolyte. The formation of adsorbed H (H_{ads}) by

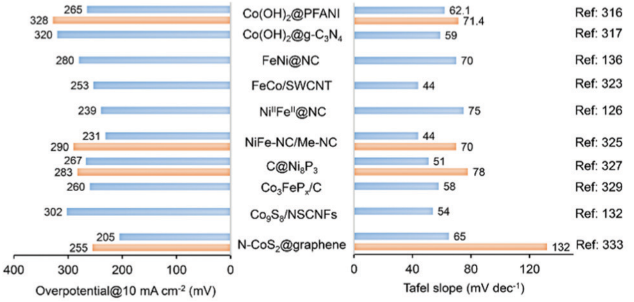

Fig. 15 Comparison of the reported OER electrocatalysts in terms of the required overpotential at a current density of 10 mA cm^{-2} and Tafel slope in 1.0 M KOH solution. The corresponding electrochemical parameters for some of the uncoated catalysts are also plotted (orange color) for comparison.

the discharge of H_2O or hydronium ions (H_3O^+) is the first step, which is known as the Volmer reaction. As the following second step, the production of H_2 proceeds by either electrochemical desorption (Heyrovsky reaction) or chemical desorption (Tafel reaction) of H_{ads}. Both the Volmer–Tafel and Volmer–Heyrovsky processes are involved in the HER. HER electrocatalysts based on precious metals and/or low-cost transition metals have been tremendously developed to reduce cost and adapt well under complex operating conditions.[115,314] Specifically, the HER shows more sluggish kinetics in alkaline solution compared to that in an acidic system, mainly owing to the energy barrier for the generation of H^+ from water dissociation.[334] DFT calculations and recent experimental results have demonstrated that the HBE and oxophilicity can be considered as the dominant thermodynamic descriptors for HER activity,[13,335] as similarly described for the HOR. Based on the Sabatier rule, the binding of catalysts with reactant molecules or intermediates should neither be too strong nor too weak. Hereto, optimizing the HBE on various surface sites is a reasonable solution for engineering optimal HER electrocatalysts for application in WECs. Similar to OER, some critical indexes such as overpotential, Tafel slope, exchange current density, and faradaic efficiency are used to elucidate the HER activity of designed electrocatalysts. In this section, surface overcoating-derived electrocatalysts favourable for the HER catalysis will be discussed.

4.2.1 Precious metal based HER electrocatalysts. PGM-based catalysts are still the best materials capable of catalyzing the process of HER, due to the low overpotential and high exchange current density. Increasingly, the advantage of employing the surface overcoating strategy to further improve their HER electrocatalytic properties has been demonstrated. As discussed in Section 2.1.1, polyallylamine hydrochloride (PAH) is efficiently used to synthesize Pt-based nanostructures with enhanced ORR properties.[52–56] For HER application, there is a report on PAA-assisted chemical reduction synthesis of Pt tripods ($Pt_{tripods}$@PAA) with ultra-thin and ultra-long branches.[57] Owing to the high interface proton concentration and the unique nanostructure, $Pt_{tripods}$@PAA displayed a better HER activity and stability than the reference Pt black. In addition to PAH, polyethyleneimine (PEI) was employed for the one-pot formation of Pt superstructures (Pt-SSs) featuring tetragonal and hierarchical morphologies.[336] As detected from the CV curve, the ECSA of Pt-SSs@PEI (22.4 $m^2\ g^{-1}$) was slightly higher than that (19.9 $m^2\ g^{-1}$) of Pt black. The PEI overlayer with 5.69 nm thickness was found to be loosely packed on the surface of Pt-SSs with a calculated 25.8% of coverage due to the steric hindrance effect. Similar to the PAA on $Pt_{tripods}$@PAA,[57] the $-NH_2$ groups of the PEI overlayer can be protonated into $-NH_3^+$, resulting in promoted concentration of local H^+ at the Pt interface which yielded the improvement of HER activity with a high onset reduction potential (+64.6 mV *vs.* RHE). Pt-SSs@PEI also exhibited outstanding long-term durability as a result of the excellent self-stability of Pt-SSs.

N-Doped hollow porous carbon polyhedron-overcoated Pt (Pt@NHPCP) was demonstrated as an efficient HER electrocatalyst through the pyrolysis of the Pt-encapsulated ZIF-8 nanomaterial.[337] In addition, an ultra-thin 2D carbon layer carbonized from ZIF-67 was able to stabilize Pt NPs on the RGO support.[233] The synergistic effect between Pt and Co–N_x–C active sites (ZIF-67 derivatives) contributed to the improved HER activity in both acid and alkaline solutions. DFT studies revealed that the benefited HER activity in acid solution was originated from the facilitated sorption behaviour of H species (with the lowest HBE of 0.23 V), while in basic media it was mainly due to the accelerated water dissociation (OH–H bond cleavage) to form H_{ad}, which remains the rate-limiting step in the alkaline HER process.

Overcoating an ultra-thin overlayer of metal oxide on the Pt electrode could aid in the achievement of high HER selectivity. Labrador *et al.*[338] prepared a buried Pt/SiO_x interface by overcoating the SiO_x film with different thickness on a smooth Pt thin film. CV curves indicated that Pt was totally located beneath the SiO_x overlayer and H^+ was selectively accessible to Pt sites *via* diffusion through the SiO_x membrane-like coating layer, while the diffusion of Cu^{2+} was blocked. As a result, the HER occurring at the Pt/SiO_x interface exhibited high selectivity in the presence of Cu^{2+}, a model poison for Pt which suppresses the HER activity. Indeed, a platinum oxide (PtO_x) interlayer was identified at the Pt/SiO_x interface and its properties can be regulated by the thickness of the SiO_x or Pt film to result in strengthened electrocatalytic performance.[339]

Other precious metals such as Ru[340] and Ag[341] have been investigated by overcoating or encapsulating with carbon nanoshells for efficient HER catalysis. In particular, a recent work by Li *et al.*[340] reported the preparation of a thin layer of N-doped carbon-coated Ru catalyst by thermally annealing polydopamine-coated Ru NPs (Ru@PDA). To investigate the effect of the Ru crystalline structure on the HER activity, the authors annealed the Ru@PDA composite at elevated temperatures. Ordered hexagonal-close-packed (hcp, (100) (002) surface) and fully crystallized Ru NPs with a diameter of 4 nm were formed when the pyrolysis temperature reached 700 °C. Higher temperature for example 800 °C resulted in the overgrowth of Ru NPs with a lower ECSA. Ru@NC-700 worked as the best HER catalyst in 0.5 M H_2SO_4 among the prepared catalysts, as shown by a small overpotential (27.5 mV) to reach a current density of 10 mA cm^{-2} and Tafel slope (37 mV dec^{-1}) which was nearly close to that of Pt/C. Furthermore, the stability of hcp-Ru@NC-700 was at least 10 times better than that of Pt/C because of the protective aid of the carbon nanoshell.

As alloying with 3d transition metals can lower the loading of PGMs, ultra-thin carbon shell-coated NiRu,[342] RuCo,[343] and IrCo[124] have been prepared through the direct pyrolysis of Ru- or Ir-incorporated MOF nanomaterials. For example, after pyrolyzing Ir-doped Co-PBA at 500 °C, the resultant IrCo@NC-500 catalyst exhibited even lower overpotential (45 mV) to deliver a current density of 10 mA cm^{-2} in N_2-saturated 1.0 M KOH solution, which is 20% above the activity of 20 wt% Pt/C (Fig. 16a and b).[124] A rapid electron transfer process occurred on IrCo@NC-500 as indicated by the smaller Tafel slope (80 mV dec^{-1}) than that (101 mV dec^{-1}) of 5% Pt/C (Fig. 16c). Durability evaluation in 0.5 M H_2SO_4 showcased only a slight cathodic current delay over the initial 5000 cycles due to the leaching of outer-exposed Co species; then, a stable current was reached after 10 000 cycles because of the protection of the inner core by the graphene shell from leaching into the acidic solution. Theoretical studies demonstrated that the charge transfer from the metal core to the outer graphene surface facilitated the adsorption of H* on the graphene overlayer, eventually resulting in enhanced HER activity.

Precious metal-based phosphides hold promise for enhancing the HER activity as well, as a consequence of the regulations on the electronic structure of the metal by incorporated non-metallic P.[108,250] It is known that electrocatalysts with Gibbs free energy of hydrogen adsorption (ΔG_{H^*}) close to 0 eV are active for catalyzing the HER. However RuP_2 has a negative ΔG_{H^*}, meaning that hydrogen atoms are strongly bound to active sites, which results in a hindered process of proton and electron transfer and thereby a delayed HER activity. With this consideration, Pu *et al.*[108] introduced a N,P-codoped carbon shell to improve the HER performance of Ru_2P NPs. DFT calculations revealed a lower absolute ΔG_{H^*} value of RuP_2@NPC than RuP_2, NPC and C. As a result, RuP_2@NPC exhibited an overpotential of 38 mV at a current density of 10 mA cm^{-2} in 0.5 M H_2SO_4, smaller than that of control prepared catalysts. RuP_2@NPC also worked well in neutral (overpotential of 57 mV in 1.0 M PBS (phosphate buffered saline)) and alkaline media (overpotential of 52 mV in 1.0 M KOH) with comparable activity but excellent durability than the commercial Pt/C catalyst. In addition, HER performance of metal phosphides can be optimized through control over P content during the phosphating process.[344] A suitable amount of the P precursor (NaH_2PO_2) in the $IrCl_4/NaH_2PO_2$-blended polymer (which was pyrolyzed under high temperature) was responsible for modulating Ir electronic configuration and tuning the thickness of the N,P-codoped carbon shell to allow an efficient electron transfer process for the HER in a wide pH range.

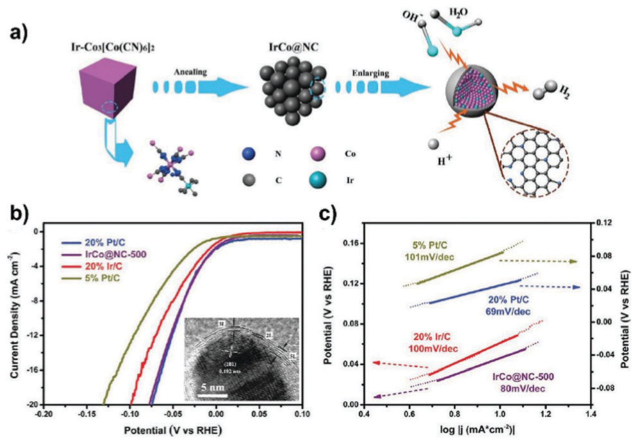

Fig. 16 (a) Schematic illustration of the synthesis of IrCo@NC by direct pyrolysis of Ir–Co–PBA. (b) LSV polarization curves and (c) Tafel slopes of IrCo@NC-500, Ir/C, and Pt/C in N_2-saturated 1.0 M KOH solution. The inset in (b) is the HRTEM image of IrCo@NC-500. Reproduced from ref. 124 with permission from Wiley-VCH, Copyright 2018.

4.2.2 Non-precious metal based HER electrocatalysts

Transition metal, metal (hydro)oxide, metal alloys. Non-precious 3d transition metals (*i.e.* Fe, Co, Ni, Cu) could catalyze the HER process due to the presence of plenty of unpaired *d*-orbital electrons for facilitating hydrogen chemisorption. Carbon nanoshell-coated transition metal based catalysts have been specifically reported to exhibit reinforced HER performance.[345–347] Tavakkoli *et al.*[348] prepared single-shell carbon-coated Fe NPs (abbreviated as SCEINs) decorated on single-walled carbon nanotubes (SWNTs) by the ethylene CVD process. Metallic Fe NPs with a diameter of 2.6 nm were overcoated with an outer single-layer carbon shell, as evidenced by the HRTEM images in Fig. 17a and b. SCEINs/SWNTs displayed high HER activity with about 0 V_{RHE} onset potential and 40 mV dec^{-1} Tafel slope, with the latter being close to that (37 mV dec^{-1}) of Pt/C, when measured in N_2-saturated 0.5 M H_2SO_4 (Fig. 17c and d). There was no observable activity degradation after 1000 potential cycles in the range of −0.15 to 0.15 V_{RHE}, pointing to an excellent durability as a result of the protection of single-shell carbon. In addition, Co species encapsulated within carbon materials have been developed for efficient HER.[103,349–352] An ultra-thin N,B-codoped carbon cage-encapsulated Co catalyst, named Co@BCN, was produced from the pyrolysis of ZIF-67 materials mixed with H_3BO_3.[352] ZIF-67 comprising Co metal nodes and organic linkers serves as the metal precursor and self-sacrificing template. When applied for hydrogen production *via* the HER, the BCN shell on Co@BCN can protect the Co metal from being corroded and oxidized, which results in high stability in extremely corrosive conditions. Dopants such as N, O, and B in the carbon nanoshell are beneficial for synergistically tuning ΔG_{H^*} near to the zero value, thus enhancing the HER activity.[103,352]

In view of the fact that non-precious metal based electrocatalysts exhibit excellent OER properties in alkaline conditions compared to those implemented in acid systems, there are many cost-effective HER electrocatalysts being developed with high performance for alkaline water electrolysis. In particular, there is considerable interest in engineering Ni-based alloys and heterostructured composites as the promising electrocatalysts for the HER in alkaline electrolytes.[353] It has been well documented by the group of Markovic that capping the Pt surface with 3d transition metal hydr(oxy)oxide nanoclusters was effective at boosting the alkaline HER activity.[354,355] They successfully applied such a hetero-junction concept to modify the Ni surface with $Ni(OH)_2$ nanoclusters. The obtained $Ni(OH)_2$/Ni catalyst showed 4 times higher alkaline HER activity than the bare Ni surface, mainly attributed to the promoted dissociation of water.[334] Gong *et al.*[356] demonstrated that pyrolysis-induced partial reduction of $Ni(OH)_2$ could afford NiO/Ni nano-hybrids distributed on the carbon nanotube. The oxidized carbon nanotube played an important role in the formation of the unique Ni@NiO core–shell nanostructure (Fig. 17e and f) by impending the reduction of Ni oxides into Ni particles and preventing them from undergoing further sintering. Compared with the control samples, *i.e.* Ni/CNT and NiO/CNT, NiO/Ni-CNT showed <100 mV overpotential to deliver a current density of 10 mA cm^{-2} at a

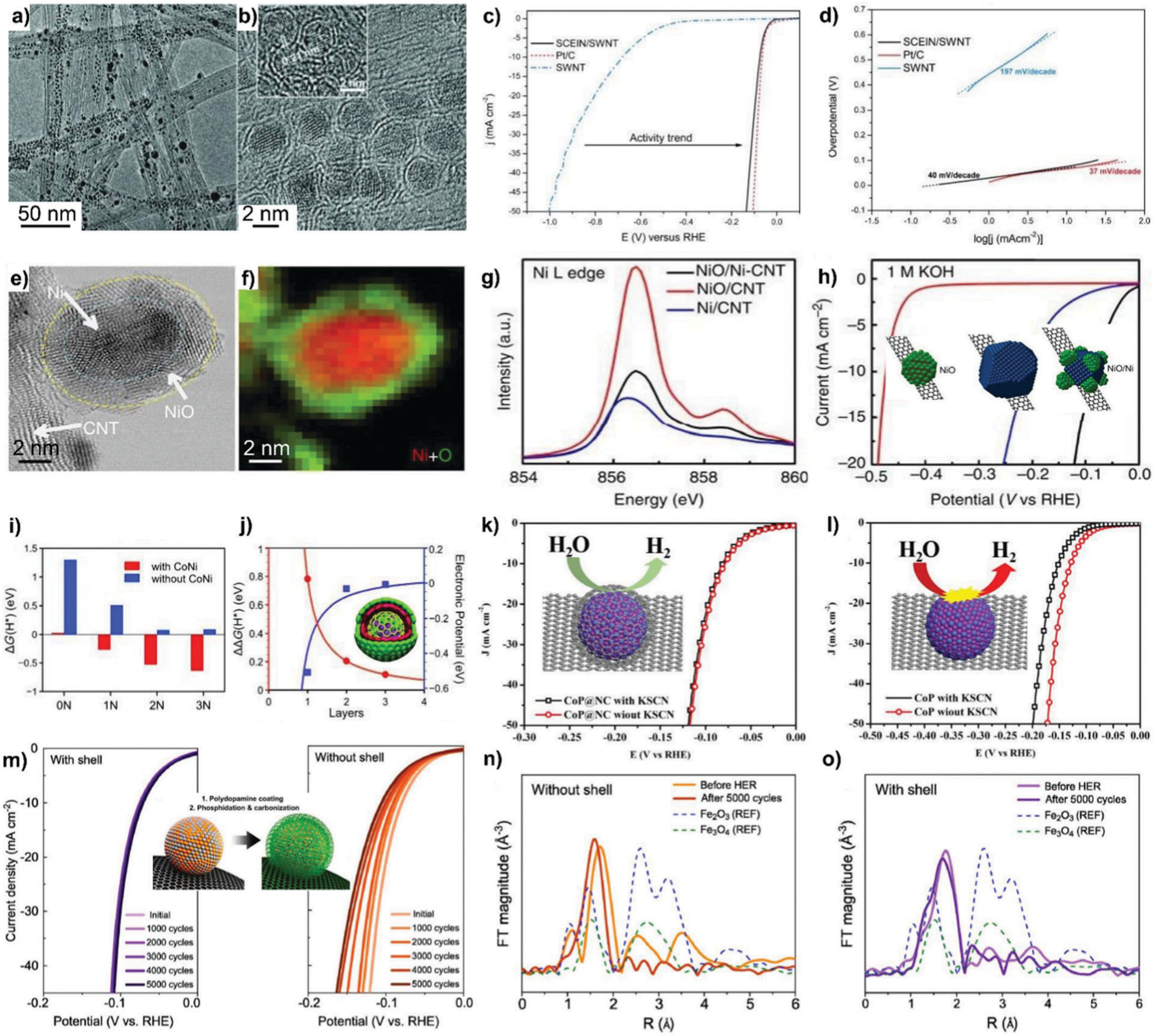

Fig. 17 (a) TEM and (b) HRTEM images of SCEIN/SWNT; the inset in (b) represents the (110) lattice plane of Fe particles in SCEINs. (c) Polarization curves at 50 mV s^{-1} in 0.5 M H_2SO_4 and (d) Tafel slopes of SWNT, SCEIN/SWNT, and Pt/C. Reproduced from ref. 348 with permission from Wiley-VCH, Copyright 2015. (e) Bright-field STEM image and (f) chemical map for Ni and O distribution of NiO/Ni-CNT. (g) Ni L edge XANES spectra and the HER linear sweep voltammetry (h) of three hybrid materials in 1.0 M KOH. Reproduced from ref. 356 with permission from Springer Nature, Copyright 2014. (i) The free energy of H adsorption ($\Delta G(H^*)$) on pure and N-doped (one, two, or three N atoms per shell) graphene shells with and without an enclosed CoNi cluster. (j) $\Delta\Delta G(H^*)$ (red line) and electronic potential (blue line) as a function of graphene layer numbers, where $\Delta\Delta G = \Delta G$ (without metal) − ΔG (with metal); inset: schematic illustration of a CoNi particle coated with three-layer graphene. Reproduced from ref. 105 with permission from Wiley-VCH, Copyright 2015. HER polarization curves of CoP@NC (k) and CoP (l) with and without the addition of KSCN in 0.5 M H_2SO_4. Reproduced from ref. 369 with permission from American Chemical Society, Copyright 2017. (m) Polarization curves of FeP NPs with (left) and without (right) carbon shell after different cycle tests. EXAFS spectra of FeP NPs without (n) and with (o) carbon shell. Reproduced from ref. 371 with permission from American Chemical Society, Copyright 2017.

loading of 0.28 mg cm^{-2} in 1.0 M KOH (Fig. 17g and h). The highly effective alkaline HER activity stemmed from the synergistic effect on the NiO/Ni interface in terms of providing the sorption sites for OH^- on NiO and facilitating H adsorption on Ni^0. It is known that Ni^0 at the NiO/Ni interface is much more active than the bulk Ni^0. Notably, the NiO/Ni heterostructure was unstable under the long-term HER condition, which was caused by the oxidation of Ni^0. The authors accordingly prepared the nanoscale Ni core being coated with the Cr_2O_3-blended NiO overlayer to display a superior stability in basic solution.[357] The addition of Cr_2O_3 could prevent the oxidation of the Ni core, thus maintaining the abundant NiO/Ni nanointerfaces for the efficient HER catalysis. In addition to metal oxides, carbon nanoshells have been deployed to enhance the long-term durability of the Ni surface for passivation or oxidation, as reported by Doan *et al.*[358] The coating of the Ni surface with a graphitic carbon layer was done by pyrolyzing the mixture of Ni^{2+}-cupferron complex in the presence of carbon support at 700 °C. Surface analysis showed the amount of Ni^0 on the carbon-coated catalyst as high as 46%, whereas no Ni^0

(but 76% of $Ni(OH)_2$) was observable on the catalyst without carbon shell embedding. The protection of the Ni^0 state from oxidation by carbon coating was evidenced from *in situ* XAS measurements.

Carbon coatings were also able to deactivate the formation of hydride on the Ni surface. Consequently, the carbon-embedded Ni catalyst featuring an optimal ratio of $Ni^0:NiO_x$ exhibited a superior HER performance. These advances demonstrate the importance of a favourable ratio between Ni^0 and NiO_x on Ni-based electrocatalysts for alkaline HER catalysis.

Layered double hydroxides (LDHs) and their derivatives are promising electrocatalysts for alkaline water splitting due to their unique electron distribution. However, the poor conductivity and insufficient active sites impede their application in alkaline HER. Recently, Wang *et al.*[144] performed surface overcoating engineering on the NiFe LDH with CeO_x by using a electrodeposition method. The enhanced alkaline HER activity in this work was credited to the facilitated H_2O adsorption on the oxygen vacancies created at the NiFe LDH/CeO_x interface. Of note, the development of carbon shell-overcoated metal oxides as electrocatalysts toward the HER catalysis is rarely investigated. The carbon shell encapsulation strategy was applied to optimize the acidic HER performance of a WO_x-based catalyst (WO_x@C/C) by means of improving electrical conductivity, increasing charge transfer rate, and optimizing hydrogen adsorption energy.[359] There are also few reports on the utility of polyoxometalate (POM)-incorporated MOF nanomaterials to fabricate metal oxide based HER electrocatalysts.[360,361] For example, Tang *et al.*[361] prepared MoO_2@PC-RGO consisting of MoO_2, P-doped nanoporous carbon (PC) and reduced graphene oxide (RGO) through the pyrolysis of the one-pot formed POM-MOFs/GO nanocomposite. For the HER in acidic solution, MoO_2@PC-RGO exhibited an onset potential of 0 mV, a Tafel slope of 41 mV dec^{-1}, and longer durability. It was described that the well-dispersed MoO_2 particles protected by the carbon shell, the P dopants derived from POM and the porous structure of MoO_2@PC-RGO synergistically led to improvement in HER performance.

Metal alloys consisting of metal atoms mixed at the nano scale can tune the HBE on active sites and result in synergistic effects which enhance their HER performance. The overcoating strategy has been applied for engineering metal alloys such as CoNi,[105] FeCo,[362] NiCu[363] and NiFe[364] with carbon nanoshells as HER electrocatalysts. By means of pyrolyzing the lamellar complex EDTA-CoNi (EDTA: ethylenediaminetetraacetate), Deng *et al.*[105] prepared uniform CoNi nanoalloys which are encapsulated within ultra-thin graphene shells with only 1–3 layers. DFT calculation results in Fig. 17i show that combining CoNi with the N-graphene shell with a varied amount of N dopants could positively tune H adsorption energy. The promotion effect on electron transfer on CoNi declines with the increasing layers of the graphene shell, as illustrated by the H adsorption difference [$\Delta\Delta G(H^*)$] of the graphene layer with or without CoNi (Fig. 17j). The effect of the thickness of the carbon shell on the HER activity was observed on the NiCu@C catalyst as well.[363] More importantly, in this case, an acceptable HER performance was achieved by a delicate control over the carbon shell thickness even without the incorporation of any dopants such as N, P, B, O and so on. These results indicate that controlling the thickness of the carbon nanoshell is an important strategy to optimize the electronic structure of the catalyst with superior HER activity.

Transition metal phosphides, carbides, chalcogenides. The application of transition metal phosphides, carbides, and chalcogenides in HER catalysis has been intensively exploited in the past decade.[327,365,366] Benefiting from the suitable hydrogen adsorption free energy and good conductivity after P incorporation, there is a body of research works that focus on developing efficient metal phosphides for the HER.[97,109,110,326] In particular, carbon nanoshell-coated CoP catalysts were demonstrated through high-temperature carbonization and phosphidation treatment on Co-based zeolitic imidazolate frameworks such as ZIF-67[119,367,368] and ZIF-9.[369] The incorporation of P in the above works is normally carried out by post-synthetic phosphidation treatment using *e.g.* NaH_2PO_2 at 200–500 °C. Impressively, Wang *et al.*[370] developed a N,P-codoped carbon shell-coated Cu_3P-based highly active HER electrocatalyst from single Cu-MOF with N- and P-containing linkers in its framework. As for the HER activity, Yang *et al.*[369] reported that CoP@NC overcoated with an ultra-thin N-doped carbon shell (2–4 layers) was better than CoP@C and CoP in both 0.5 M H_2SO_4 and 1.0 M KOH solutions. Meanwhile, only 2 mV degradation after 1000 potential cycles from 0.05 to -0.2 V_{RHE} and negligible current density loss (at 0.1 V overpotential) were detected after 24 h of continuous operation. The authors further conducted poisoning experiments using thiocyanate ions (SCN^-) to identify the active sites on CoP@NC. As shown in Fig. 17k and l, CoP has 22 mV increase of overpotential after adding SCN^-, while that of CoP@NC with a N-doped carbon nanoshell is only 5 mV, indicating that carbon atoms that are adjacent to the N dopants in the carbon shell are the active sites for HER catalysis. Similarly, after overcoating of the N,P-codoped carbon shell (derived from ZIF-67) on the CoP nanoarray, the carbon atom-adjacent heteroatoms featuring electron donor–acceptor properties could provide abundant active sites for HER catalysis.[368]

As discussed in Section 2.2, heteroatom-containing polymers and organic compounds are suitable precursors for fabricating a porous carbon shell on metal particles. In this context, Chung *et al.*[371] prepared polydopamine pyrolysis-derived carbon shell-coated FeP NPs with a diameter of 4 nm. The afforded FeP/C with a N-doped carbon shell exhibits better HER activity (71 mV overpotential at 10 mA cm^{-2}, 52 mV dec^{-1} Tafel slope) and excellent durability compared to FeP without carbon coating, a single carbon shell without Fe as well as oxidized FeO_x/C (Fig. 17m). By comparing the Fe K-edge X-ray absorption fine structure (EXAFS) before and after the durability tests, and referring to the standard data of Fe_2O_3 and Fe_3O_4 (Fig. 17n and o), the authors discovered that the first coordination shell signal of the uncoated sample slightly shifted to the oxidized Fe state after 5000 cycles, whereas that of carbon-coated FeP/C remained in the stable valence state. The above findings indicated that the carbon nanoshell could protect FeP NPs from oxidation, which was further evidenced by performing theoretical studies.

There are also reports on HER electrocatalysts based on different kinds of metal phosphides such as MoP, FeP and Cu_3P, which are derived from carbon overcoating by the pyrolysis of organic matters, along with *in situ* or post-synthetic phosphidation treatment.[107,121,372,373] Li *et al.*[107] demonstrated that embedding MoP NPs in the Mo- and P-doped carbon layer realized the formation of Mo–C and P–C bonds. The electron transport process on the prepared MoP@C was favoured to result in extremely lower overpotential and Tafel slope for the HER catalysis in acid and alkaline solutions in comparison with that of the uncoated MoP counterpart. Likewise, Zhao *et al.*[373] recently synthesized MoP NPs encapsulated within hollow-spherical-structured N-doped carbon thin layers (MoP@NCHSs) to study the synergistic effect between MoP NPs and N dopants for enhancing HER performance. In this work, the N content and configurations were detailed from K-edge XANES and N 1s XPS spectra. The higher HER activity in alkaline solution was proposed to be originated from the large pyridinic-N ratio on MoP@NCHSs-900 which was pyrolyzed at 900 °C. Pyridinic-N–Mo was the active site for HER, as revealed by performing pyridinic N poisoning experiments and DFT calculations. In other words, pyridinic-N was effective in inhibiting the strong adsorption of OH*, and the pyridinic-N–Mo interactions can weaken the adsorption of H on Mo by electron transfer.

Carbon matrix-embedded transition metal carbides such as Mo_2C/G-NCS,[374] MoC_x@C,[375] β-Mo_2C@C,[376] WC@C,[129] W_2C@WC_{1-x}@C,[377] and W/W_2C@NPC[378] are also under extensive investigations for HER applications, owing to the features of good conductivity and excellent thermal and electrical stability against sintering. Similar to metal phosphides noted above, heteroatoms such as N and P elements doped in carbon shells can activate the adjacent carbon atoms to be the active sites on metal carbides for the catalytic generation of H_2.[111,379–382] Moreover, the incorporation of transition metal moieties (such as Fe, Co, Ni) at the atomic scale into metal carbide based HER electrocatalysts has been demonstrated to be a rewarding strategy for achieving the manifestation of synergistic effects.[116,127,383,384] In addition to the capability of promoting the formation of a carbon nanoshell and the high dispersion of metal carbide particles during carbonization, the incorporated transition metals could modulate the surface electronic structure of the catalyst to affect H binding on the active sites and thus are responsible for the favourable HER performance.

Nanomaterials (especially those derived from MOFs) featuring hollow structures could maximize the exposure of active sites and facilitate the mass transfer kinetics for efficient catalysis. Nevertheless, it is challenging in most cases to fabricate such catalysts because of the easy collapse or destruction of the structure of applied precursors during the high-temperature pyrolysis. Impressively, surface overcoating engineering could help in architecturing hollow-structured and robust molybdenum based carbides for HER catalysis, as demonstrated by Xu *et al.*[385] Prior to pyrolytic treatment, they overcoated the POM-MOF (Ni) precursor with a thin layer of carbon nitride polymer by the self-polymerization reaction of hexamethylenetetramine in ethanol solution dispersed with hollow-structured POM-MOF (Ni) at 170 °C. A totally destroyed morphology with severe metal particle agglomeration was observed after the direct annealing of the POM-MOF (Ni) precursor at 800 °C. On the other hand, overcoating with the carbon nitride polymer could efficiently avoid the collapse of hollow POM-MOF precursors and prevent metal particles from coalescence or detachment during the process of carbonization. As a result, the carbon layer-coated hollow-structured molybdenum carbide together with the Ni-MOFs-derived Ni nanoparticle made the catalyst exhibit remarkable HER activity and long-term durability in alkaline solution.

Transition metal chalcogenides are also garnering research attention for the HER.[386,387] It was reported that overcoating the carbon shell onto MoS_2 was profitable for conductivity improvement, mass transfer dynamics and protection of the MoS_2 nanosphere from collapse and stacking.[388] Similar to the pyridinic-N–Mo sites formed on MoP@NCHSs-900,[373] pyridinic-N sites on N-doped carbon coated $NiSe_2$ nano-octahedra ($NiSe_2$@NC) could determine the corresponding HER activity which showed a linear correlation with the content of pyridinic-N.[389] For the preparation of $NiSe_2$@NC, mixed-linker Ni-MOFs consisting of O-coordinating anionic carboxylate linkers and N-coordinating neutral ligands appeared to be good candidates for selective selenization. After a deliberate control over the content and configuration of N in the carbon nanoshell by using different N-ligands, $NiSe_2$@NC-PZ (PZ: pyrazine), in particular, exhibited a lower overpotential of 162 mV at 10 mA cm^{-2} and Tafel slope (88 mV dec^{-1}) in alkaline media than other $NiSe_2$@NC hybrids.

To briefly conclude, facile catalyst engineering *via* the introduction of foreign overcoatings on metal based catalysts is valuable for tackling the performance degradation. Non-precious metal based electrocatalysts have been fabricated as the favourable alternatives to precious metal counterparts for the HER catalysis. To our delight, carbon coating engineering is most widely exploited for enhancing the intrinsic activity of metal catalysts toward the HER, as discussed above based on the existing literature. The heteroatom dopants in the carbon nanoshell can positively modify H adsorption free energy with a nearly zero value to potentially optimize the electronic structure of the metal and the process of H formation/binding and thus boosting the HER efficiencies in both acid and alkaline environment. For comparison, representative surface overcoating-derived electrocatalysts based on precious and non-precious metals for efficient HER catalysis in both acid[107,233,340,342,348,361,363,369,378,381] and alkaline solutions[107,108,124,342,343,374,375,378,389] are summarized in Fig. 18.

4.3 Overcoated bifunctional electrocatalysts for overall water splitting

Electrochemical overall splitting of water powered by renewable energy appears promising for pure H_2 and O_2 production *via* the HER and OER. Owing to the sluggish kinetics of OER and the high demand on catalyst stability, developing high-efficiency

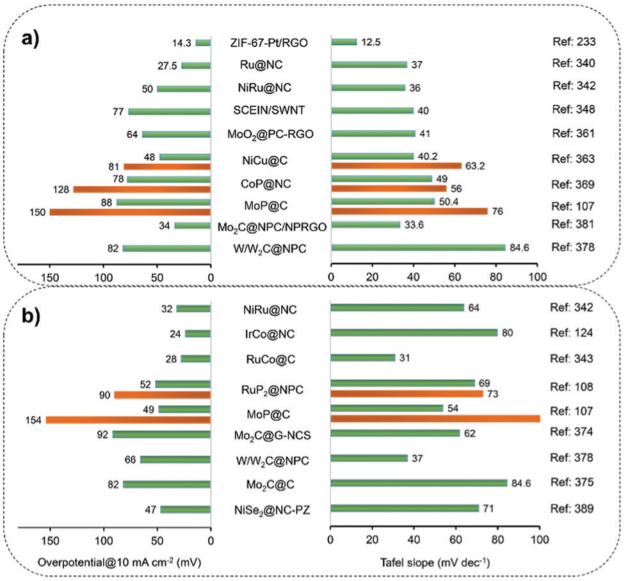

Fig. 18 Comparison of the reported HER electrocatalysts in terms of the required overpotential to reach a current density of 10 mA cm^{-2} and Tafel slope in (a) 0.5 M H_2SO_4 and (b) 1.0 M KOH electrolytes. The electrochemical parameters for some of the corresponding uncoated catalysts are also plotted (orange color).

bifunctional overall water splitting electrocatalysts in all pH range is practically meaningful and imperative. Pt/C and RuO_x or IrO_x are the benchmark catalysts for HER and OER, respectively. Recently, cost-effective water splitting electrocatalysts with satisfactory performance are becoming desirable. Some specially designed catalysts have already displayed similar or even better performance than that found with Pt/C‖RuO_2 and/or Pt/C‖IrO_2 counterparts.

The overpotential (the difference value between the required potential and the thermodynamic potential (1.23 V, 25 °C)) for OER/HER and the voltage needed to reach a certain current density (10 mA cm^{-2}) are the parameters that are generally used to evaluate the overall water splitting performance of bifunctional OER/HER electrocatalysts.

In the development of precious metal-based water splitting electrocatalysts, alloying treatment and/or constructing core–shell nanostructures with abundant 3d transition metals has been demonstrated to result in a positively perturbed electronic structure of the metal for efficient electrocatalysis. There are several works that focus on carbon nanoshell-encapsulated precious metal electrocatalysts for overall water splitting.[390–392] For example, Li *et al.*[391] prepared Co@Ir core–shell NPs encapsulated in N-doped porous carbon through the galvanic replacement of $IrCl_3$ with the ZIF-67-derived Co/NC nanomaterial in an aqueous solution for 24 h, followed by centrifugation and drying step. The formation of a core–shell structure with a shell of thin layer of Ir on Co@Ir could promote the exposed proportion of Ir and further improve its utilization efficiency. Electrical measurements on Co@Ir/NC-10% (10% is the initial mass amount of Ir) displayed the best performance in terms of superior OER activity than IrO_2 and close HER activity to Pt/C, along with excellent long-term durability. The authors evaluated further the practical overall water splitting performance of Co@Ir/NC-10% in basic solution by assembling the catalyst onto carbon fiber paper, and showed potential application under the applied 1.7 V_{RHE}. Following a similar galvanic replacement strategy, Ni@Ru core–shell NPs overcoated with a 2–5 nm-thin graphitic carbon nanoshell displayed a potential of 1.612 V at 10 mA cm^{-2} for overall water splitting in alkaline solution, outperforming the reference Pt/C and RuO_2 catalysts.[392]

Combining the merits of the carbon matrix with non-precious metal species by using various overcoating methodologies, along with the phosphorization or sulfurization treatment, promises cost-effective electrocatalysts based on abundant metals for efficient overall water splitting reactions. Recently, boosting research activities have been dedicated to the development of surface overcoating-derived bifunctional overall water splitting electrocatalysts, including metallic transition metals and alloys,[117,324,345,393–398] transition metal (hydro)oxides,[144,399–402] metal phosphides,[130,131,327,403–406] metal carbides[407–409] and metal chalcogenides.[101,410,411] Some typical examples of these works are presented below.

Li *et al.*[399] developed N-doped carbon-coated Co–Mn oxide (CoMnO@CN) by utilizing a solvent evaporation-induced self-assembly method (Fig. 19a). After the slow evaporation of solvent and the calcination step, 5 nm-sized CoMnO particles were assembled into a highly ordered superlattice structure with the overcoating of a 2 nm-thin amorphous carbon layer. The obtained CoMnO@CN exhibited the highest OER current density (308 mA cm^{-2}) at 1.65 V_{RHE} in alkaline solution compared with structure disordered CoMnO@CN and the catalyst without N doping (Fig. 19b and c).The HER performance of CoMnO@CN superlattices also surpassed that of most earth-abundant metal based HER catalysts (Fig. 19d). According to the authors, CoMnO NPs in the CoMnO@CN catalyst favour the OER, while the outer carbon shells not only provide additional active sites for HER, but could also synergistically protect the inner CoMnO NPs from aggregation or dissolution during the electrocatalytic processes. When working as both the electrodes in an alkaline water electrolyzer, CoMnO@CN superlattices realized 54 and 108 mA cm^{-2} current density with an applied potential of 1.7 V and 1.8 V, respectively. High stability was also achieved after 10 h operation with an applied potential of 1.5 V (Fig. 19e).

Note that, in addition to the surface overcoating strategy, there are other strategies being developed for improving the performance of metal based catalysts toward the electrochemical water splitting, such as doping, defect engineering and designing unique nanoarchitectonics and so on.[412,413] A number of 3d transition metal-based nanomaterials including metal oxides, nitrides, and sulfides have been and are being rationally designed as good candidates for overall water splitting reactions. For example, Zhang *et al.*[414] designed $NiMoO_{4-x}$/MoO_2 by combining oxygen vacancies and nanointerfaces between $NiMoO_{4-x}$ and MoO_2 as the efficient water splitting catalyst. In this case, a voltage of 1.56 V was required for a current density of 10 mA cm^{-2}. Porous MoO_2 nanosheets on nickel foam were developed by the group of

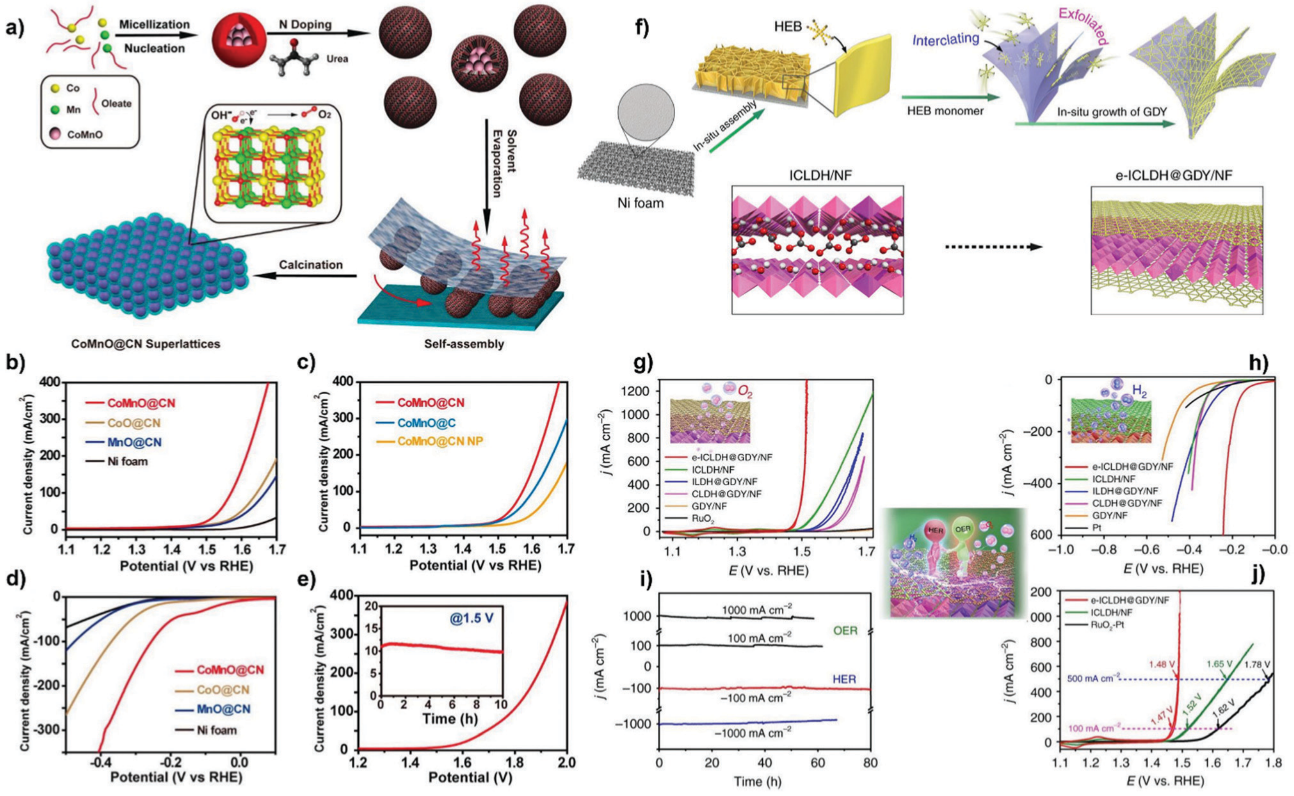

Fig. 19 (a) Synthetic procedures for the CoMnO@CN superlattice structure. (b and c) OER and (d) HER LSV curves of CoMnO@CN compared with other control samples in a 1.0 M KOH electrolyte in a 3-electrode configuration. (e) Overall water splitting measurements of CoMnO@CN in a two-electrode configuration. The inset represents the chronoamperometric curve at an applied potential of 1.5 V across the electrodes. Reproduced from ref. 399 with permission from American Chemical Society, Copyright 2015. (f) Schematic of the synthesis of e-ICLDH@GDY/NF structures. (g) OER and (h) HER polarization curves of as-synthesized different samples. (i) Chronopotentiometric curves of e-ICLDH@GDY/NF for OER and HER at 100 and 1000 mA cm^{-2}. (j) The activities of pristine ICLDH/NF and e-ICLDH@GDY/NF towards the overall water splitting reaction with iR-correction. Reproduced from ref. 421 with permission from Springer Nature, Copyright 2018.

Cui as the active and stable bifunctional overall water splitting catalyst, showing a cell voltage of 1.53 V for a current density of 10 mA cm^{-2} together with at least 24 h of durability.[415] Li *et al.*[416] reported that 3D self-supported Fe-doped Ni_2P nanosheet arrays showed promising overall water splitting performance with 1.49 V of cell voltage at 10 mA cm^{-2} and excellent stability at 1.7 V. Recently, Yu *et al.*[417] reported 3D core–shell NiMoN@NiFeN supported on porous Ni foam for the alkaline seawater splitting. When working as the bifunctional electrode catalyst at 60 °C, NiMoN@NiFeN achieved a current density of 500 and 1000 mA cm^{-2} at a record voltage of 1.608 and 1.709 V, respectively. In addition, a cell voltage as low as 1.43 V at 10 mA cm^{-2} and excellent long-term durability (100 h@100 mA cm^{-2}) were achieved on the NiCoMo–OH catalyst, which was prepared by Hao *et al.*[418] through a chloride corrosion method. Moreover, a $NiMoO_x$/NiMoS heterostructure was engineered in the work of Zhai *et al.*[419] to accelerate water splitting kinetics, which required a voltage of 1.60 and 1.66 V respectively to reach a current density of 500 and 1000 mA cm^{-2} as well demonstrated excellent long-term durability.

The overall water splitting cell voltage and durability of overcoated materials developed as bifunctional water splitting electrocatalysts in 1.0 M KOH solution are summarized in Table 2. It is worth stressing that surface overcoating engineering can be regarded as one of the promising strategies for improving catalyst's overall water splitting performance. Typically, coupling carbon with ultra-thin Co-doped NiO ($Ni_{0.82}Co_{0.18}O$) on Ni foam enabled to feature unique 3D configuration and abundant exposed active sites, ensuring an ultralow voltage of 1.42 V at a current density of 10 mA cm^{-2} when catalyzing the overall water splitting.[400] Recently, Qian *et al.*[420] reported Ni NPs encapsulated with ultra-thin N-doped graphene coupled with MoO_2 nanosheets for catalyzing the water splitting at large current density. In detail, the prepared Ni@C-MoO_2/NF electrode exhibited a voltage of 1.54, 1.61 and 1.67 V at 10, 50 and 100 mA cm^{-2}, respectively. Impressively, it can be held for over 196 h at 1000 mA cm^{-2} in 1.0 M KOH. These superior performances were ascribed to the following factors: (i) the electron transfer between Ni NPs and N atoms from the carbon shell optimized the surface electronic structure, thus enhancing the OER/HER activity; (ii) the Ni@C structure was prone to have a more efficient electron transfer and faster faradaic process on the electrode–electrolyte interface; and (iii) the self-supported MoO_2 nanosheets on Ni foam improved the utilization efficiency of active sites and facilitated the mass

Table 2 Comparison of cell voltage and durability of overcoated electrocatalysts for overall water splitting

Electrocatalyst	Cell voltage@10 mA cm^{-2} [V]	Durability [h]	Substrate	Ref.
$Fe_{1.0}Co_{1.1}Ni_{1.4}$-NC	1.52	20 (@10 mA cm^{-2})	Carbon cloth	117
Co@N-CS/N-HCP	1.545	24 (@30 mA cm^{-2})	Carbon cloth	397
Ni@NC	1.60	50 (@1.62 V)	Ni foam	345
Ni@C-MoO_2/NF	1.54	196 (@1000 mA cm^{-2})	Ni foam	420
Cu@C	1.645	24 (@10 mA cm^{-2})	Ni foam	398
NiFe LDH/CeO_x	1.51	10 (@10 mA cm^{-2})	Ni foam	144
e-ICLDH@GDY/NF	1.43	60 (@100 mA cm^{-2})	Ni foam	421
FeCH@GDY/NF	1.49	25 (@10 mA cm^{-2})	Ni foam	422
CoMnO@CN	1.50	10 (@10 mA cm^{-2})	Ni foam	399
$Ni_{0.82}Co_{0.18}O$@C	1.42	20 (@10 mA cm^{-2})	Ni foam	400
Ni-$NiFe_2O_4$@C	1.57	20 (@20 mA cm^{-2})	Carbon cloth	401
FeNiP/PG	1.58	10 (@10 mA cm^{-2})	Carbon cloth	130
NC-$NiFeO_x$@NiFe-P	1.59	20 (@10 mA cm^{-2})	Ni foam	131
$NiFeO_x$@NiFe-P	1.81	—	Ni foam	131
C@Ni_8P_3	1.65	25 (@10 mA cm^{-2})	Ni foam	327
Ni_8P_3	1.79	—	Ni foam	327
CoP@C@rGo	1.50	24 (@10 mA cm^{-2})	Carbon paper	406
Co_9S_8@NOSC-900	1.60	10 (@50 mA cm^{-2})	Ni foam	101
NCT-$NiCo_2S_4$	1.60	15 (@10 mA cm^{-2})	Ni foam	411

transfer process during the reaction. Moreover, when employed as both anode and cathode catalysts in a water electrolyzer, C@Ni_8P_3 (the Ni_8P_3 nanosheets surface-coated with carbon shell) can deliver a current density of 10 mA cm^{-2} at a lower cell voltage (1.65 V) than Ni_8P_3 without carbon coating with a voltage of 1.79 V in 1.0 M KOH.[327] C@Ni_8P_3 also exhibited an excellent long-term durability performance, whereas Ni_8P_3 was found to be considerably degraded.

In another study by Hui *et al.*,[421] the synthesis of graphdiyne-wrapped iron-cobalt LDH nanosheets (CoFe-LDH) with sandwiched structure grown on Ni foam and their application as a bifunctional overall water splitting electrode were reported. In this case, graphdiyne (GDY), a 2D monolayer of sp/sp^2-hybridized carbon material, was introduced into the interlayer of CoFe LDH by using hexaethynylbenzene monomers through *in situ* polymerization (Fig. 19f). The uniform growth of the GDY film on the CoFe LDH surface with intimate contact induced the complete exfoliation of bulk LDH into ultrathin LDH nanosheets being wrapped with GDY on both sides of surfaces. Notably, due to its high electronic conductivity and the richness in charged carbon atoms, the GDY layer was found to play a critical role in enhancing the catalytic performance of CoFe LDH for the overall water splitting. The OER activity test on the as-fabricated catalyst indicated a low overpotential of 216, 249, and 278 mV to deliver 10, 100, and 1000 mA cm^{-2} current densities (Fig. 19g). To achieve such current densities, an overpotential of 43, 215 and 256 mV was respectively required for the HER catalysis (Fig. 19h). The excellent OER performance was mainly ascribed to Fe doping and GDY incorporation which induced enhanced charge transfer from LDH to GDY. On the other hand, the origin of the enhancement of HER activity was enabled by the facilitated electron transport and the abundant active sites after GDY layer wrapping. The superior durability (Fig. 19i) of e-LDH@GDY/NF to the OER and HER was attributed to the protective aid from the GDY overlayer. The performance of GDY-wrapped CoFe LDH for overall water splitting was evaluated in 1.0 M KOH in a two electrode configuration. As shown in Fig. 19j, 1.43, 1.46 and 1.49 V was respectively measured to achieve 10, 100 and 1000 mA cm^{-2} current densities. The electrolyzer displayed an enhanced long-term stability (over 60 h) at the current density of 100 mA cm^{-2} under a constant voltage of 1.56 V. A faradaic efficiency of 97.40% for the O_2 evolution was achieved. The authors also revealed the decisive role of the GDY overlayer in improving the electrocatalytic efficiencies of ultrathin GDY-wrapped iron carbonate hydroxide nanosheets for the overall water splitting in WECs.[422]

The above achieved progress indicates that the encapsulated metal catalysts constructed based on surface overcoating engineering are a kind of advanced architecture for catalyzing high-performance electrochemical reactions. Accordingly, both precious and non-precious metal based electrocatalysts designed and optimized by surface overcoating engineering have been validated to be efficient for application in WECs. By controlling the synthetic aspects such as the elaborate selection of overcoating materials, pyrolysis conditions and heteroatom dopants, the chemical composition, spatial structural properties of electrocatalysts as well as the nature of active sites can be rationally optimized to result in outstanding overall water splitting performance.

5. Summary and outlook

This review summarizes a variety of surface overcoating methodologies implemented for engineering high-performance electrocatalysts, which are potentially applied for sustainable energy-related transformations. Substantial advances in nanoscience and material chemistry have benefited the fabrication of metal nanoparticles and the modification of catalyst supports by the utility of overcoating materials, including organic matters, inorganic carbon nanoshells and metal oxides. Surface-engineered nanostructures featuring the promoted synergistic effect of metal sites and foreign coatings can remarkably enhance the process of electrocatalysis. Despite the research progress, effectiveness and structure–catalytic function of surface overcoating-derived electrocatalysts as discussed in this review, the development of electrochemically highly active and durable nanocatalysts is still ongoing to achieve their large-scale distributions in renewable energy conversion and storage devices. Therefore, the identified opportunities and perspectives associated with the surface overcoating engineering for designing optimal heterogeneous catalysts should be considered and are detailed below.

(1) Approximate selection of overcoating materials for precise design and optimization of more advanced electrocatalysts. In addition to the manifestation of steric hindrance effects, surface overcoatings enable one to dramatically modulate the electronic surface structure of metal entities and tune the adsorption behaviour of reactants and key intermediate catalytic species; consequently, electrocatalytic performance varies with the overcoating materials introduced. It is worth noting that catalyst electrocatalytic activity, which can be descripted by the binding energy states of surface intermediates (*i.e.* H*, OH*, OOH*), follows the intrinsic catalytic behaviour of metals, the pH of electrolytes, and the operating environment (such as the cell performance tests where electrocatalysts are fabricated into MEAs). Therefore, the specific selection of surface overcoating materials should be compatible with specifically investigated applications in the areas related to electrochemical energy storage and conversion. Currently, organic capping agents/polymers, inorganic carbon nanoshells and metal oxides have been successfully employed as the favourable surface overcoating materials. With the blooming synthetic development of metal nanostructures as well as support materials, the exploitation of innovative overcoating materials such as MOFs and/or MOF-derivatives becomes increasingly crucial for the fabrication of multifunctional nanocomposites with superior efficacy when applied in PEFCs, WECs and beyond. We refer the readers to a recent review, which describes the synergistic advantages of MOF coatings in broad applications.[423]

(2) In-depth understanding of the interfacial mechanism at different scales. Electrical coupling, regulating the structure and mobility of metal NPs, and controlling surface adsorption kinetics are among the most rewarding benefits from catalyst overcoating engineering. As noted, the functional groups of N-containing organic compounds serve as the coordination sites for controllable synthesis of metal entities with desired phase compositions and morphological integrities. Heteroatom-doped carbon nanoshells derived from the carbonization of organic composites could afford a plethora of functionalities, including the modulation of the binding energy states of reactants and intermediate reactive species and the limitation posed on the probability of metal nanoparticle coalescence and sintering. In addition, in many cases the strong metal–metal oxide interaction is a critical factor as well for enhancing electrocatalytic properties *via* specific modification pathways. Despite the widely accepted role of the carbon nanoshell in stabilizing metal NPs, there is still a dearth of in-depth studies on the carbonization of organic matters and the concurrent overcoating process on the surface of metal entities during the process of high-temperature pyrolysis. Moreover, an improved mechanistic understanding for enhancing electrocatalytic properties and the synergistic effect between metal particles and overcoatings is still imperative. Intensive *in situ* and *operando* characterization technologies such as XRD, X-ray absorption (XPS, XANES, EXAFS), TEM/STEM and infrared spectroscopy (IR) in conjunction with theoretical calculations could enable detailed structural and fundamental observations on the genuine active sites and their evolution processes under the real-time synthetic and operating conditions.

(3) Broadening the application of the surface overcoating strategy. Besides the emerging applications in PEFCs (involving HOR, ORR, alcohol oxidation reactions) and WECs (comprising OER, HER, overall water splitting) as featured in this review article, the surface overcoating strategy also shows increasing potential for fabricating advanced nanomaterials, which are already applied in thermal-catalytic reactions,[188,424–428] redox flow batteries,[429,430] metal–air batteries,[431,432] solid oxide fuel cells,[433–435] lithium-ion batteries or capacitors,[69,436,437] ammonia electrosynthesis,[438,439] CO_2 electrocatalytic reduction,[440–442] and biotechnology.[443,444] One could obtain highly dispersed fine metal nanoparticles with the aid of organic or inorganic overlayers after annealing treatment. As appealing in the thermal catalysis field, the carbon nanoshell derived from organic capping agents or polymers has been employed as a sacrificial protector to inhibit metal particles from migration/coalescence and sintering. A simple removal of carbon species by post-oxidation treatment enables the formation of surface clean and ultra-stable Co, Mo, Au, Pd, and Pt catalysts.[445–448] One can also achieve the control of catalytic selectivity in gas-phase thermal reactions by the utility of the reactant sieve property of the carbon overlayer.[449] As for manipulating catalytic activity, after overcoating reducible metal oxides onto Pt/SiO_2, CO oxidation activity followed the trend $TiO_2 > CeO_2 > Pt/SiO_2 > Ta_2O_5 \approx Nb_2O_5$.[450] It is assigned to the formation of a metal–metal oxide interface, which is also beneficial for Pt with high resistance towards sintering under high temperature. In another report, the $Cu–ZrO_2$ interface formed on ZrO_2-overcoated Cu/SiO_2 was efficient for methanol synthesis from CO_2 hydrogenation.[451] Moreover, dopamine polymerization-derived N-doped carbon shell-coated SnO_2,[452] $SnFe_2O_4$,[453] and silicon[454] have already exhibited excellent rate capability and long-term stability in lithium-ion batteries. Intriguingly, the implementation of the surface overcoating strategy is holding great potential for engineering of optimal heterogeneous catalysts with a broad scope of applications.

Suitably engineered electrocatalysts play crucial roles in the practical applications of electrocatalysis-based energy conversion and storage devices. Great progress in the rational design of nanomaterials based on the surface overcoating strategy has been made for the assurance of electrochemical transformations with high efficiencies. We hope that this review can be a useful reference and serves to provide instructive inspirations for catalysis research communities. Surface overcoating engineering will continue being one of the crucially developed strategies for the design, fabrication and optimization of advanced heterogeneous catalysts.

Conflicts of interest

There are no conflicts to declare.

Acknowledgements

This project has received funding from the European Union's Horizon 2020 research and innovation programme under grant agreement no. 875524. This work does not reflect the official opinion of the European Union and responsibility for the information lies entirely with the authors.

References

1 J. Zecevic, G. Vanbutsele, K. P. de Jong and J. A. Martens, *Nature*, 2015, **528**, 245–248.

2 M. Liu, R. Zhang and W. Chen, *Chem. Rev.*, 2014, **114**, 5117–5160.

3 L. He, F. Weniger, H. Neumann and M. Beller, *Angew. Chem., Int. Ed.*, 2016, **55**, 12582–12594.

4 H. You, S. Yang, B. Ding and H. Yang, *Chem. Soc. Rev.*, 2013, **42**, 2880–2904.

5 Y. Dai, P. Lu, Z. Cao, C. T. Campbell and Y. Xia, *Chem. Soc. Rev.*, 2018, **47**, 4314–4331.

6 Y.-J. Wang, N. Zhao, B. Fang, H. Li, X. T. Bi and H. Wang, *Chem. Rev.*, 2015, **115**, 3433–3467.

7 E. D. Goodman, J. A. Schwalbe and M. Cargnello, *ACS Catal.*, 2017, **7**, 7156–7173.

8 T. W. Hansen, A. T. DeLaRiva, S. R. Challa and A. K. Datye, *Acc. Chem. Res.*, 2013, **46**, 1720–1730.

9 Y. Nie, L. Li and Z. Wei, *Chem. Soc. Rev.*, 2015, **44**, 2168–2201.

10 X. X. Wang, M. T. Swihart and G. Wu, *Nat. Catal.*, 2019, **2**, 578–589.

11 Z. W. Seh, J. Kibsgaard, C. F. Dickens, I. Chorkendorff, J. K. Nørskov and T. F. Jaramillo, *Science*, 2017, **355**, eaad4998.

12 M. K. Debe, *Nature*, 2012, **486**, 43–51.

13 X. Tian, P. Zhao and W. Sheng, *Adv. Mater.*, 2019, **31**, 1808066.

14 Y. Cong, B. Yi and Y. Song, *Nano Energy*, 2018, **44**, 288–303.

15 R. Borup, J. Meyers, B. Pivovar, Y. S. Kim, R. Mukundan, N. Garland, D. Myers, M. Wilson, F. Garzon, D. Wood, P. Zelenay, K. More, K. Stroh, T. Zawodzinski, J. Boncella, J. E. McGrath, M. Inaba, K. Miyatake, M. Hori, K. Ota, Z. Ogumi, S. Miyata, A. Nishikata, Z. Siroma, Y. Uchimoto, K. Yasuda, K.-I. Kimijima and N. Iwashita, *Chem. Rev.*, 2007, **107**, 3904–3951.

16 K. Ehelebe, J. Knöppel, M. Bierling, B. Mayerhöfer, T. Böhm, N. Kulyk, S. Thiele, K. J. J. Mayrhofer and S. Cherevko, *Angew. Chem., Int. Ed.*, 2021, **60**, 8882–8888.

17 X. Tian, X. F. Lu, B. Y. Xia and X. W. Lou, *Joule*, 2020, **4**, 45–68.

18 K. Singh, E. B. Tetteh, H.-Y. Lee, T.-H. Kang and J.-S. Yu, *ACS Catal.*, 2019, **9**, 8622–8645.

19 J. Song, C. Wei, Z.-F. Huang, C. Liu, L. Zeng, X. Wang and Z. J. Xu, *Chem. Soc. Rev.*, 2020, **49**, 2196–2214.

20 S. Mukerjee, S. Srinivasan, M. P. Soriaga and J. McBreen, *J. Electrochem. Soc.*, 1995, **142**, 1409–1422.

21 I. E. L. Stephens, A. S. Bondarenko, U. Grønbjerg, J. Rossmeisl and I. Chorkendorff, *Energy Environ. Sci.*, 2012, **5**, 6744–6762.

22 Y. Kang, J. B. Pyo, X. Ye, T. R. Gordon and C. B. Murray, *ACS Nano*, 2012, **6**, 5642–5647.

23 X. Huang, Z. Zhao, L. Cao, Y. Chen, E. Zhu, Z. Lin, M. Li, A. Yan, A. Zettl, Y. M. Wang, X. Duan, T. Mueller and Y. Huang, *Science*, 2015, **348**, 1230–1234.

24 S. T. Hunt, M. Milina, A. C. Alba-Rubio, C. H. Hendon, J. A. Dumesic and Y. Román-Leshkov, *Science*, 2016, **352**, 974–978.

25 J. Li, Z. Xi, Y.-T. Pan, J. S. Spendelow, P. N. Duchesne, D. Su, Q. Li, C. Yu, Z. Yin, B. Shen, Y. S. Kim, P. Zhang and S. Sun, *J. Am. Chem. Soc.*, 2018, **140**, 2926–2932.

26 Z. Xia and S. Guo, *Chem. Soc. Rev.*, 2019, **48**, 3265–3278.

27 P. Strasser, S. Koh, T. Anniyev, J. Greeley, K. More, C. Yu, Z. Liu, S. Kaya, D. Nordlund, H. Ogasawara, M. F. Toney and A. Nilsson, *Nat. Chem.*, 2010, **2**, 454–460.

28 X. Wang, S.-I. Choi, L. T. Roling, M. Luo, C. Ma, L. Zhang, M. Chi, J. Liu, Z. Xie, J. A. Herron, M. Mavrikakis and Y. Xia, *Nat. Commun.*, 2015, **6**, 7594.

29 A. Garg, M. Milina, M. Ball, D. Zanchet, S. T. Hunt, J. A. Dumesic and Y. Román-Leshkov, *Angew. Chem., Int. Ed.*, 2017, **56**, 8828–8833.

30 D. Göhl, A. Garg, P. Paciok, K. J. J. Mayrhofer, M. Heggen, Y. Shao-Horn, R. E. Dunin-Borkowski, Y. Román-Leshkov and M. Ledendecker, *Nat. Mater.*, 2020, **19**, 287–291.

31 Y. J. Sa, D.-J. Seo, J. Woo, J. T. Lim, J. Y. Cheon, S. Y. Yang, J. M. Lee, D. Kang, T. J. Shin, H. S. Shin, H. Y. Jeong, C. S. Kim, M. G. Kim, T.-Y. Kim and S. H. Joo, *J. Am. Chem. Soc.*, 2016, **138**, 15046–15056.

32 Z.-Z. Jiang, Z.-B. Wang, D.-M. Gu and E. S. Smotkin, *Chem. Commun.*, 2010, **46**, 6998–7000.

33 H. Li, C. Chen, D. Yan, Y. Wang, R. Chen, Y. Zou and S. Wang, *J. Mater. Chem. A*, 2019, **7**, 23432–23450.

34 Q. Lenne, Y. R. Leroux and C. Lagrost, *ChemElectroChem*, 2020, **7**, 2345–2363.

35 C. Gao, F. Lyu and Y. Yin, *Chem. Rev.*, 2021, **121**, 834–881.

36 Y. Nie and Z. Wei, *Prog. Nat. Sci.*, 2020, **30**, 796–806.

37 M. Sharma, N. Jung and S. J. Yoo, *Chem. Mater.*, 2018, **30**, 2–24.

38 I. Chang, S. Ji, J. Park, M. H. Lee and S. W. Cha, *Adv. Energy Mater.*, 2015, **5**, 1402251.

39 S. Hong, S. Oh, H. J. Kim, Y. Lim, J. An and Y.-B. Kim, *J. Electrochem. Soc.*, 2017, **164**, F1301–F1306.

40 J. W. Shin, S. Oh, S. Lee, J.-G. Yu, J. Park, D. Go, B. C. Yang, H. J. Kim and J. An, *ACS Appl. Mater. Interfaces*, 2019, **11**, 46651–46657.

41 S. H. Joo, J. Y. Park, C.-K. Tsung, Y. Yamada, P. Yang and G. A. Somorjai, *Nat. Mater.*, 2009, **8**, 126–131.

42 Y. Y. J. Tong, *Chem. Soc. Rev.*, 2012, **41**, 8195–8209.

43 K. Miyabayashi, H. Nishihara and M. Miyake, *Langmuir*, 2014, **30**, 2936–2942.

44 Y.-H. Chung, S. J. Kim, D. Y. Chung, H. Y. Park, Y.-E. Sung, S. J. Yoo and J. H. Jang, *Chem. Commun.*, 2015, **51**, 2968–2971.

45 F. Mirkhalaf, J. Paprotny and D. J. Schiffrin, *J. Am. Chem. Soc.*, 2006, **128**, 7400–7401.

46 Z.-Y. Zhou, X. Kang, Y. Song and S. Chen, *Chem. Commun.*, 2011, **47**, 6075–6077.

47 Z.-Y. Zhou, J. Ren, X. Kang, Y. Song, S.-G. Sun and S. Chen, *Phys. Chem. Chem. Phys.*, 2012, **14**, 1412–1417.

48 A. M. Hofstead-Duffy, D.-J. Chen and Y. Y. J. Tong, *Electrochim. Acta*, 2012, **82**, 543–549.

49 W. Liu and H. Wang, *Surf. Sci.*, 2016, **648**, 120–125.

50 J. E. Newton, J. A. Preece, N. V. Rees and S. L. Horswell, *Phys. Chem. Chem. Phys.*, 2014, **16**, 11435–11446.

51 Q. Xue, J. Bai, C. Han, P. Chen, J.-X. Jiang and Y. Chen, *ACS Catal.*, 2018, **8**, 11287–11295.

52 G. Fu, K. Wu, X. Jiang, L. Tao, Y. Chen, J. Lin, Y. Zhou, S. Wei, Y. Tang, T. Lu and X. Xia, *Phys. Chem. Chem. Phys.*, 2013, **15**, 3793–3802.

53 G. Fu, K. Wu, J. Lin, Y. Tang, Y. Chen, Y. Zhou and T. Lu, *J. Phys. Chem. C*, 2013, **117**, 9826–9834.

54 G. Fu, X. Jiang, M. Gong, Y. Chen, Y. Tang, J. Lin and T. Lu, *Nanoscale*, 2014, **6**, 8226–8234.

55 F.-M. Li, X.-Q. Gao, S.-N. Li, Y. Chen and J.-M. Lee, *NPG Asia Mater.*, 2015, **7**, e219.

56 G.-R. Xu, B. Wang, J.-Y. Zhu, F.-Y. Liu, Y. Chen, J.-H. Zeng, J.-X. Jiang, Z.-H. Liu, Y.-W. Tang and J.-M. Lee, *ACS Catal.*, 2016, **6**, 5260–5267.

57 G.-R. Xu, J. Bai, L. Yao, Q. Xue, J.-X. Jiang, J.-H. Zeng, Y. Chen and J.-M. Lee, *ACS Catal.*, 2017, **7**, 452–458.

58 Y. Ding, B.-Q. Miao, Y.-C. Jiang, H.-C. Yao, X.-F. Li and Y. Chen, *J. Mater. Chem. A*, 2019, **7**, 13770–13776.

59 D. Strmcnik, M. Escudero-Escribano, K. Kodama, V. R. Stamenkovic, A. Cuesta and N. M. Marković, *Nat. Chem.*, 2010, **2**, 880–885.

60 B. Genorio, D. Strmcnik, R. Subbaraman, D. Tripkovic, G. Karapetrov, V. R. Stamenkovic, S. Pejovnik and N. M. Marković, *Nat. Mater.*, 2010, **9**, 998–1003.

61 B. Genorio, R. Subbaraman, D. Strmcnik, D. Tripkovic and V. R. Stamenkovic, *Angew. Chem., Int. Ed.*, 2011, **50**, 5468–5472.

62 J. Bai, N. Jia, P. Jin, P. Chen, J.-X. Jiang, J.-H. Zeng and Y. Chen, *J. Energy Chem.*, 2020, **51**, 105–112.

63 S.-i. Yamazaki, M. Asahi and T. Ioroi, *Electrochim. Acta*, 2019, **297**, 725–734.

64 S.-i. Yamazaki, M. Asahi, N. Taguchi, T. Ioroi, Y. Kishimoto, H. Daimon, M. Inaba, K. Koga, Y. Kurose and H. Inoue, *ACS Catal.*, 2020, **10**, 14567–14580.

65 S. Chen, Z. Wei, X. Q. Qi, L. Dong, Y.-G. Guo, L. Wan, Z. Shao and L. Li, *J. Am. Chem. Soc.*, 2012, **134**, 13252–13255.

66 X. Sun, N. Zhang and X. Huang, *ChemCatChem*, 2016, **8**, 3436–3440.

67 A.-L. Wang, H. Xu, J.-X. Feng, L.-X. Ding, Y.-X. Tong and G.-R. Li, *J. Am. Chem. Soc.*, 2013, **135**, 10703–10709.

68 K. S. Kim, Y. Hong, H. C. Kim, S.-I. Choi and J. W. Hong, *Chem. – Eur. J.*, 2019, **25**, 7185–7190.

69 Y. Liu, K. Ai and L. Lu, *Chem. Rev.*, 2014, **114**, 5057–5115.

70 L. Shen, H. Lv, S. Chen, P. Kopold, P. A. van Aken, X. Wu, J. Maier and Y. Yu, *Adv. Mater.*, 2017, **29**, 1700142.

71 C. M. Parnell, B. Chhetri, A. Brandt, F. Watanabe, Z. A. Nima, T. K. Mudalige, A. S. Biris and A. Ghosh, *Sci. Rep.*, 2016, **6**, 31415.

72 T. Fujigaya, M. Okamoto and N. Nakashima, *Carbon*, 2009, **47**, 3227–3232.

73 K. Matsumoto, T. Fujigaya, K. Sasakic and N. Nakashima, *J. Mater. Chem.*, 2011, **21**, 1187–1190.

74 T. Fujigaya, M. Okamoto, K. Matsumoto, K. Kaneko and N. Nakashima, *ChemCatChem*, 2013, **5**, 1701–1704.

75 Z. Yang and N. Nakashima, *Sci. Rep.*, 2015, **5**, 12236.

76 Z. Yang, M. R. Berber and N. Nakashima, *J. Mater. Chem. A*, 2014, **2**, 18875–18880.

77 Z. Yang, C. Kim, S. Hirata, T. Fujigaya and N. Nakashima, *ACS Appl. Mater. Interfaces*, 2015, **7**, 15885–15891.

78 Z. Yang, I. H. Hafez, M. R. Berber and N. Nakashima, *ChemCatChem*, 2015, **7**, 808–813.

79 Z. Yang, I. Moriguchi and N. Nakashima, *ACS Appl. Mater. Interfaces*, 2016, **8**, 9030–9036.

80 K. Cheng, Z. Kou, J. Zhang, M. Jiang, H. Wu, L. Hu, X. Yang, M. Pan and S. Mu, *J. Mater. Chem. A*, 2015, **3**, 14007–14014.

81 J. Liu, W. Li, R. Cheng, Q. Wu, J. Zhao, D. He and S. Mu, *Langmuir*, 2019, **35**, 2580–2586.

82 K. Ham, S. Chung and J. Lee, *J. Power Sources*, 2020, **450**, 227650.

83 L. Guo, W.-J. Jiang, Y. Zhang, J.-S. Hu, Z.-D. Wei and L.-J. Wan, *ACS Catal.*, 2015, **5**, 2903–2909.

84 M. Karuppannan, Y. Kim, S. Gok, E. Lee, J. Y. Hwang, J.-H. Jang, Y.-H. Cho, T. Lim, Y.-E. Sung and O. J. Kwon, *Energy Environ. Sci.*, 2019, **12**, 2820–2829.

85 H. Yamada, H. Kato and K. Kodama, *J. Electrochem. Soc.*, 2020, **167**, 084508.

86 X. Tong, J. Zhang, G. Zhang, Q. Wei, R. Chenitz, J. P. Claverie and S. Sun, *Chem. Mater.*, 2017, **29**, 9579–9587.

87 S. Guo, S. Zhang and S. Sun, *Angew. Chem., Int. Ed.*, 2013, **52**, 8526–8544.

88 D. Wang, H. L. Xin, R. Hovden, H. Wang, Y. Yu, D. A. Muller, F. J. DiSalvo and H. D. Abruña, *Nat. Mater.*, 2013, **12**, 81–87.

89 D. Y. Chung, S. W. Jun, G. Yoon, S. G. Kwon, D. Y. Shin, P. Seo, J. M. Yoo, H. Shin, Y.-H. Chung, H. Kim, B. S. Mun, K.-S. Lee, N.-S. Lee, S. J. Yoo, D.-H. Lim, K. Kang, Y.-E. Sung and T. Hyeon, *J. Am. Chem. Soc.*, 2015, **137**, 15478–15485.

90 Y. Cho, W. H. Lee and H. Kim, *J. Electrochem. Soc.*, 2016, **164**, F65–F70.

91 Q. Wang, S. Chen, F. Shi, K. Chen, Y. Nie, Y. Wang, R. Wu, J. Li, Y. Zhang, W. Ding, Y. Li, L. Li and Z. Wei, *Adv. Mater.*, 2016, **28**, 10673–10678.

92 X. Zou, S. Chen, Q. Wang, X. Gao, J. Li, J. Li, L. Li, W. Ding and Z. Wei, *Nanoscale*, 2019, **11**, 20115–20122.

93 S. Chen, Y. Yan, P. Hao, M. Li, J. Liang, J. Guo, Y. Zhang, S. Chen, W. Ding and X. Guo, *ACS Appl. Mater. Interfaces*, 2020, **12**, 12686–12695.

94 J. Jin, X. Fu, Q. Liu and J. Zhang, *J. Mater. Chem. A*, 2013, **1**, 10538–10545.

95 X.-W. Gao, J. Yang, K. Song, W.-B. Luo, S.-X. Dou and Y.-M. Kang, *J. Mater. Chem. A*, 2018, **6**, 23445–23456.

96 Z. Wang, B. Li, X. Ge, F. W. Thomas Goh, X. Zhang, G. Du, D. Wuu, Z. Liu, T. S. Andy Hor, H. Zhang and Y. Zong, *Small*, 2016, **12**, 2580–2587.

97 S. Yang, L. Chen, W. Wei, X. Lv and J. Xie, *Appl. Surf. Sci.*, 2019, **476**, 749–756.

98 S. A. Shah, Z. Ji, X. Shen, X. Yue, G. Zhu, K. Xu, A. Yuan, N. Ullah, J. Zhu, P. Song and X. Li, *ACS Appl. Energy Mater.*, 2019, **2**, 4075–4083.

99 S. Li, R. Wang, X. Yang, J. Wu, H. Meng, H. Xu and Z. Ren, *ACS Sustainable Chem. Eng.*, 2019, **7**, 11872–11884.

100 Y. Yuan, Y. Zhou, H. Shen, S. A. Rasaki, T. Thomas, J. Wang, C. Wang, J. Wang and M. Yang, *ACS Appl. Energy Mater.*, 2018, **1**, 6774–6780.

101 S. Huang, Y. Meng, S. He, A. Goswami, Q. Wu, J. Li, S. Tong, T. Asefa and M. Wu, *Adv. Funct. Mater.*, 2017, **27**, 1606585.

102 M. Karuppannan, J. E. Park, H. E. Bae, Y.-H. Cho and O. J. Kwon, *Nanoscale*, 2020, **12**, 2542–2554.

103 H. Wang, B. Hou, Y. Yang, Q. Chen, M. Zhu, A. Thomas and Y. Liao, *Small*, 2018, **14**, 1803232.

104 Y. Hu, J. O. Jensen, W. Zhang, L. N. Cleemann, W. Xing, N. J. Bjerrum and Q. Li, *Angew. Chem., Int. Ed.*, 2014, **53**, 3675–3679.

105 J. Deng, P. Ren, D. Deng and X. Bao, *Angew. Chem., Int. Ed.*, 2015, **54**, 2100–2104.

106 Z. Li, L. Cai, M. Song, Y. Shen, X. Wang, J. Li, J. Wang, P. Wang and L. Tian, *Electrochim. Acta*, 2020, **339**, 135886.

107 G. Li, Y. Sun, J. Rao, J. Wu, A. Kumar, Q. N. Xu, C. Fu, E. Liu, G. R. Blake, P. Werner, B. Shao, K. Liu, S. Parkin, X. Liu, M. Fahlman, S.-C. Liou, G. Auffermann, J. Zhang, C. Felser and X. Feng, *Adv. Energy Mater.*, 2018, **8**, 1801258.

108 Z. Pu, I. S. Amiinu, Z. Kou, W. Li and S. Mu, *Angew. Chem., Int. Ed.*, 2017, **56**, 11559–11564.

109 X. Lv, J. Ren, Y. Wang, Y. Liu and Z.-Y. Yuan, *ACS Sustainable Chem. Eng.*, 2019, **7**, 8993–9001.

110 Y.-Y. Ma, C.-X. Wu, X.-J. Feng, H.-Q. Tan, L.-K. Yan, Y. Liu, Z.-H. Kang, E.-B. Wang and Y.-G. Li, *Energy Environ. Sci.*, 2017, **10**, 788–798.

111 G. Yan, C. Wu, H. Tan, X. Feng, L. Yan, H. Zang and Y. Li, *J. Mater. Chem. A*, 2017, **5**, 765–772.

112 C. Pi, C. Huang, Y. Yang, H. Song, X. Zhang, Y. Zheng, B. Gao, J. Fu, P. K. Chu and K. Huo, *Appl. Catal., B*, 2020, **263**, 118358.

113 A. Bavykina, N. Kolobov, I. S. Khan, J. A. Bau, A. Ramirez and J. Gascon, *Chem. Rev.*, 2020, **120**, 8468–8535.

114 Z. Chen, H. Qing, K. Zhou, D. Sun and R. Wu, *Prog. Mater. Sci.*, 2020, **108**, 100618.

115 Q. Liang, J. Chen, F. Wang and Y. Li, *Coord. Chem. Rev.*, 2020, **424**, 213488.

116 X. Li, L. Yang, T. Su, X. Wang, C. Sun and Z. Su, *J. Mater. Chem. A*, 2017, **5**, 5000–5006.

117 M. Khalid, A. M. B. Honorato, G. T. Filho and H. Varela, *J. Mater. Chem. A*, 2020, **8**, 9021–9031.

118 Z. Shi, Y. Wang, H. Lin, H. Zhang, M. Shen, S. Xie, Y. Zhang, Q. Gao and Y. Tang, *J. Mater. Chem. A*, 2016, **4**, 6006–6013.

119 L. Wang, J. Cao, X. Cheng, C. Lei, Q. Dai, B. Yang, Z. Li, M. A. Younis, L. Lei, Y. Hou and K. Ostrikov, *ACS Sustainable Chem. Eng.*, 2019, **7**, 10044–10051.

120 H. Peng, M. Zhang, K. Sun, X. Xie, H. Lei and G. Ma, *Appl. Surf. Sci.*, 2020, **529**, 147174.

121 X. Zhu, M. Liu, Y. Liu, R. Chen, Z. Nie, J. Li and S. Yao, *J. Mater. Chem. A*, 2016, **4**, 8974–8977.

122 J. Su, G. Xia, R. Li, Y. Yang, J. Chen, R. Shi, P. Jiang and Q. Chen, *J. Mater. Chem. A*, 2016, **4**, 9204–9212.

123 B. Singh and A. Indra, *Mater. Today Energy*, 2020, **16**, 100404.

124 P. Jiang, J. Chen, C. Wang, K. Yang, S. Gong, S. Liu, Z. Lin, M. Li, G. Xia, Y. Yang, J. Su and Q. Chen, *Adv. Mater.*, 2018, **30**, 1705324.

125 J. Xi, Y. Xia, Y. Xu, J. Xiao and S. Wang, *Chem. Commun.*, 2015, **51**, 10479–10482.

126 L. Du, L. Luo, Z. Feng, M. Engelhard, X. Xie, B. Han, J. Sun, J. Zhang, G. Yin, C. Wang, Y. Wang and Y. Shao, *Nano Energy*, 2017, **39**, 245–252.

127 J.-S. Li, Y.-J. Tang, C.-H. Liu, S.-L. Li, R.-H. Li, L.-Z. Dong, Z.-H. Dai, J.-C. Bao and Y.-Q. Lan, *J. Mater. Chem. A*, 2016, **4**, 1202–1207.

128 P. He, X.-Y. Yu and X. W. Lou, *Angew. Chem., Int. Ed.*, 2017, **56**, 3897–3900.

129 Y.-T. Xu, X. Xiao, Z.-M. Ye, S. Zhao, R. Shen, C.-T. He, J.-P. Zhang, Y. Li and X.-M. Chen, *J. Am. Chem. Soc.*, 2017, **139**, 5285–5288.

130 F. Bu, W. Chen, M. F. Aly Aboud, I. Shakir, J. Gu and Y. Xu, *J. Mater. Chem. A*, 2019, **7**, 14526–14535.

131 Q. Hu, X. Liu, C. Tang, L. Fan, X. Chai, Q. Zhang, J. Liu and C. He, *Sustainable Energy Fuels*, 2018, **2**, 1085–1092.

132 L.-L. Wu, Q.-S. Wang, J. Li, Y. Long, Y. Liu, S.-Y. Song and H.-J. Zhang, *Small*, 2018, **14**, 1704035.

133 B. Xu, X. Wang, X. Yang, Z. Chen, Y. Sun, Q. Liu and C. Li, *Electrochim. Acta*, 2019, **296**, 738–745.

134 Q. Hu, X. Liu, C. Tang, L. Fan, X. Chai, Q. Zhang, J. Liu and C. He, *Electrochim. Acta*, 2018, **265**, 620–628.

135 F. Bu, W. Chen, J. Gu, P. O. Agboola, N. F. Al-Khalli, I. Shakir and Y. Xu, *Chem. Sci.*, 2018, **9**, 7009–7016.

136 X. Cui, P. Ren, D. Deng, J. Deng and X. Bao, *Energy Environ. Sci.*, 2016, **9**, 123–129.

137 X. Cui, P. Ren, C. Ma, J. Zhao, R. Chen, S. Chen, N. P. Rajan, H. Li, L. Yu, Z. Tian and D. Deng, *Adv. Mater.*, 2020, **32**, 1908126.

138 D. V. Esposito, *ACS Catal.*, 2018, **8**, 457–465.

139 N. Aoki, H. Inoue, H. Kawasaki, H. Daimon, T. Doi and M. Inaba, *J. Electrochem. Soc.*, 2018, **165**, F737.

140 S. Takenaka, A. Hirata, E. Tanabe, H. Matsune and M. Kishida, *J. Catal.*, 2010, **274**, 228–238.

141 S. Takenaka, H. Miyamoto, Y. Utsunomiya, H. Matsune and M. Kishida, *J. Phys. Chem. C*, 2014, **118**, 774–783.

142 S. Kang, F. Xia, Z. Hu, W. Hu, Y. She, L. Wang, X. Fu and W. Lu, *Electrochim. Acta*, 2020, **343**, 136119.

143 H. J. Kim, D. H. K. Jackson, J. Lee, Y. Guan, T. F. Kuech and G. W. Huber, *ACS Catal.*, 2015, **5**, 3463–3469.

144 X. Wang, Y. Yang, L. Diao, Y. Tang, F. He, E. Liu, C. He, C. Shi, J. Li, J. Sha, S. Ji, P. Zhang, L. Ma and N. Zhao, *ACS Appl. Mater. Interfaces*, 2018, **10**, 35145–35153.

145 H. Xu, J. Cao, C. Shan, B. Wang, P. Xi, W. Liu and Y. Tang, *Angew. Chem., Int. Ed.*, 2018, **57**, 8654–8658.

146 J. G. Vos, T. A. Wezendonk, A. W. Jeremiasse and M. T. M. Koper, *J. Am. Chem. Soc.*, 2018, **140**, 10270–10281.

147 W. J. Jo, G. Katsoukis and H. Frei, *Adv. Funct. Mater.*, 2020, **30**, 1909262.

148 B. Endrődi, V. Smulders, N. Simic, M. Wildlock, G. Mul, B. Mei and A. Cornell, *Appl. Catal., B*, 2019, **244**, 233–239.

149 B. Endrődi, O. Diaz-Morales, U. Mattinen, M. Cuartero, A. K. Padinjarethil, N. Simic, M. Wildlock, G. A. Crespo and A. Cornell, *Electrochim. Acta*, 2020, **341**, 136022.

150 D. He, C. Zeng, C. Xu, N. Cheng, H. Li, S. Mu and M. Pan, *Langmuir*, 2011, **27**, 5582–5588.

151 B. Ye, K. Cheng, W. Li, J. Liu, J. Zhang and S. Mu, *Langmuir*, 2017, **33**, 5353–5361.

152 Y. Wang, Z. Li, S. Xu, Y. Xie and S. Lin, *Mater. Res. Bull.*, 2018, **102**, 172–179.

153 B. Wu, D. Hu, Y. Kuang, B. Liu, X. Zhang and J. Chen, *Angew. Chem., Int. Ed.*, 2009, **48**, 4751–4754.

154 Q.-L. Zhang, T.-Q. Xu, J. Wei, J.-R. Chen, A.-J. Wang and J.-J. Feng, *Electrochim. Acta*, 2013, **112**, 127–132.

155 X. Yu, H. Wang, L. Guo and L. Wang, *Chem. – Asian J.*, 2014, **9**, 3221–3227.

156 W. Tamakloe, D. A. Agyeman, M. Park, J. Yang and Y.-M. Kang, *J. Mater. Chem. A*, 2019, **7**, 7396–7405.

157 R. Escudero Cid, J. L. Gómez de la Fuente, S. Rojas, J. L. García Fierro and P. Ocón, *ChemCatChem*, 2013, **5**, 3680–3689.

158 T. Fujigaya, S. Hirata, M. R. Berber and N. Nakashima, *ACS Appl. Mater. Interfaces*, 2016, **8**, 14494–14502.

159 M. Okamoto, T. Fujigaya and N. Nakashima, *Small*, 2009, **5**, 735–740.

160 S. M. Jayawickrama, Z. Han, S. Kido, N. Nakashima and T. Fujigaya, *Electrochim. Acta*, 2019, **312**, 349–357.

161 T. Fujigaya, Y. Shi, J. Yang, H. Li, K. Ito and N. Nakashima, *J. Mater. Chem. A*, 2017, **5**, 10584–10590.

162 Z. Yang and N. Nakashima, *J. Mater. Chem. A*, 2015, **3**, 23316–23322.

163 F. Morales-Lara, V. K. Abdelkader-Fernández, M. Melguizo, A. Turco, E. Mazzotta, M. Domingo-García, F. J. López-Garzón and M. Pérez-Mendoza, *J. Mater. Chem. A*, 2019, **7**, 24502–24514.

164 X.-C. Liu, G.-C. Wang, R.-P. Liang, L. Shi and J.-D. Qiu, *J. Mater. Chem. A*, 2013, **1**, 3945–3953.

165 H. Yang, H. Zou, M. Chen, S. Li, J. Jin and J. Ma, *Inorg. Chem. Front.*, 2017, **4**, 1881–1887.

166 M. R. Berber, I. H. Hafez, T. Fujigaya and N. Nakashima, *J. Mater. Chem. A*, 2014, **2**, 19053–19059.

167 M. Kato, R. Nakahoshiba, K. Ogura, S. Tokuda, S. Yasuda, K. Higashi, T. Uruga, Y. Uemura and I. Yagi, *ACS Appl. Energy Mater.*, 2020, **3**, 6768–6774.

168 T. Fujigaya and N. Nakashima, *Adv. Mater.*, 2013, **25**, 1666–1681.

169 N. Jung, S. Bhattacharjee, S. Gautam, H.-Y. Park, J. Ryu, Y.-H. Chung, S.-Y. Lee, I. Jang, J. H. Jang, S. H. Park, D. Y. Chung, Y.-E. Sung, K.-H. Chae, U. V. Waghmare, S.-C. Lee and S. J. Yoo, *NPG Asia Mater.*, 2016, **8**, e237.

170 Z.-Z. Jiang, Z.-B. Wang, Y.-Y. Chu, D.-M. Gu and G.-P. Yin, *Energy Environ. Sci.*, 2011, **4**, 2558–2566.

171 Z.-Z. Jiang, Z.-B. Wang, Y.-Y. Chu, D.-M. Gu and G.-P. Yin, *Energy Environ. Sci.*, 2011, **4**, 728–735.

172 Z.-Z. Jiang, Z.-B. Wang, W.-L. Qu, H. Rivera, D.-M. Gu and G.-P. Yin, *Nanoscale*, 2012, **4**, 7411–7418.

173 Q. Zhang, Z. Yang, J. Yang, X. Yu, Y. Ling, Y. Zhang, W. Cai and H. Cheng, *Chem. Commun.*, 2018, **54**, 9282–9285.

174 C.-Z. Li, Z.-B. Wang, X.-L. Sui, L.-M. Zhang, D.-M. Gu and S. Gu, *J. Mater. Chem. A*, 2014, **2**, 20139–20146.

175 C.-Z. Li, Z.-B. Wang, X.-L. Sui, L.-M. Zhang and D.-M. Gu, *Carbon*, 2015, **93**, 105–115.

176 S.-Y. Huang, P. Ganesan, S. Park and B. N. Popov, *J. Am. Chem. Soc.*, 2009, **131**, 13898–13899.

177 Y. Liu, S. Shrestha and W. E. Mustain, *ACS Catal.*, 2012, **2**, 456–463.

178 V. T. T. Ho, C.-J. Pan, J. Rick, W.-N. Su and B.-J. Hwang, *J. Am. Chem. Soc.*, 2011, **133**, 11716–11724.

179 T.-T. Nguyen, V. T. ThanhHo, C.-J. Pan, J.-Y. Liu, H.-L. Chou, J. Rick, W.-N. Su and B.-J. Hwang, *Appl. Catal., B*, 2014, **154**, 183–189.

180 A. Kumar and V. Ramani, *ACS Catal.*, 2014, **4**, 1516–1525.

181 Y. Liu and W. E. Mustain, *J. Am. Chem. Soc.*, 2013, **135**, 530–533.

182 A. S. Asundi, J. A. Raiford and S. F. Bent, *ACS Energy Lett.*, 2019, **4**, 908–925.

183 Y. Zhao and X. Sun, *ACS Energy Lett.*, 2018, **3**, 899–914.

184 Z. Gao and Y. Qin, *Acc. Chem. Res.*, 2017, **50**, 2309–2316.

185 X. Meng, X. Wang, D. Geng, C. Ozgit-Akgun, N. Schneider and J. W. Elam, *Mater. Horiz.*, 2017, **4**, 133–154.

186 B. Zhang and Y. Qin, *ACS Catal.*, 2018, **8**, 10064–10081.

187 K. Cao, J. Cai and R. Chen, *Chem. Mater.*, 2020, **32**, 2195–2207.

188 J. Lu, B. Fu, M. C. Kung, G. Xiao, J. W. Elam, H. H. Kung and P. C. Stair, *Science*, 2012, **335**, 1205–1208.

189 Y. Chen, J. Wang, X. Meng, Y. Zhong, R. Li, X. Sun, S. Ye and S. Knights, *J. Power Sources*, 2013, **238**, 144–149.

190 S. Hussain, H. Erikson, N. Kongi, A. Tarre, P. Ritslaid, M. Kook, M. Rähn, M. Merisalu, V. Sammelselg and K. Tammeveski, *J. Electrochem. Soc.*, 2019, **166**, F1284–F1291.

191 N. Cheng, M. N. Banis, J. Liu, A. Riese, X. Li, R. Li, S. Ye, S. Knights and X. Sun, *Adv. Mater.*, 2015, **27**, 277–281.

192 Z. Song, B. Wang, N. Cheng, L. Yang, D. Banham, R. Li, S. Ye and X. Sun, *J. Mater. Chem. A*, 2017, **5**, 9760–9767.

193 L. Zhang, Y. Zhao, M. N. Banis, K. Adair, Z. Song, L. Yang, M. Markiewicz, J. Li, S. Wang, R. Li, S. Ye and X. Sun, *Nano Energy*, 2019, **60**, 111–118.

194 C. Du, X. Gao, C. Cheng, Z. Zhuang, X. Li and W. Chen, *Electrochim. Acta*, 2018, **266**, 348–356.

195 F. Xu, D. Wang, B. Sa, Y. Yu and S. Mu, *Int. J. Hydrogen Energy*, 2017, **42**, 13011–13019.

196 Y. Li, X. Zhang, S. Wang and G. Sun, *ChemElectroChem*, 2018, **5**, 2442–2448.

197 Y.-J. Wang, D. P. Wilkinson, V. Neburchilov, C. Song, A. Guest and J. Zhang, *J. Mater. Chem. A*, 2014, **2**, 12681–12685.

198 Y. Zhuang, W. Ding, Y. Liu, Z. Mou, J. Sun and M. Guan, *J. Mater. Sci.*, 2015, **50**, 3875–3882.

199 J. Wang, M. Xu, J. Zhao, H. Fang, Q. Huang, W. Xiao, T. Li and D. Wang, *Appl. Catal., B*, 2018, **237**, 228–236.

200 N. G. Akalework, C.-J. Pan, W.-N. Su, J. Rick, M.-C. Tsai, J.-F. Lee, J.-M. Lin, L.-D. Tsai and B.-J. Hwang, *J. Mater. Chem.*, 2012, **22**, 20977–20985.

201 J. Huang, J. Zang, Y. Zhao, L. Dong and Y. Wang, *Mater. Lett.*, 2014, **137**, 335–338.

202 S. Hussain, N. Kongi, H. Erikson, M. Rähn, M. Merisalu, L. Matisen, P. Paiste, J. Aruväli, V. Sammelselg, L. A. Estudillo-Wong, K. Tammeveski and N. Alonso-Vante, *Electrochim. Acta*, 2019, **316**, 162–172.

203 Z. Ma, S. Li, L. Wu, L. Song, G. Jiang, Z. Liang, D. Su, Y. Zhu, R. R. Adzic, J. X. Wang and Z. Chen, *Nano Energy*, 2020, **69**, 104455.

204 Y. Qu, Y. Gao, L. Wang, J. Rao and G. Yin, *Chem. – Eur. J.*, 2016, **22**, 193–198.

205 W. Gao, T. Liu, Z. Zhang, M. Dou and F. Wang, *J. Mater. Chem. A*, 2020, **8**, 5525–5534.

206 A. Meng, L. Lin, X. Yuan, T. Shen, Z. Li and Q. Li, *ChemCatChem*, 2019, **11**, 2900–2908.

207 Y.-P. Xiao, W.-J. Jiang, S. Wan, X. Zhang, J.-S. Hu, Z.-D. Wei and L.-J. Wan, *J. Mater. Chem. A*, 2013, **1**, 7463–7468.

208 L. Wang, W. Wu, Z. Lei, T. Zeng, Y. Tan, N. Cheng and X. Sun, *J. Mater. Chem. A*, 2020, **8**, 592–598.

209 Z. M. Cui, S. P. Jiang and C. M. Li, *Chem. Commun.*, 2011, **47**, 8418–8420.

210 S. Wu, J. Liu, Y. Ye, Z. Tian, X. Zhu and C. Liang, *ACS Appl. Energy Mater.*, 2019, **2**, 5577–5583.

211 Y.-Y. Chu, Z.-B. Wang, Z.-Z. Jiang, D.-M. Gu and G.-P. Yin, *Adv. Mater.*, 2011, **23**, 3100–3104.

212 Y. Y. Chu, J. Cao, Z. Dai and X. Y. Tan, *J. Mater. Chem. A*, 2014, **2**, 4038–4044.

213 D.-G. Lee, H. Jeong, K.-W. Jeon, L. Zhang, K. Park, S. Ryu, J. Kim and I. S. Lee, *J. Mater. Chem. A*, 2017, **5**, 22341–22351.

214 J. Zhu, M. Xiao, X. Zhao, C. Liu and W. Xing, *J. Power Sources*, 2015, **292**, 78–86.

215 W. Li, Y. Bai, F. Li, C. Liu, K.-Y. Chan, X. Feng and X. Lu, *J. Mater. Chem.*, 2012, **22**, 4025–4031.

216 X. Wu, W. Zhuang, L. Lu, L. Li, J. Zhu, L. Mu, W. Li, Y. Zhu and X. Lu, *Appl. Surf. Sci.*, 2017, **426**, 890–896.

217 Y. Chang, C. Yuan, Y. Li, C. Liu, T. Wu, B. Zeng, Y. Xu and L. Dai, *J. Mater. Chem. A*, 2017, **5**, 1672–1678.

218 A. Kulkarni, S. Siahrostami, A. Patel and J. K. Nørskov, *Chem. Rev.*, 2018, **118**, 2302–2312.

219 N. Jung, H. Shin, M. Kim, I. Jang, H.-J. Kim, J. H. Jang, H. Kim and S. J. Yoo, *Nano Energy*, 2015, **17**, 152–159.

220 Y. Tan, C. Xu, G. Chen, N. Zheng and Q. Xie, *Energy Environ. Sci.*, 2012, **5**, 6923–6927.

221 L. Lu, Z. Wang, S. Zou, Y. Zhou, W. Hong, R. Li, L. Xiao, J. Liu, X.-Q. Gong and J. Fan, *J. Mater. Chem. A*, 2018, **6**, 18884–18890.

222 Y.-H. Chung, D. Y. Chung, N. Jung and Y.-E. Sung, *J. Phys. Chem. Lett.*, 2013, **4**, 1304–1309.

223 H. S. Casalongue, S. Kaya, V. Viswanathan, D. J. Miller, D. Friebel, H. A. Hansen, J. K. Nørskov, A. Nilsson and H. Ogasawara, *Nat. Commun.*, 2013, **4**, 2817.

224 Z.-Y. Zhou, X. Kang, Y. Song and S. Chen, *J. Phys. Chem. C*, 2012, **116**, 10592–10598.

225 M. Asahi, S.-i. Yamazaki, N. Taguchi and T. Ioroi, *J. Electrochem. Soc.*, 2019, **166**, F498–F505.

226 J. Snyder, K. Livi and J. Erlebacher, *Adv. Funct. Mater.*, 2013, **23**, 5494–5501.

227 G.-R. Zhang, M. Munoz and B. J. M. Etzold, *Angew. Chem., Int. Ed.*, 2016, **55**, 2257–2261.

228 M. George, G.-R. Zhang, N. Schmitt, K. Brunnengräber, D. J. S. Sandbeck, K. J. J. Mayrhofer, S. Cherevko and B. J. M. Etzold, *ACS Catal.*, 2019, **9**, 8682–8692.

229 W. Song, Z. Chen, C. Yang, Z. Yang, J. Tai, Y. Nan and H. Lu, *J. Mater. Chem. A*, 2015, **3**, 1049–1057.

230 Y. Nie, S. Chen, W. Ding, X. Xie, Y. Zhang and Z. Wei, *Chem. Commun.*, 2014, **50**, 15431–15434.

231 K. Sun, J. Li, F. Wang, W. He, M. Fei, Z. Lu, H. Zhang, J. Liu and Z. Zou, *Chem. Commun.*, 2019, **55**, 5693–5696.

232 G. Chen, H. Shan, Y. Li, H. Bao, T. Hu, L. Zhang, S. Liu and F. Ma, *J. Mater. Chem. A*, 2020, **8**, 10337–10345.

233 W. Wu, Z. Zhang, Z. Lei, X. Wang, Y. Tan, N. Cheng and X. Sun, *ACS Appl. Mater. Interfaces*, 2020, **12**, 10359–10368.

234 W. Li and S. Zou, *ACS Appl. Energy Mater.*, 2019, **2**, 2769–2778.

235 S. Takenaka, T. Miyazaki, H. Matsune and M. Kishida, *Catal. Sci. Technol.*, 2015, **5**, 1133–1142.

236 K. Park, T. Ohnishi, M. Goto, M. So, S. Takenaka, Y. Tsuge and G. Inoue, *Int. J. Hydrogen Energy*, 2020, **45**, 1867–1877.

237 G. Wu and P. Zelenay, *Acc. Chem. Res.*, 2013, **46**, 1878–1889.

238 R. Bashyam and P. Zelenay, *Nature*, 2006, **443**, 63–66.

239 G. Wu, K. L. More, C. M. Johnston and P. Zelenay, *Science*, 2011, **332**, 443–447.

240 Z. Dong, M. Li, W. Zhang, Y. Liu, Y. Wang., C. Qin, L. Yu, J. Yang, X. Zhang and X. Dai, *ChemCatChem*, 2019, **11**, 6039–6050.

241 H.-S. Park, S.-B. Han, D.-H. Kwak, J.-H. Han and K.-W. Park, *J. Catal.*, 2019, **370**, 130–137.

242 J. Deng, L. Yu, D. Deng, X. Chen, F. Yang and X. Bao, *J. Mater. Chem. A*, 2013, **1**, 14868–14873.

243 S. Gao, B. Fan, R. Feng, C. Ye, X. Wei, J. Liu and X. Bu, *Nano Energy*, 2017, **40**, 462–470.

244 Y. Hou, T. Huang, Z. Wen, S. Mao, S. Cui and J. Chen, *Adv. Energy Mater.*, 2014, **4**, 1400337.

245 K. Vezzù, A. B. Delpeuch, E. Negro, S. Polizzi, G. Nawn, F. Bertasi, G. Pagot, K. Artyushkova, P. Atanassov and V. Di Noto, *Electrochim. Acta*, 2016, **222**, 1778–1791.

246 K. Yuan, S. Sfaelou, M. Qiu, D. Lützenkirchen-Hecht, X. Zhuang, Y. Chen, C. Yuan, X. Feng and U. Scherf, *ACS Energy Lett.*, 2018, **3**, 252–260.

247 J. Ryu, N. Jung, D.-H. Lim, D. Y. Shin, S. H. Park, H. C. Ham, J. H. Jang, H.-J. Kim and S. J. Yoo, *Chem. Commun.*, 2014, **50**, 15940–15943.

248 X. Zhong, Y. Jiang, X. Chen, L. Wang, G. Zhuang, X. Li and J.-G. Wang, *J. Mater. Chem. A*, 2016, **4**, 10575–10584.

249 C. Han, X. Bo, Y. Zhang, M. Li, A. Wang and L. Guo, *Chem. Commun.*, 2015, **51**, 15015–15018.

250 Z. Pu, R. Cheng, J. Zhao, Z. Hu, C. Li, W. Li, P. Wang, I. S. Amiinu, Z. Wang, M. Wang, D. Chen and S. Mu, *iScience*, 2020, **23**, 101793.

251 D. Strmcnik, M. Uchimura, C. Wang, R. Subbaraman, N. Danilovic, D. van der Vliet, A. P. Paulikas, V. R. Stamenkovic and N. M. Markovic, *Nat. Chem.*, 2013, **5**, 300–306.

252 K. Elbert, J. Hu, Z. Ma, Y. Zhang, G. Chen, W. An, P. Liu, H. S. Isaacs, R. R. Adzic and J. X. Wang, *ACS Catal.*, 2015, **5**, 6764–6772.

253 J. Ohyama, D. Kumada and A. Satsuma, *J. Mater. Chem. A*, 2016, **4**, 15980–15985.

254 H. Wang and H. D. Abruña, *J. Am. Chem. Soc.*, 2017, **139**, 6807–6810.

255 Y. Cong, B. Yi and Y. Song, *Nano Energy*, 2018, **44**, 288–303.

256 L. Su, D. Gong, Y. Jin, D. Wu and W. Luo, *J. Energy Chem.*, 2022, **66**, 107–122.

257 J. Zheng, W. Sheng, Z. Zhuang, B. Xu and Y. Yan, *Sci. Adv.*, 2016, **2**, e1501602.

258 T. Wang, Z.-X. Chen, S. Yu, T. Sheng, H.-B. Ma, L.-N. Chen, M. Rauf, H.-P. Xia, Z.-Y. Zhou and S.-G. Sun, *Energy Environ. Sci.*, 2018, **11**, 166–171.

259 M. Sun, Y. Lv, Y. Song, H. Wu, G. Wang, H. Zhang, M. Chen, Q. Fu and X. Bao, *Appl. Surf. Sci.*, 2018, **450**, 244–250.

260 S.-W. Yun, S.-A. Park, T.-J. Kim, J.-H. Kim, G.-W. Pak and Y.-T. Kim, *ChemSusChem*, 2017, **10**, 489–493.

261 J. Jang, M. Sharma, D. Choi, Y. S. Kang, Y. Kim, J. Min, H. Sung, N. Jung and S. J. Yoo, *ACS Appl. Mater. Interfaces*, 2019, **11**, 27735–27742.

262 R. K. Singh, E. S. Davydova, J. Douglin, A. O. Godoy, H. Tan, M. Bellini, B. J. Allen, J. Jankovic, H. A. Miller, A. C. Alba-Rubio and D. R. Dekel, *Adv. Funct. Mater.*, 2020, **30**, 2002087.

263 F. D. Speck, F. S. M. Ali, M. T. Y. Paul, R. K. Singh, T. Böhm, A. Hofer, O. Kasian, S. Thiele, J. Bachmann, D. R. Dekel, T. Kallio and S. Cherevko, *Chem. Mater.*, 2020, **32**, 7716–7724.

264 B. M. Stühmeier, S. Selve, M. U. M. Patel, T. N. Geppert, H. A. Gasteiger and H. A. El-Sayed, *ACS Appl. Energy Mater.*, 2019, **2**, 5534–5539.

265 T. N. Geppert, M. Bosund, M. Putkonen, B. M. Stühmeier, A. T. Pasanen, P. Heikkilä, H. A. Gasteiger and H. A. El-Sayed, *J. Electrochem. Soc.*, 2020, **167**, 084517.

266 G. Zhao, J. Chen, W. Sun and H. Pan, *Adv. Funct. Mater.*, 2021, **31**, 2010633.

267 A. G. Oshchepkov, G. Braesch, A. Bonnefont, E. R. Savinova and M. Chatenet, *ACS Catal.*, 2020, **10**, 7043–7068.

268 S. Kabir, K. Lemire, K. Artyushkova, A. Roy, M. Odgaard, D. Schlueter, A. Oshchepkov, A. Bonnefont, E. Savinova, D. C. Sabarirajan, P. Mandal, E. J. Crumlin, I. V. Zenyuk, P. Atanassov and A. Serov, *J. Mater. Chem. A*, 2017, **5**, 24433–24443.

269 M. Wang, H. Yang, J. Shi, Y. Chen, Y. Zhou, L. Wang, S. Di, X. Zhao, J. Zhong, T. Cheng, W. Zhou and Y. Li, *Angew. Chem., Int. Ed.*, 2021, **60**, 5771–5777.

270 A. Roy, M. R. Talarposhti, S. J. Normile, I. V. Zenyuk, V. D. Andrade, K. Artyushkova, A. Serov and P. Atanassov, *Sustainable Energy Fuels*, 2018, **2**, 2268–2275.

271 W. Sheng, A. P. Bivens, M. Myint, Z. Zhuang, R. V. Forest, Q. Fang, J. G. Chen and Y. Yan, *Energy Environ. Sci.*, 2014, **7**, 1719–1724.

272 S. Qin, Y. Duan, X.-L. Zhang, L.-R. Zheng, F.-Y. Gao, P.-P. Yang, Z.-Z. Niu, R. Liu, Y. Yang, X.-S. Zheng, J.-F. Zhu and M.-R. Gao, *Nat. Commun.*, 2021, **12**, 2686.

273 T. Wang, M. Wang, H. Yang, M. Xu, C. Zuo, K. Feng, M. Xie, J. Deng, J. Zhong, W. Zhou, T. Cheng and Y. Li, *Energy Environ. Sci.*, 2019, **12**, 3522–3529.

274 F. Yang, P. Han, N. Yao, G. Cheng, S. Chen and W. Luo, *Chem. Sci.*, 2020, **11**, 12118–12123.

275 W. Ni, T. Wang, P. A. Schouwink, Y.-C. Chuang, H. M. Chen and X. Hu, *Angew. Chem., Int. Ed.*, 2020, **59**, 10797–10801.

276 F. Song, W. Li, J. Yang, G. Han, P. Liao and Y. Sun, *Nat. Commun.*, 2018, **9**, 4531.

277 Z. Zhuang, S. A. Giles, J. Zheng, G. R. Jenness, S. Caratzoulas, D. G. Vlachos and Y. Yan, *Nat. Commun.*, 2016, **7**, 10141.

278 F. Yang, X. Bao, Y. Zhao, X. Wang, G. Cheng and W. Luo, *J. Mater. Chem. A*, 2019, **7**, 10936–10941.

279 Y. Zhou, Z. Xie, J. Jiang, J. Wang, X. Song, Q. He, W. Ding and Z. Wei, *Nat. Catal.*, 2020, **3**, 454–462.

280 A. G. Oshchepkov, A. Bonnefont and E. R. Savinova, *Curr. Opin. Electrochem.*, 2021, **26**, 100667.

281 F. Yang, X. Bao, P. Li, X. Wang, G. Cheng, S. Chen and W. Luo, *Angew. Chem., Int. Ed.*, 2019, **58**, 14179–14183.

282 Y. Yang, X. Sun, G. Han, X. Liu, X. Zhang, Y. Sun, M. Zhang, Z. Cao and Y. Sun, *Angew. Chem., Int. Ed.*, 2019, **58**, 10644–10649.

283 A. G. Oshchepkov, A. Bonnefont, V. A. Saveleva, V. Papaefthimiou, S. Zafeiratos, S. N. Pronkin, V. N. Parmon and E. R. Savinova, *Top. Catal.*, 2016, **59**, 1319–1331.

284 A. G. Oshchepkov, A. Bonnefont, V. N. Parmon and E. R. Savinova, *Electrochim. Acta*, 2018, **269**, 111–118.

285 A. G. Oshchepkov, A. Bonnefont and E. R. Savinova, *Electrocatalysis*, 2020, **11**, 133–142.

286 Y. Pan, G. Hu, J. Lu, L. Xiao and L. Zhuang, *J. Energy Chem.*, 2019, **29**, 111–115.

287 E. S. Davydova, F. D. Speck, M. T. Y. Paul, D. R. Dekel and S. Cherevko, *ACS Catal.*, 2019, **9**, 6837–6845.

288 L. Gao, Y. Wang, H. Li, Q. Li, N. Ta, L. Zhuang, Q. Fu and X. Bao, *Chem. Sci.*, 2017, **8**, 5728–5734.

289 Y. Gao, H. Peng, Y. Wang, G. Wang, L. Xiao, J. Lu and L. Zhuang, *ACS Appl. Mater. Interfaces*, 2020, **12**, 31575–31581.

290 J. Wang, X. Dong, J. Liu, W. Li, L. T. Roling, J. Xiao and L. Jiang, *ACS Catal.*, 2021, **11**, 7422–7428.

291 B. Xiong, W. Zhao, L. Chen and J. Shi, *Adv. Funct. Mater.*, 2019, **29**, 1902505.

292 L. Wang, E. Magliocca, E. L. Cunningham, W. E. Mustain, S. D. Poynton, R. Escudero-Cid, M. M. Nasef, J. Ponce-González, R. Bance-Souahli, R. C. T. Slade, D. K. Whelligan and J. R. Varcoe, *Green Chem.*, 2017, **19**, 831–843.

293 S. Lu, J. Pan, A. Huang, L. Zhuang and J. Lu, *Proc. Natl. Acad. Sci. U. S. A.*, 2008, **105**, 20611–20614.

294 Q. Wang, S. Chen, H. Lan, P. Li, X. Ping, S. Ibraheem, D. Long, Y. Duan and Z. Wei, *J. Mater. Chem. A*, 2019, **7**, 18143–18149.

295 J. E. Robinson, N. Y. Labrador, H. Chen, B. E. Sartor and D. V. Esposito, *ACS Catal.*, 2018, **8**, 11423–11434.

296 P. Dhanasekaran, A. Shukla, S. V. Selvaganesh, S. Mohan and S. D. Bhat, *J. Power Sources*, 2019, **438**, 226999.

297 H. Lv, N. Cheng, T. Peng, M. Pan and S. Mu, *J. Mater. Chem.*, 2012, **22**, 1135–1141.

298 L. Xin, F. Yang, S. Rasouli, Y. Qiu, Z.-F. Li, A. Uzunoglu, C.-J. Sun, Y. Liu, P. Ferreira, W. Li, Y. Ren, L. A. Stanciu and J. Xie, *ACS Catal.*, 2016, **6**, 2642–2653.

299 C.-H. Hsu, H.-Y. Liao and P.-L. Kuo, *J. Phys. Chem. C*, 2010, **114**, 7933–7939.

300 Z. Yang, J. Li, Y. Ling, Q. Zhang, X. Yu and W. Cai, *ChemCatChem*, 2017, **9**, 3307–3313.

301 Z. Yang, T. Fujigaya and N. Nakashima, *J. Power Sources*, 2015, **300**, 175–181.

302 Z. Song, M. N. Banis, L. Zhang, B. Wang, L. Yang, D. Banham, Y. Zhao, J. Liang, M. Zheng, R. Li, S. Ye and X. Sun, *Nano Energy*, 2018, **53**, 716–725.

303 W. Yuan, J. Li, L. Wang, P. Chen, A. Xie and Y. Shen, *ACS Appl. Mater. Interfaces*, 2014, **6**, 21978–21985.

304 C. Xie, Z. Niu, D. Kim, M. Li and P. Yang, *Chem. Rev.*, 2020, **120**, 1184–1249.

305 R. Kou, Y. Shao, D. Mei, Z. Nie, D. Wang, C. Wang, V. V. Viswanathan, S. Park, I. A. Aksay, Y. Lin, Y. Wang and J. Liu, *J. Am. Chem. Soc.*, 2011, **133**, 2541–2547.

306 H. Huang, Q. Chen, M. He, X. Sun and X. Wang, *J. Power Sources*, 2013, **239**, 189–195.

307 H. Huang, Y. Liu, Q. Gao, W. Ruan, X. Lin and X. Li, *ACS Appl. Mater. Interfaces*, 2014, **6**, 10258–10264.

308 Q. Jia, S. Ghoshal, J. Li, W. Liang, G. Meng, H. Che, S. Zhang, Z.-F. Ma and S. Mukerjee, *J. Am. Chem. Soc.*, 2017, **139**, 7893–7903.

309 W. Gao, Z. Zhang, M. Dou and F. Wang, *ACS Catal.*, 2019, **9**, 3278–3288.

310 Z. Zhang, J. Liu, J. Gu, L. Su and L. Cheng, *Energy Environ. Sci.*, 2014, **7**, 2535–2558.

311 K. W. Kim, S. M. Kim, S. Choi, J. Kim and I. S. Lee, *ACS Nano*, 2012, **6**, 5122–5129.

312 T. Qu, Q. Tan, Y. Chen, L. Liu, S. Guo, Y. Chen, Y. Liu, S. Li and Y. Liu, *ACS Appl. Energy Mater.*, 2019, **2**, 8449–8458.

313 Q. Shi, C. Zhu, D. Du and Y. Lin, *Chem. Soc. Rev.*, 2019, **48**, 3181–3192.

314 H. Xu, H. Shang, C. Wang and Y. Du, *Coord. Chem. Rev.*, 2020, **418**, 213374.

315 A. Sivanantham, P. Ganesan, L. Estevez, B. P. McGrail, R. K. Motkuri and S. Shanmugam, *Adv. Energy Mater.*, 2018, **8**, 1702838.

316 J. Yu, X. Hou, C. Zhai, J. Li, A. Sartorel, M. Carraro, Z. Xin and Y. Huang, *ACS Sustainable Chem. Eng.*, 2020, **8**, 6127–6133.

317 M. Tahir, N. Mahmood, L. Pan, Z.-F. Huang, Z. Lv, J. Zhang, F. K. Butt, G. Shen, X. Zhang, S. X. Dou and J.-J. Zou, *J. Mater. Chem. A*, 2016, **4**, 12940–12946.

318 K. Obata and K. Takanabe, *Angew. Chem., Int. Ed.*, 2018, **57**, 1616–1620.

319 D. Zhao, Y. Pi, Q. Shao, Y. Feng, Y. Zhang and X. Huang, *ACS Nano*, 2018, **12**, 6245–6251.

320 R. Bose, K. Karuppasamy, H. Rajan, D. B. Velusamy, H.-S. Kim and A. Alfantazi, *ACS Sustainable Chem. Eng.*, 2019, **7**, 16392–16400.

321 B. Qiu, C. Wang, N. Zhang, L. Cai, Y. Xiong and Y. Chai, *ACS Catal.*, 2019, **9**, 6484–6490.

322 D. Deng, L. Yu, X. Chen, G. Wang, L. Jin, X. Pan, J. Deng, G. Sun and X. Bao, *Angew. Chem., Int. Ed.*, 2013, **52**, 371–375.

323 D. Xie, Y. Chen, D. Yu, S. Han, J. Song, Y. Xie, F. Hu, L. Li and S. Peng, *Chem. Commun.*, 2020, **56**, 6842–6845.

324 Y. Yang, Z. Lin, S. Gao, J. Su, Z. Lun, G. Xia, J. Chen, R. Zhang and Q. Chen, *ACS Catal.*, 2017, **7**, 469–479.

325 T. Najam, S. S. A. Shah, W. Ding, Z. Ling, L. Li and Z. Wei, *Electrochim. Acta*, 2019, **327**, 134939.

326 X.-Y. Yu, Y. Feng, B. Guan, X. W. Lou and U. Paik, *Energy Environ. Sci.*, 2016, **9**, 1246–1250.

327 J. Yu, Q. Li, N. Chen, C.-Y. Xu, L. Zhen, J. Wu and V. P. Dravid, *ACS Appl. Mater. Interfaces*, 2016, **8**, 27850–27858.

328 Y. Liu, Q. Wang, L. Wu, Y. Long, J. Li, S. Song and H. Zhang, *Cryst. Growth Des.*, 2018, **18**, 3404–3410.

329 J. Han, G. Chen, X. Liu, N. Zhang, S. Liang, R. Ma and G. Qiu, *Chem. Commun.*, 2019, **55**, 9212–9215.

330 J.-Y. Zhao, R. Wang, S. Wang, Y.-R. Lv, H. Xu and S.-Q. Zang, *J. Mater. Chem. A*, 2019, **7**, 7389–7395.

331 Z. Chen, R. Wu, M. Liu, Y. Liu, S. Xu, Y. Ha, Y. Guo, X. Yu, D. Sun and F. Fang, *J. Mater. Chem. A*, 2018, **6**, 10304–10312.

332 Q. Yang, L. Liu, L. Xiao, L. Zhang, M. J. Wang, J. Li and Z. Wei, *J. Mater. Chem. A*, 2018, **6**, 14752–14760.

333 W. Zhang, W. Chen, Q. Xiao, L. Yu, C. Huang, G. Lu, A. W. Morawski and Y. Yu, *Appl. Catal., B*, 2020, **268**, 118449.

334 N. Danilovic, R. Subbaraman, D. Strmcnik, K.-C. Chang, A. P. Paulikas, V. R. Stamenkovic and N. M. Markovic, *Angew. Chem., Int. Ed.*, 2012, **51**, 12495–12498.

335 W. Sheng, Z. Zhuang, M. Gao, J. Zheng, J. G. Chen and Y. Yan, *Nat. Commun.*, 2015, **6**, 5848.

336 G.-R. Xu, J. Bai, J.-X. Jiang, J.-M. Lee and Y. Chen, *Chem. Sci.*, 2017, **8**, 8411–8418.

337 J. Ying, G. Jiang, Z. P. Cano, L. Han, X.-Y. Yang and Z. Chen, *Nano Energy*, 2017, **40**, 88–94.

338 N. Y. Labrador, E. L. Songcuan, C. D. Silva, H. Chen, S. J. Kurdziel, R. K. Ramachandran, C. Detavernier and D. V. Esposito, *ACS Catal.*, 2018, **8**, 1767–1778.

339 M. E. S. Beatty, H. Chen, N. Y. Labrador, B. J. Lee and D. V. Esposito, *J. Mater. Chem. A*, 2018, **6**, 22287–22300.

340 Y. Li, L. A. Zhang, Y. Qin, F. Chu, Y. Kong, Y. Tao, Y. Li, Y. Bu, D. Ding and M. Liu, *ACS Catal.*, 2018, **8**, 5714–5720.

341 X. Ji, B. Liu, X. Ren, X. Shi, A. M. Asiri and X. Sun, *ACS Sustainable Chem. Eng.*, 2018, **6**, 4499–4503.

342 Y. Xu, S. Yin, C. Li, K. Deng, H. Xue, X. Li, H. Wang and L. Wang, *J. Mater. Chem. A*, 2018, **6**, 1376–1381.

343 J. Su, Y. Yang, G. Xia, J. Chen, P. Jiang and Q. Chen, *Nat. Commun.*, 2017, **8**, 14969.

344 W.-L. Yu, J.-Q. Chi and B. Dong, *J. Mater. Chem. A*, 2021, **9**, 2195–2204.

345 Y. Xu, W. Tu, B. Zhang, S. Yin, Y. Huang, M. Kraft and R. Xu, *Adv. Mater.*, 2017, **29**, 1605957.

346 J. Deng, P. Ren, D. Deng, L. Yu, F. Yang and X. Bao, *Energy Environ. Sci.*, 2014, **7**, 1919–1923.

347 X. Zou, X. Huang, A. Goswami, R. Silva, B. R. Sathe, E. Mikmeková and T. Asefa, *Angew. Chem., Int. Ed.*, 2014, **53**, 4372–4376.

348 M. Tavakkoli, T. Kallio, O. Reynaud, A. G. Nasibulin, C. Johans, J. Sainio, H. Jiang, E. I. Kauppinen and K. Laasonen, *Angew. Chem., Int. Ed.*, 2015, **54**, 4535–4538.

349 W. Zhou, Y. Zhou, L. Yang, J. Huang, Y. Ke, K. Zhou, L. Li and S. Chen, *J. Mater. Chem. A*, 2015, **3**, 1915–1919.

350 X. Dai, Z. Li, Y. Ma, M. Liu, K. Du, H. Su, H. Zhuo, L. Yu, H. Sun and X. Zhang, *ACS Appl. Mater. Interfaces*, 2016, **8**, 6439–6448.

351 L. Zhang, S. Zhu, S. Dong, N. J. Woo, Z. Xu, J. Huang, J.-K. Kim and M. Shao, *J. Electrochem. Soc.*, 2018, **165**, J3271–J3275.

352 H. Zhang, Z. Ma, J. Duan, H. Liu, G. Liu, T. Wang, K. Chang, M. Li, L. Shi, X. Meng, K. Wu and J. Ye, *ACS Nano*, 2016, **10**, 684–694.

353 M. Gong, D.-Y. Wang, C.-C. Chen, B.-J. Hwang and H. Dai, *Nano Res.*, 2016, **9**, 28–46.

354 R. Subbaraman, D. Tripkovic, D. Strmcnik, K.-C. Chang, M. Uchimura, A. P. Paulikas, V. Stamenkovic and N. M. Markovic, *Science*, 2011, **334**, 1256–1260.

355 R. Subbaraman, D. Tripkovic, K.-C. Chang, D. Strmcnik, A. P. Paulikas, P. Hirunsit, M. Chan, J. Greeley, V. Stamenkovic and N. M. Markovic, *Nat. Mater.*, 2012, **11**, 550–557.

356 M. Gong, W. Zhou, M.-C. Tsai, J. Zhou, M. Guan, M.-C. Lin, B. Zhang, Y. Hu, D.-Y. Wang, J. Yang, S. J. Pennycook, B.-J. Hwang and H. Dai, *Nat. Commun.*, 2014, **5**, 4695.

357 M. Gong, W. Zhou, M. J. Kenney, R. Kapusta, S. Cowley, Y. Wu, B. Lu, M.-C. Lin, D.-Y. Wang, J. Yang, B.-J. Hwang and H. Dai, *Angew. Chem., Int. Ed.*, 2015, **54**, 11989–11993.

358 H. Doan, I. Kendrick, R. Blanchard, Q. Jia, E. Knecht, A. Freeman, T. Jankins, M. K. Bates and S. Mukerjee, *J. Electrochem. Soc.*, 2021, **168**, 084501.

359 S. Jing, J. Lu, G. Yu, S. Yin, L. Luo, Z. Zhang, Y. Ma, W. Chen and P. K. Shen, *Adv. Mater.*, 2018, **30**, 1705979.

360 H. B. Wu, B. Y. Xia, L. Yu, X.-Y. Yu and X. W. Lou, *Nat. Commun.*, 2015, **6**, 6512.

361 Y.-J. Tang, M.-R. Gao, C.-H. Liu, S.-L. Li, H.-L. Jiang, Y.-Q. Lan, M. Han and S.-H. Yu, *Angew. Chem., Int. Ed.*, 2015, **54**, 12928–12932.

362 Y. Yang, Z. Lun, G. Xia, F. Zheng, M. He and Q. Chen, *Energy Environ. Sci.*, 2015, **8**, 3563–3571.

363 Y. Shen, Y. Zhou, D. Wang, X. Wu, J. Li and J. Xi, *Adv. Energy Mater.*, 2018, **8**, 1701759.

364 S. Wu, X. Shen, G. Zhu, H. Zhou, Z. Ji, L. Ma, K. Xu, J. Yang and A. Yuan, *Carbon*, 2017, **116**, 68–76.

365 X. Yin, L. Yang and Q. Gao, *Nanoscale*, 2020, **12**, 15944–15969.

366 S. Xu, H. Zhao, T. Li, J. Liang, S. Lu, G. Chen, S. Gao, A. M. Asiri, Q. Wu and X. Sun, *J. Mater. Chem. A*, 2020, **8**, 19729–19745.

367 X. Luo, Q. Zhou, S. Du, J. Li, L. Zhang, K. Lin, H. Li, B. Chen, T. Wu, D. Chen, M. Chang and Y. Liu, *ACS Appl. Mater. Interfaces*, 2018, **10**, 42335–42347.

368 X. Huang, X. Xu, C. Li, D. Wu, D. Cheng and D. Cao, *Adv. Energy Mater.*, 2019, **9**, 1803970.

369 F. Yang, Y. Chen, G. Cheng, S. Chen and W. Luo, *ACS Catal.*, 2017, **7**, 3824–3831.

370 R. Wang, X.-Y. Dong, J. Du, J.-Y. Zhao and S.-Q. Zang, *Adv. Mater.*, 2017, **30**, 1703711.

371 D. Y. Chung, S. W. Jun, G. Yoon, H. Kim, J. M. Yoo, K.-S. Lee, T. Kim, H. Shin, A. K. Sinha, S. G. Kwon, K. Kang, T. Hyeon and Y.-E. Sung, *J. Am. Chem. Soc.*, 2017, **139**, 6669–6674.

372 M. Pi, T. Yang, S. Wang and S. Chen, *J. Mater. Res.*, 2018, **33**, 546–555.

373 D. Zhao, K. Sun, W.-C. Cheong, L. Zheng, C. Zhang, S. Liu, X. Cao, K. Wu, Y. Pan, Z. Zhuang, B. Hu, D. Wang, Q. Peng, C. Chen and Y. Li, *Angew. Chem., Int. Ed.*, 2020, **59**, 8982–8990.

374 H. Wei, Q. Xi, X. Chen, D. Guo, F. Ding, Z. Yang, S. Wang, J. Li and S. Huang, *Adv. Sci.*, 2018, **5**, 1700733.

375 X. Yang, X. Feng, H. Tan, H. Zang, X. Wang, Y. Wang, E. Wang and Y. Li, *J. Mater. Chem. A*, 2016, **4**, 3947–3954.

376 R. A. Mir and O. P. Pandey, *Chem. Eng. J.*, 2018, **348**, 1037–1048.

377 I. Kim, S.-W. Park and D.-W. Kim, *Nanoscale*, 2018, **10**, 21123–21131.

378 Q. Zhang, F. Luo, H. Hu, R. Xu, K. Qu, Z. Yang, J. Xu and W. Cai, *Chem. Commun.*, 2019, **55**, 9665–9668.

379 Y.-Y. Chen, Y. Zhang, W.-J. Jiang, X. Zhang, Z. Dai, L.-J. Wan and J.-S. Hu, *ACS Nano*, 2016, **10**, 8851–8860.

380 L. Zhang, H. Yang, D. K. J. A. Wanigarathna and B. Liu, *Small Methods*, 2018, **2**, 1700353.

381 J.-S. Li, Y. Wang, C.-H. Liu, S.-L. Li, Y.-G. Wang, L.-Z. Dong, Z.-H. Dai, Y.-F. Li and Y.-Q. Lan, *Nat. Commun.*, 2016, **7**, 11204.

382 Y. Liu, G. Yu, G.-D. Li, Y. Sun, T. Asefa, W. Chen and X. Zou, *Angew. Chem., Int. Ed.*, 2015, **54**, 10752–10757.

383 L. Peng, J. Shen, L. Zhang, Y. Wang, R. Xiang, J. Li, L. Li and Z. Wei, *J. Mater. Chem. A*, 2017, **5**, 23028–23034.

384 F. Yu, Y. Gao, Z. Lang, Y. Ma, L. Yin, J. Du, H. Tan, Y. Wang and Y. Li, *Nanoscale*, 2018, **10**, 6080–6087.

385 X. Xu, F. Nosheen and X. Wang, *Chem. Mater.*, 2016, **28**, 6313–6320.

386 Q. Yun, Q. Lu, X. Zhang, C. Tan and H. Zhang, *Angew. Chem., Int. Ed.*, 2018, **57**, 626–646.

387 Y. Guo, T. Park, J. W. Yi, J. Henzie, J. Kim, Z. Wang, B. Jiang, Y. Bando, Y. Sugahara, J. Tang and Y. Yamauchi, *Adv. Mater.*, 2019, **31**, 1807134.

388 J. Ren, Z. Wang, Y. Feng, B. Guo, K. Yu and Z. Zhu, *New J. Chem.*, 2019, **43**, 17502–17510.

389 Z. Huang, S. Yuan, T. Zhang, B. Cai, B. Xu, X. Lu, L. Fan, F. Dai and D. Sun, *Appl. Catal., B*, 2020, **272**, 118976.

390 X. Sun, F. Liu, X. Chen, C. Li, J. Yu and M. Pan, *Electrochim. Acta*, 2019, **307**, 206–213.

391 D. Li, Z. Zong, Z. Tang, Z. Liu, S. Chen, Y. Tian and X. Wang, *ACS Sustainable Chem. Eng.*, 2018, **6**, 5105–5114.

392 W. Wu, Y. Wu, D. Zheng, K. Wang and Z. Tang, *Electrochim. Acta*, 2019, **320**, 134568.

393 J. Wang, D. Gao, G. Wang, S. Miao, H. Wu, J. Li and X. Bao, *J. Mater. Chem. A*, 2014, **2**, 20067–20074.

394 Y. Hou, Z. Wen, S. Cui, S. Ci, S. Mao and J. Chen, *Adv. Funct. Mater.*, 2015, **25**, 872–882.

395 M. Li, T. Liu, X. Bo, M. Zhou and L. Guo, *J. Mater. Chem. A*, 2017, **5**, 5413–5425.

396 Q. Mo, N. Chen, M. Deng, L. Yang and Q. Gao, *ACS Appl. Mater. Interfaces*, 2017, **9**, 37721–37730.

397 Z. Chen, Y. Ha, H. Jia, X. Yan, M. Chen, M. Liu and R. Wu, *Adv. Energy Mater.*, 2019, **9**, 1803918.

398 T. Zhang, R. Cheng, B. Li, C. Wang, Y. Guo, J. Liu and L. Wang, *Chem. Commun.*, 2021, **57**, 769–772.

399 J. Li, Y. Wang, T. Zhou, H. Zhang, X. Sun, J. Tang, L. Zhang, A. M. Al-Enizi, Z. Yang and G. Zheng, *J. Am. Chem. Soc.*, 2015, **137**, 14305–14312.

400 H. Yang, Z. Chen, W. Hao, H. Xu, Y. Guo and R. Wu, *Appl. Catal., B*, 2019, **252**, 214–221.

401 J. Zhang, Y. Jiang, Y. Wang, C. Yu, J. Cui, J. Wu, X. Shu, Y. Qin, J. Sun, J. Yan, H. Zheng, Y. Zhang and Y. Wu, *Electrochim. Acta*, 2019, **321**, 134652.

402 Y. Ha, L. Shi, Z. Chen and R. Wu, *Adv. Sci.*, 2019, **6**, 1900272.

403 J.-T. Ren, G.-G. Yuan, C.-C. Weng and Z.-Y. Yuan, *Electrochim. Acta*, 2018, **261**, 454–463.

404 Z. Peng, Y. Yu, D. Jiang, Y. Wu, B. Y. Xia and Z. Dong, *Carbon*, 2019, **144**, 464–471.

405 L. Yang and L. Zhang, *Appl. Catal., B*, 2019, **259**, 118053.

406 H. Xu, H. Jia, B. Fei, Y. Ha, H. Li, Y. Guo, M. Liu and R. Wu, *Appl. Catal., B*, 2020, **268**, 118404.

407 Z.-Y. Yu, Y. Duan, M.-R. Gao, C.-C. Lang, Y.-R. Zheng and S.-H. Yu, *Chem. Sci.*, 2017, **8**, 968–973.

408 Q. Feng, Y. Xiong, L. Xie, Z. Zhang, X. Lu, Y. Wang, X.-Z. Yuan, J. Fan, H. Li and H. Wang, *ACS Appl. Mater. Interfaces*, 2019, **11**, 25123–25132.

409 M. Li, Y. Zhu, H. Wang, C. Wang, N. Pinna and X. Lu, *Adv. Energy Mater.*, 2019, **9**, 1803185.

410 Q. Hao, S. Li, H. Liu, J. Mao, Y. Li, C. Liu, J. Zhang and C. Tang, *Catal. Sci. Technol.*, 2019, **9**, 3099–3108.

411 F. Li, R. Xu, Y. Li, F. Liang, D. Zhang, W.-F. Fu and X.-J. Lv, *Carbon*, 2019, **145**, 521–528.

412 H. Sun, X. Xu, Y. Song, W. Zhou and Z. Shao, *Adv. Mater.*, 2021, **31**, 2009779.

413 L. Sun, Q. Luo, Z. Dai and F. Ma, *Coord. Chem. Rev.*, 2021, **444**, 214049.

414 Z. Zhang, X. Ma and J. Tang, *J. Mater. Chem. A*, 2018, **6**, 12361–12369.

415 Y. Jin, H. Wang, J. Li, X. Yue, Y. Han, P. K. Shen and Y. Cui, *Adv. Mater.*, 2016, **28**, 3785–3790.

416 Y. Li, H. Zhang, M. Jiang, Q. Zhang, P. He and X. Sun, *Adv. Funct. Mater.*, 2017, **27**, 1702513.

417 L. Yu, Q. Zhu, S. Song, B. McElhenny, D. Wang, C. Wu, Z. Qin, J. Bao, Y. Yu, S. Chen and Z. Ren, *Nat. Commun.*, 2019, **10**, 5106.

418 S. Hao, L. Chen, C. Yu, B. Yang, Z. Li, Y. Hou, L. Lei and X. Zhang, *ACS Energy Lett.*, 2019, **4**, 952–959.

419 P. Zhai, Y. Zhang, Y. Wu, J. Gao, B. Zhang, S. Cao, Y. Zhang, Z. Li, L. Sun and J. Hou, *Nat. Commun.*, 2020, **11**, 5462.

420 G. Qian, G. Yu, J. Lu, L. Luo, T. Wang, C. Zhang, R. Ku, S. Yin, W. Chen and S. Mu, *J. Mater. Chem. A*, 2020, **8**, 14545–14554.

421 L. Hui, Y. Xue, B. Huang, H. Yu, C. Zhang, D. Zhang, D. Jia, Y. Zhao, Y. Li, H. Liu and Y. Li, *Nat. Commun.*, 2018, **9**, 5309.

422 L. Hui, D. Jia, H. Yu, Y. Xue and Y. Li, *ACS Appl. Mater. Interfaces*, 2019, **11**, 2618–2625.

423 J. Meng, X. Liu, C. Niu, Q. Pang, J. Li, F. Liu, Z. Liu and L. Mai, *Chem. Soc. Rev.*, 2020, **49**, 3142–3186.

424 L. Liu, P. Concepción and A. Corma, *J. Catal.*, 2016, **340**, 1–9.

425 B. P. Le Monnier, F. Wells, F. Talebkeikhah and J. S. Luterbacher, *Adv. Mater.*, 2019, **31**, 1904276.

426 M. Makosch, W.-I. Lin, V. Bumbálek, J. Sá, J. W. Medlin, K. Hungerbühler and J. A. van Bokhoven, *ACS Catal.*, 2012, **2**, 2079–2081.

427 A. C. Chien and J. A. van Bokhoven, *Catal. Sci. Technol.*, 2015, **5**, 3518–3524.

428 A. Beck, X. Huang, L. Artiglia, M. Zabilskiy, X. Wang, P. Rzepka, D. Palagin, M.-G. Willinger and J. A. van Bokhoven, *Nat. Commun.*, 2020, **11**, 3220.

429 G. Gershinsky, P. Nanikashvili, R. Elazari and D. Zitoun, *ACS Appl. Energy Mater.*, 2018, **1**, 4678–4685.

430 K. Saadi, P. Nanikashvili, Z. Tatus-Portnoy, S. Hardisty, V. Shokhen, M. Zysler and D. Zitoun, *J. Power Sources*, 2019, **422**, 84–91.

431 M. P. Clark, M. Xiong, K. Cadien and D. G. Ivey, *ACS Appl. Energy Mater.*, 2020, **3**, 603–613.

432 T. Tang, W.-J. Jiang, X.-Z. Liu, J. Deng, S. Niu, B. Wang, S.-F. Jin, Q. Zhang, L. Gu, J.-S. Hu and L.-J. Wan, *J. Am. Chem. Soc.*, 2020, **142**, 7116–7127.

433 I. Chang, S. Ji, J. Park, M. H. Lee and S. W. Cha, *Adv. Energy Mater.*, 2015, **5**, 1402251.

434 J. W. Shin, S. Oh, S. Lee, J.-G. Yu, J. Park, D. Go, B. C. Yang, H. J. Kim and J. An, *ACS Appl. Mater. Interfaces*, 2019, **11**, 46651–46657.

435 J. Seo, N. Tsvetkov, S. J. Jeong, Y. Yoo, S. Ji, J. H. Kim, J. K. Kang and W. Jung, *ACS Appl. Mater. Interfaces*, 2020, **12**, 4405–4413.

436 Z. Wang, Y. Zou, Y. Li and Y. Cheng, *Small*, 2020, **16**, 1907042.

437 U. Nisar, N. Muralidharan, R. Essehli, R. Amin and I. Belharouak, *Energy Storage Mater.*, 2021, **38**, 309–328.

438 X. Qu, L. Shen, Y. Mao, J. Lin, Y. Li, G. Li, Y. Zhang, Y. Jiang and S. Sun, *ACS Appl. Mater. Interfaces*, 2019, **11**, 31869–31877.

439 W. Li, C. Zhang, M. Han, Y. Ye, S. Zhang, Y. Liu, G. Wang, C. Liang and H. Zhang, *ACS Appl. Mater. Interfaces*, 2019, **11**, 44186–44195.

440 S. Zhang, P. Kang, S. Ubnoske, M. K. Brennaman, N. Song, R. L. House, J. T. Glass and T. J. Meyer, *J. Am. Chem. Soc.*, 2014, **136**, 7845–7848.

441 Z. Cai, Y. Zhang, Y. Zhao, Y. Wu, W. Xu, X. Wen, Y. Zhong, Y. Zhang, W. Liu, H. Wang, Y. Kuang and X. Sun, *Nano Res.*, 2019, **12**, 345–349.

442 P. An, L. Wei, H. Li, B. Yang, K. Liu, J. Fu, H. Li, H. Liu, J. Hu, Y.-R. Lu, H. Pan, T.-S. Chan, N. Zhang and M. Liu, *J. Mater. Chem. A*, 2020, **8**, 15936–15941.

443 K. Liang, R. Ricco, C. M. Doherty, M. J. Styles, S. Bell, N. Kirby, S. Mudie, D. Haylock, A. J. Hill, C. J. Doonan and P. Falcaro, *Nat. Commun.*, 2015, **6**, 7240.

444 R. F. Mendes, F. Figueira, J. P. Leite, L. Gales and F. A. Almeida Paz, *Chem. Soc. Rev.*, 2020, **49**, 9121–9153.

445 X. Wang, L. Li, T. Zhang, B. Lin, J. Ni, C.-T. Au and L. Jiang, *Chem. Commun.*, 2019, **55**, 474–477.

446 H. Lee, S. M. Dellatore, W. M. Miller and P. B. Messersmith, *Science*, 2007, **318**, 426–430.

447 W. Zhan, Q. He, X. Liu, Y. Guo, Y. Wang, L. Wang, Y. Guo, A. Y. Borisevich, J. Zhang, G. Lu and S. Dai, *J. Am. Chem. Soc.*, 2016, **138**, 16130–16139.

448 W. Zhan, Y. Shu, Y. Sheng, H. Zhu, Y. Guo, L. Wang, Y. Guo, J. Zhang, G. Lu and S. Dai, *Angew. Chem., Int. Ed.*, 2017, **56**, 4494–4498.

449 S. Yook, H. Shin, H. Kim and M. Choi, *ChemCatChem*, 2014, **6**, 2836–2842.

450 S. Y. Moon, B. Naik, C.-H. Jung, K. Qadir and J. Y. Park, *Catal. Today*, 2016, **265**, 245–253.

451 I. Ro, Y. Liu, M. R. Ball, D. H. K. Jackson, J. P. Chada, C. Sener, T. F. Kuech, R. J. Madon, G. W. Huber and J. A. Dumesic, *ACS Catal.*, 2016, **6**, 7040–7050.

452 B. Jiang, Y. He, B. Li, S. Zhao, S. Wang, Y.-B. He and Z. Lin, *Angew. Chem., Int. Ed.*, 2017, **56**, 1869–1872.

453 D.-C. Guan, S. Tian, Y.-H. Sun, F. Deng, J.-M. Nan, G.-Z. Ma and Y.-P. Cai, *Electrochim. Acta*, 2019, **322**, 134722.

454 D. Gueona and J. H. Moon, *Chem. Commun.*, 2019, **55**, 361–364.